UNIVERSITY OF CAPE TOWN

FACULTY OF ENGINEERING AND THE BUILT ENVIRONMENT

Department of Mechanical Engineering

NUMERICAL DESIGN OF A 3-STAGE CASCADED THERMAL ENERGY STORAGE SYSTEM FOR SOLAR APPLICATION

By

Chimezie Oguike

A dissertation submitted to the Department of Mechanical Engineering, University of Cape Town in partial fulfilment of the requirements for the degree of Master of Science in Mechanical Engineering

DECLARATION

I, Chimezie Oguike know the meaning of plagiarism and declare that all the work in the document, save for the properly acknowledged, is my own. This dissertation has been submitted to the Turnitin module, and I confirm that my supervisor has seen my report and any concerns revealed by such have been resolved with my supervisor.

Signed by candidate

Chimezie Oguike

Student Number: OGKCHI001

Date: 06-09-2022

ABSTRACT

Title:	**Numerical Design of a 3 Stage Cascaded Thermal Energy Storage System For Solar Application**
Author:	Chimezie Oguike (OGKCHI001)
Supervisor:	Prof. Tunde Bello-Ochende
University:	University of Cape Town
Department:	Mechanical Engineering
Degree:	Master of Science in Mechanical Engineering (M.Sc. Mech. Eng.)

The analysis of a three-stage cascaded thermal energy storage is presented in this dissertation. Cascaded thermal energy storage systems has many advantages over conventional thermal energy storages, majorly it allows for maintaining of a nigh-constant temperature between the HTF and PCM during the charging and discharging cycles leading to improved performance of the system.

This dissertation investigates the performance and transient response of a packed bed operating under high-temperature conditions with phase change materials in varying encapsulations (cascaded in a three-stage format) during charging and discharging cycle by employing computational numerical techniques via commercially available ANSYS Fluent software.

The analysis was performed for nine different encapsulation geometries with increased surface area and constant volume in comparison to the base geometry (sphere) to determine the effects of each new encapsulation on the performance of the thermal energy storage (TES). The computational model used in the development of this work compares well with the experimental results by Raul [1]. Additionally, the effect of packing scheme/PCM layout is also investigated in this work. Comparative data analysis was performed on the TES with the various PCM encapsulation designs and the standard spherical PCM encapsulation to determine which geometry provides better performance during charging and discharging cycles.

The results of this study show that the thermal performance of the cascaded thermal energy storage improves with each new encapsulation as evidenced by the decreases in charging and discharging times in comparison to the base encapsulation. This study also highlights which capsule design is most practical when considering the bed dimension increases/ decreases with in increasing thermal performance. This study's findings can serve as a benchmark for future optimization of cascaded thermal energy storage systems.

ACKNOWLEDGEMENTS

Acknowledgement and thanks are given to my supervisor Prof. Tunde Bello-Ochende for his guidance and continuous encouragement throughout this project.

I thank my parents for their continued support and provision during the course of my life.

I give special thanks to my aunt, Dr. Grace Nnadi and the Mastercard UCT Coordinators, Siya, Riyyad, Xolani, Jean and Khoza for all the support and encouragement you provided throughout my studies.

Finally, the funding received from the Mastercard Foundation is gratefully acknowledged and appreciated.

Table of Contents

Table of Figures

List of Tables

NOMENCLATURE

Symbols

A	cross-sectional area of the material	m^2
x, y, z	axial coordinates	m
Bi	Biot number	
S	damping source term	
d	diameter	m
w	dimensionless geometric parameter defined by $1 + w = lA/V$	
Q	Energy	J
Fo	Fourier number	
Gr	Grashof number	
g	gravitational acceleration	m/s^2
k	heat transfer coefficient	$W/m^2{\cdot}K$
L	latent heat of fusion	J/kg
l	length in the flow direction	m
m	mass	kg
f	melt fraction	
Nu	Nusselt number	
Pr	Prandtl number	
p	pressure	Pa
r	radius or radial coordinate	m
Ra	Rayleigh number	
Re	Reynolds number	
h	sensible volumetric enthalpy	J/m^3
Cp	specific heat capacity at constant pressure	J/kg K
Ste	Stefan number	
T	temperature	C or K
k	thermal conductivity	W/m K
α	thermal diffusivity of PCM	m^2/s
H	total volumetric enthalpy of PCM	J/m^3
v	velocity	m/s
U	velocity vector	m/s
V	volume	m^3

Greek Symbols

α	thermal diffusivity of PCM	m^2/s
βt	thermal expansion coefficient	K^{-1}
ΔT	temperature difference	°C or K
ε	porosity	-
φt	dimensionless temperature difference	-
λ	mixture thermal conductivity	-
μ	dynamic viscosity of the liquid PCM	kg/(m ·s)
ν	kinematic viscosity	m^2/s
ω	admissible error	-
Ω	a constant introduced to avoid division by zero in the Carman-Kozeny equation	-
ρ	mixture density of PCM	kg/m^3
τ	time	s

Abbreviations

2-D	Two Dimensional
3-D	Three Dimensional
CFD	Computational fluid dynamics
CSP	Concentrated Solar Power
DIF	Diffuse Horizontal Irradiance
DNI	Direct Normal Irradiance
GHI	Global Horizontal Irradiance
HDPE	High Density Poly-Ethylene
HFC	Heliostat Field Collector
HTF	Heat Transfer Fluid
LFR	Linear Fresnel Reflector
LHS	Latent heat storage
LHTES	Latent Heat Thermal Energy Storage
PCM	Phase Change Material
PDR	Parabolic Dish Reflector
PTC	Parabolic Trough Collector
PVP	Photovoltaic Power Potential
SHS	Sensible heat storage
SPT	Solar Power Tower
TCHS	Thermo-Chemical Heat Storage
TES	Thermal Energy Storage
W, E, P, N, S	West, East, Centre, North, And South Node

CHAPTER ONE

1. Introduction

1.1 Background of Study

Cascade thermal energy storage system being a packed bed system consisting of a storage tank filled with multi-layered PCMs, is proposed as a suitable alternative to single PCM thermal storage systems in scenarios that involve large temperature differences between the heat transfer fluid and the phase change material [2]. Cascade storage is a method of heat transfer enhancement for thermal storage systems [3]. This method serves to improve the performance of the thermal energy storage systems by maintaining a nearly constant temperature difference between the HTF and PCMs during the charging and discharging cycles . Other methods of heat transfer enhancement can include encapsulation (macro, micro and nano) and use of extended surfaces (fins) [4]. The combination of two or more of these heat transfer enhancement methods further improves the performance of a thermal energy storage system. A cascade thermal storage system with multiple PCM in macro-encapsulation is presented in this study. This configuration is suitable for CSP power plant to serve as a backup source of thermal energy in trough periods of solar radiation.

1.2 Statement of Problem

Due to the rising amounts of greenhouse gases in the environment caused by the burning of fossil fuels and other energy sources with a large carbon footprint, the harvesting and usage of renewable energy resources has gained a great deal of attention in recent years [5]. Solar energy is the most essential and abundant of the numerous renewable energy supplies now available. It is also the least expensive. The disparity between demand and availability of solar energy, on the other hand, creates obstacles to its widespread adoption [6]. Thermal energy storage is a critical component in closing this gap and ensuring that solar energy can be used to generate electricity on a consistent basis. Thermal energy storage techniques such as sensible heat storage (SHS) and latent heat storage (LHS) are among the most widely used in the world [7]. Because of its high energy storage density and ability to store heat as latent heat of fusion at a steady temperature, the LHS approach is a popular choice among scientists. Phase change materials (PCMs) are materials that may undergo phase transformations from solid to solid, solid to liquid, and liquid to gas. PCMs are utilized for latent heat thermal energy storage and are classified as such. The use of phase change materials (PCMs) with defined phase change temperatures allows for the storage of latent heat as thermal energy through the use of phase change materials. This is because it is one of the most efficient techniques of storing solar thermal energy currently available. In the field of solar energy, one of the most pressing topics to address is the improvement of the performance of thermal energy storage devices.

1.3 Objectives of the Investigation

The main objective of the investigation in to improve the performance of a three-stage cascade thermal energy storge with multiple phase change materials. This will be achieved through the following research objectives:

- Modelling the computational domain of cylindrical packed bed thermal energy storage.
- Development of novel capsule geometries
- CFD model validation with an experimental data to ensure congruency of the computational models to be deployed.
- Performing CFD simulations of the computational domain with each novel capsule geometry
- Comparative data analysis of the TES system performance with novel capsule geometries and the spherical geometry.
- Comparative data analysis of the performance of the TES system under different packed bed layouts
-

1.4 Originality of Work

The effect of the PCM encapsulation geometry on the performance of a thermal energy storage system has not been the subject of many a research topics. This study has found that the geometry of PCM encapsulations employed in a thermal energy storage system has critical impact on its performance in terms of charging and discharging cycle times. In the literature, this approach of TES performance enhancement has only been limited to the use of cylinders and blocks but never the full range of novel encapsulation designs developed in this study.

1.5 Dissertation Overview

The dissertation is composed of 6 chapters, each chapter is subdivided into sections for good flow and better understanding.

- Chapter 1 gives a description of the background to the research, the problem that is to be addressed and the objectives of the investigation. The originality of the work is also addressed along with the layout of the dissertation.
- Chapter 2 is the literature review, which presents a summary of the literature published on the topics of solar energy, concentrated solar power technologies, phase change materials, thermal energy storage systems, types of TES, their enhancement techniques and applications.
- Chapter 3 is the theoretical formulation section where the heat transfer mathematical models, simulation models and numerical methods for simulating phase change problems are explained.
- Chapter 4 is the validation study section where the computational domains, novel capsule design equations, the governing equations, boundary conditions and CFD model validation are presented.
- Chapter 5 is the section where the results of the simulations and the comparative data analysis of the PCM encapsulations are presented and discussed.
- Chapter 6 is the section where the conclusions from the study are drawn and the recommendations for future work are proposed.

CHAPTER TWO

2. Literature Review

2.1 Background Information

This chapter brings to light an overview of previous research conducted in the field of solar thermal energy systems as well as the importance of the use of solar energy in South Africa and the broader Africa. This literature review also contains information on current CSP technologies employed in Africa, South Africa, and globally.

2.2 Solar Energy in Sub-Saharan Africa

The renewable form of energy from our sun is abundantly available in many areas of the African continent. It is referred to as the "Sun Continent" as it receives many more hours of bright sunshine in a year than any other continent (tropical rainforest regions excluded) [8].

The distribution of solar energy in Africa is averagely dispersed, with over 85% of the continent's landscape receiving a global solar horizontal irradiance at or above 2,000 kWh/m^2.year [9].

Africa has a solar energy theoretical reserve estimated to be about 60 EWh. These energy reserves are significantly distributed within the South Africa, Sudan, and Tanzania regions with an annual irradiance of 1500 – 2000 kWh/m^2 [10]. Figures 1.1, 1.2, and 1.3 show the direct normal irradiance, global horizontal irradiance, and photovoltaic power potential of Sub-Saharan Africa.

The following images present crucial solar parameters for Sub-Saharan Africa;

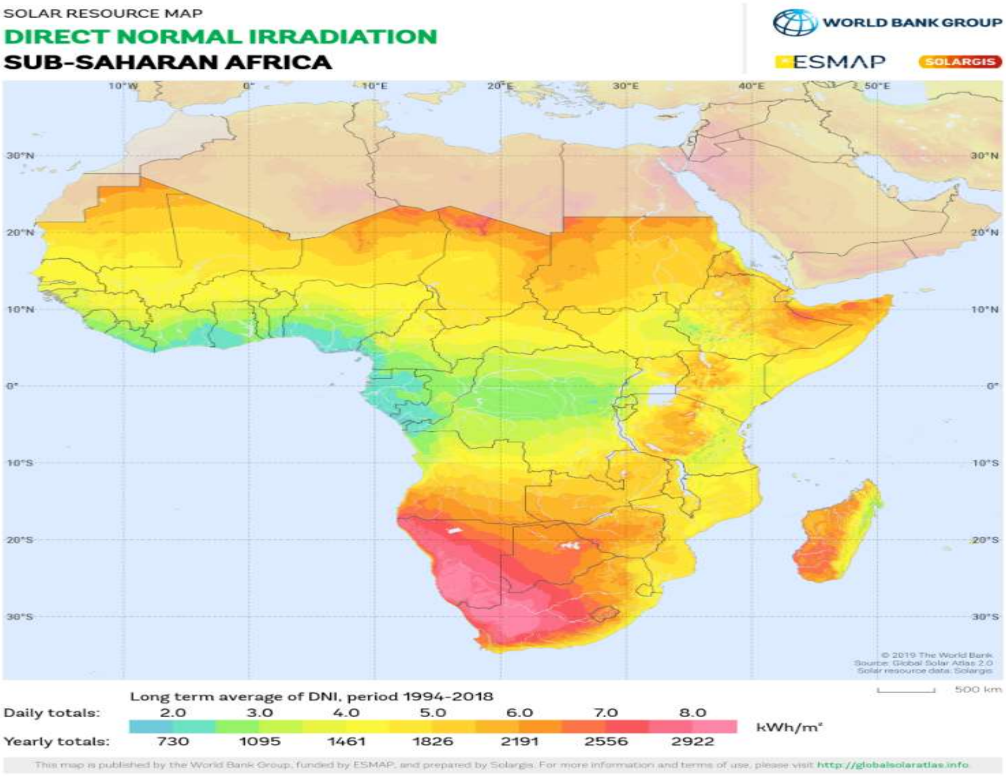

Figure 2-1:Annual Direct Normal Irradiance map of Sub-Saharan Africa [9]

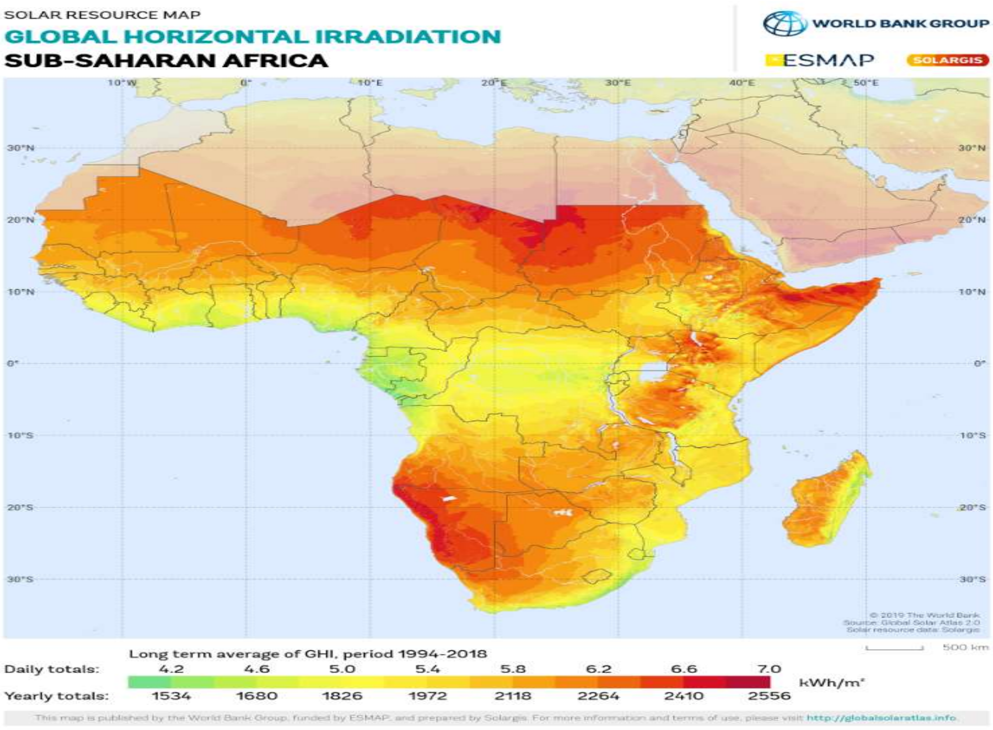

Figure 2-2: Annual Global Horizontal Irradiance map of Sub-Saharan Africa [9]

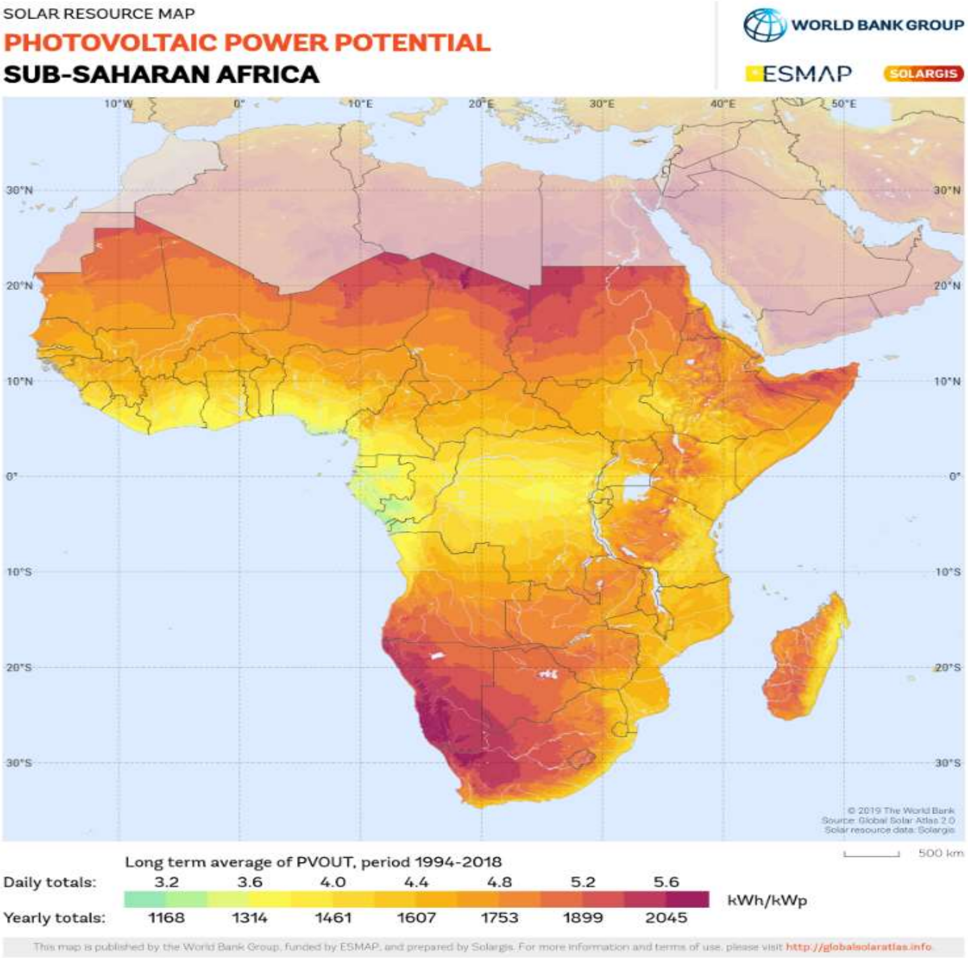

Figure 2-3: Annual Photovoltaic Power Potential map of Sub-Saharan Africa [9]

2.3 Solar Energy in South Africa

South Africa receives solar radiation of about 24 GWhr/m^2 each year over its 1.22 million km^2 of land [11].

According to the South African Department of Energy, the 24-hour global solar radiation average per annum is approximately 220 W/m^2 for South Africa compared to the USA, which receives 150 W/m^2, and the UK and Europe receive about 100 W/m^2. This makes South Africa's local resource, one of the highest in the world. Figure 2-4 shows the annual DNI (Direct Normal Irradiance) map of South Africa.

Solar energy in South Africa is harnessed through Photovoltaics as well as Concentrated Solar Power (CSP) technologies. In 2016, South Africa began operation of its latest operational solar-tower power plant named Khi Solar One with a capacity of 50MW, and it is expected to generate electricity of about 180 GWh/year. The Redstone Solar Thermal Plant which commenced in 2018 is still under development and will have a capacity of 100MW [12]

According to a study on "investment attractiveness" conducted by Greenpeace for investment in photovoltaic and CSP technologies, South Africa ranked third for CSP technologies and seventh for the photovoltaic system out of the forty countries that participated in the study. This is a reliable indicator that future development of solar energy systems, especially CSP systems, will be a feasible economic endeavor in South Africa.

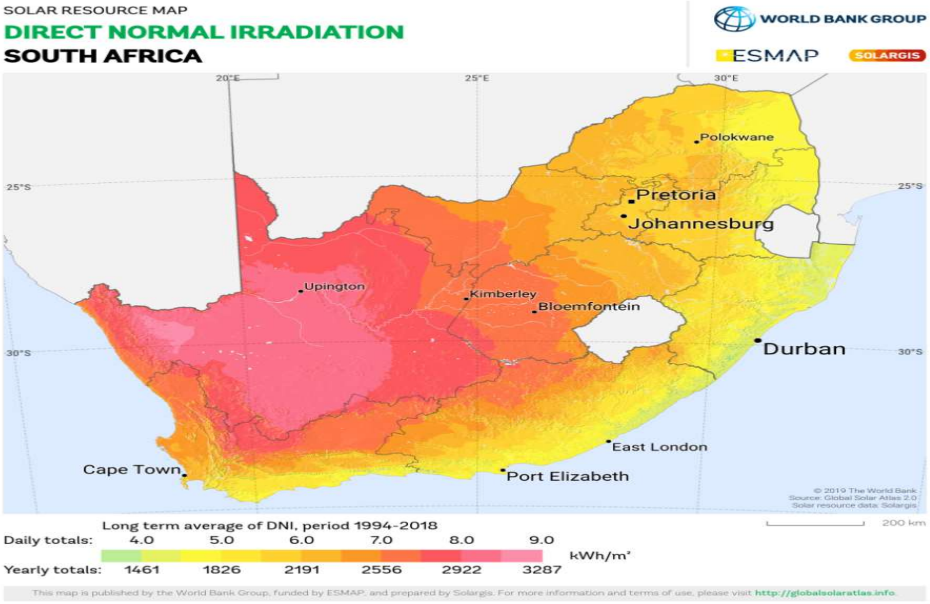

Figure 2-4: Annual DNI map of South Africa [9]

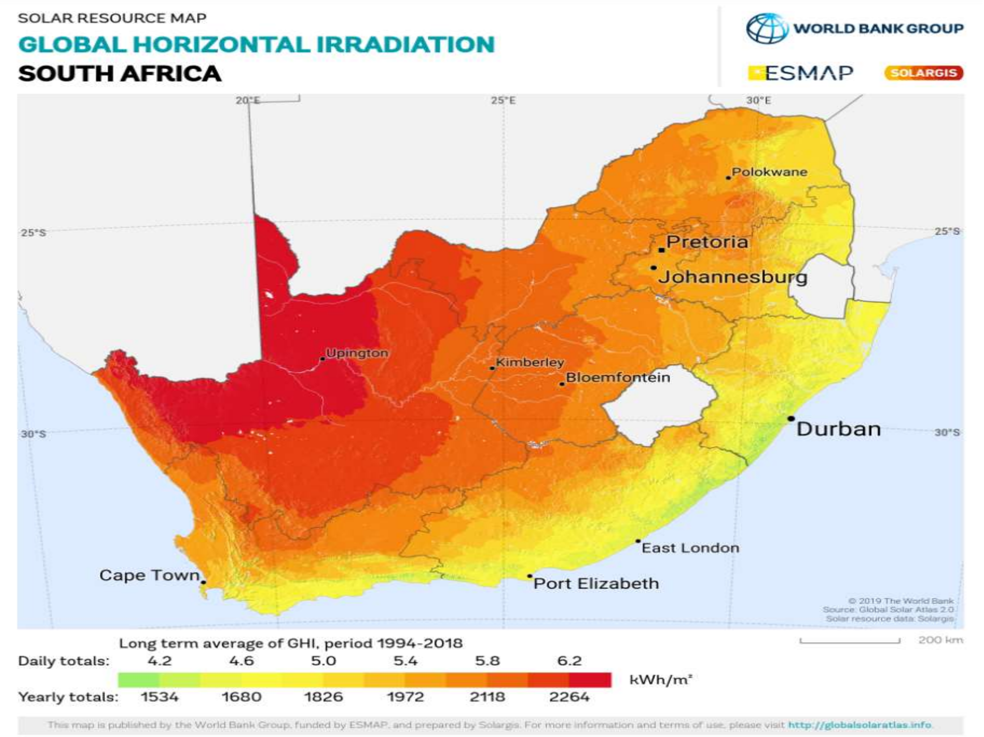

Figure 2-5: Annual GHI map of South Africa [9]

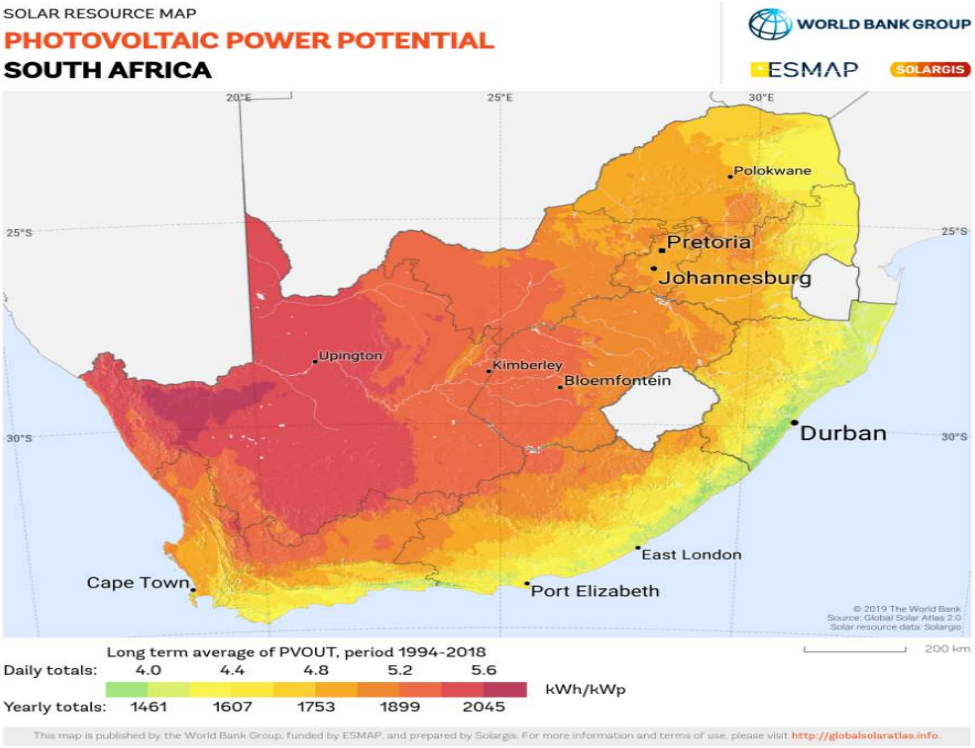

Figure 2-6: Annual PVP map of South Africa[9]

2.4 Solar Irradiance and Radiation

The sun, being a star, is a massive hydrogen-powered fusion reactor. It creates energy in form heat and other electromagnetic radiation as the byproduct of the fusion of hydrogen atoms to helium. This energy is transferred from its core, through the mantle and is radiated from its surface, reaching us on earth as solar radiation. Solar irradiance, however, is a measure of the power output produced by the sun as per unit area impinged.

The solar radiation is emitted by the Sun in space with an irradiance of about 63.3×10^6W/m^2. Due to the enormous distance between the Sun and the Earth (close to 150×10^6 km), the solar radiation has a mean intensity of 1.366kW/m^2 at the Karman line (edge of the outer atmosphere,100km above sea level) due to the attenuation (a consequence of the inverse square law) [13]. This value is described as the solar constant (K_s).

Before reaching the earth's surface, a significant proportion of solar irradiance is lost. The usable irradiance at the earth's surface is dependent on the inclination angle of its axis relative to its orbital plane around the sun. The significant contributors to the loss of irradiance are its location dependency, climatic factors, attenuation, cloud cover, the composition and thickness of the atmospheric layers, and other particulate matter which are capable of absorbing, scattering and reflecting incident irradiance [14]. These can lead to a loss of about 30% (about 340 W/m^2) in the value of the solar constant on a very clear day.

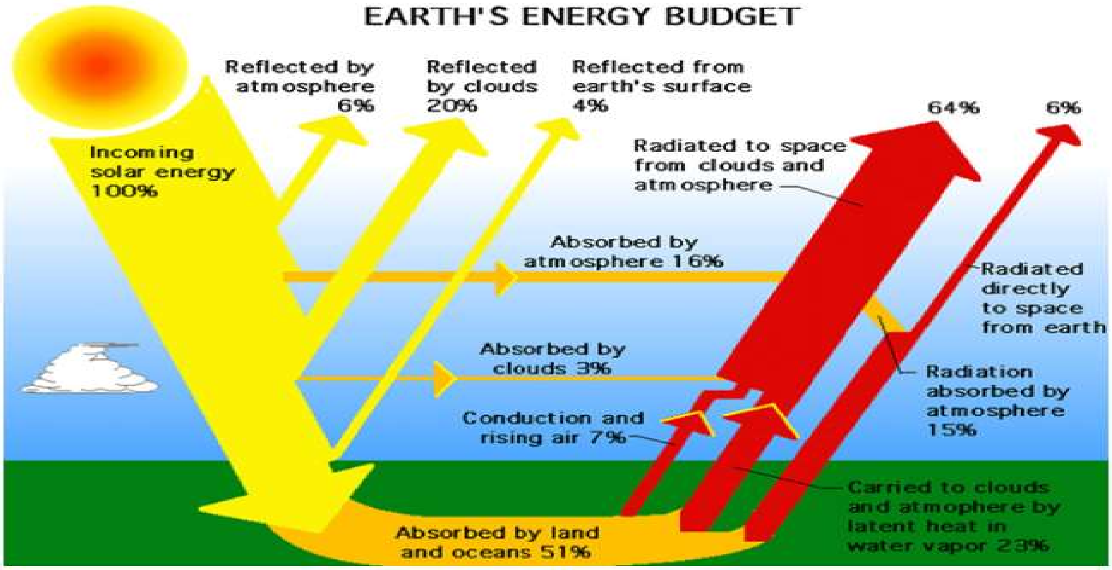

Figure 2-7: The Earth Energy Budget[15]

Solar irradiance can be represented in a couple of different ways (Glossary of Technical Renewable Energy Terminology);

I. **Direct Normal Irradiance (DNI):** This is representative of the amount of solar radiation a surface receives normal to the incident rays arriving parallel from the direction of the sun at its current location in the sky.

II. **Global Horizontal Irradiance (GHI):** This is representative of the cumulative amount of short-wave radiation a horizontal surface receives relative to the earth. It can conversely be viewed as combinate of the DNI and DIF.

III. **Diffuse Horizontal Irradiance (DIF):** This is indicative of the amount of solar radiation that comes in all directions after being scattered by atmospheric particles and molecules

IV. **Photovoltaic Power Potential (PVP):** This is indicative of the potential for which solar radiation can be converted directly to electricity using photovoltaic devices (utilizing the photo-electric effect) within a geographical region.

Other types of radiation to consider when designing and optimizing a solar collector is re-radiation from the solar collector, reflected irradiance as well as thermal radiation from surrounding bodies and the sky.

The cumulative solar irradiance at the earth's surface is the sum of the direct and diffuse radiation and is given by Equation 2-1, where θ is the normal angle between the sun and the surface [17].

$$\boldsymbol{G_{solar} = G_{direct}\cos\theta + G_{diffuse}} \qquad \textit{(2-1)}$$

Concentrated Solar Power utilizes only direct irradiance as the reflected rays are a function of the direct rays falling on the reflector while Photovoltaic technology makes use of both direct and diffuse irradiance as it works on the photoelectric effect. This study focuses on CSP technologies; hence on DNI would be considered.

2.5 Solar Thermal Collectors & Concentrated Solar Power Systems

Solar Thermal Collectors are heat exchangers that convert incident solar irradiance into thermal energy by virtue of a heat transfer fluid. Solar collectors can be classified, as illustrated in Figure 2-8.

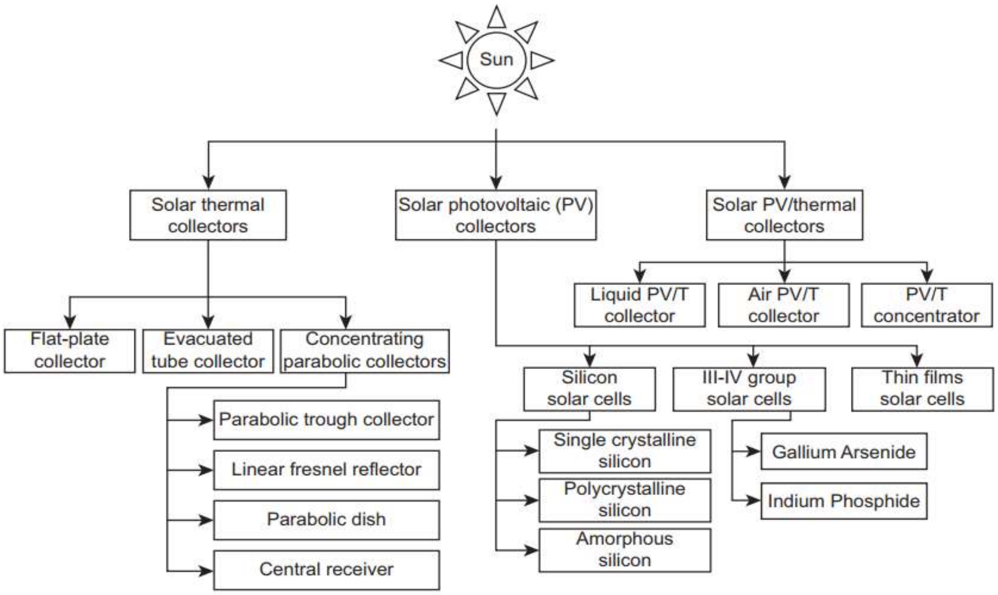

Figure 2-8: Classification of Solar Collectors [18]

Concentrated Solar Power systems make use of various concentrating solar thermal collectors. They work by intensifying via the convergence of direct irradiance from the sun on an absorber/receiver using a series of highly reflective material arranged in the right geometry, thereby converting solar radiation to thermal energy. A heat transfer fluid is contained in the receiver section. It can be used directly to drive a heat engine – as in the case of direct steam generation or to vaporize water via heat exchangers to power steam turbines for electricity generation as well as for domestic and industrial water heating purposes. Table 2-1 shows solar energy collectors, their modes of tracking, concentration ratio, and their indicative temperature ranges.

Table 2-1: Concentrating Collectors in CSP Systems and their descriptive parameters [19]

Collector Type	Motion	Absorber Type	Concentration Ratio	Indicative Temperature Range (^{0}C)
Linear Fresnel Reflector (LFR)	*Single-Axis Tracking*	*Tubular*	*10-40*	*60-250*
Parabolic Trough Collector (PTC)			*10-85*	*60-400*
Parabolic Dish Reflector (PDR)	*Two-Axis Tracking*	*Point*	*600-2000*	*100-1500*
Heliostat Field Collector (HFC)/ Solar Power Tower (SPT)			*300-1500*	*150-2000*

CSP systems incorporate solar thermal collectors and have mainly four types, as shown in Table 2-1. These four collectors are ubiquitous in their industrial and commercial applications around the world. This section provides preliminary information on each collector system mentioned.

2.5.1 Linear Fresnel Reflector System

This CSP system utilizes an array of flat single-axis tracking mirrors for concentrating solar radiation into a fixed central receiver. The array can be set up to mimic a trough shape, even while tracking the sun [20]. This system's optical can be increased by adding secondary reflectors mounted above the receiver. LFR systems are a novel addition to CSP technologies with the economic advantage of being relatively cheaper to construct and manufacture being a flat mirror system. Flat mirrors also reduce the wind load acting on the system. Figure 2-9 shows a schematic for a LFR system.

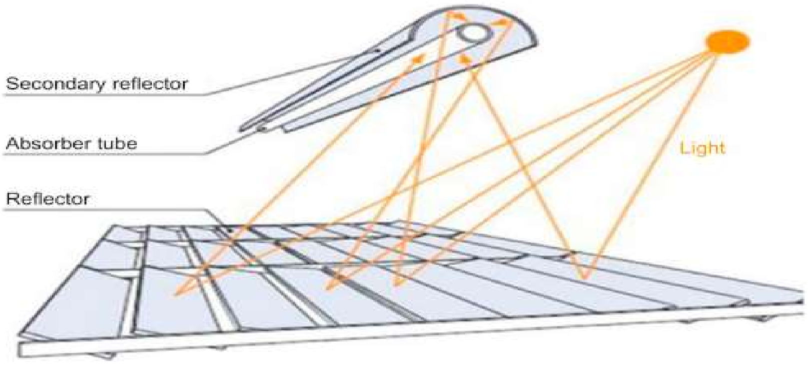

Figure 2-9: Schematic of a Linear Fresnel Reflector[21]

2.5.2 Parabolic Trough Collector System

This CSP system utilizes a series of parabolic reflective surfaces that employ single-axis tracking (installed north to south while tracking east to west) mirrors for concentrating solar radiation into a fixed tubular receiver. This system operates a focus concentrating technique - incident solar irradiance is reflected on the surface and concentrated on to a linear receiver tube ideally located at the focus of the parabolic reflector. The tube material must be of high absorptivity to curb radiation losses due to reflection, and to prevent convective losses, an evacuated glass tube is employed.

In a study comparing two linear collectors in solar thermal power plants, LFR collectors were found to have an optical efficiency of 67%, while PTC were found to have an optical efficiency of 75%. This resulted in the respective systems of having an overall electric efficiency of 19.25% for the linear Fresnel system and 23.6% for the parabolic trough system [22]. Figure 2-10 shows a schematic for a PTC system.

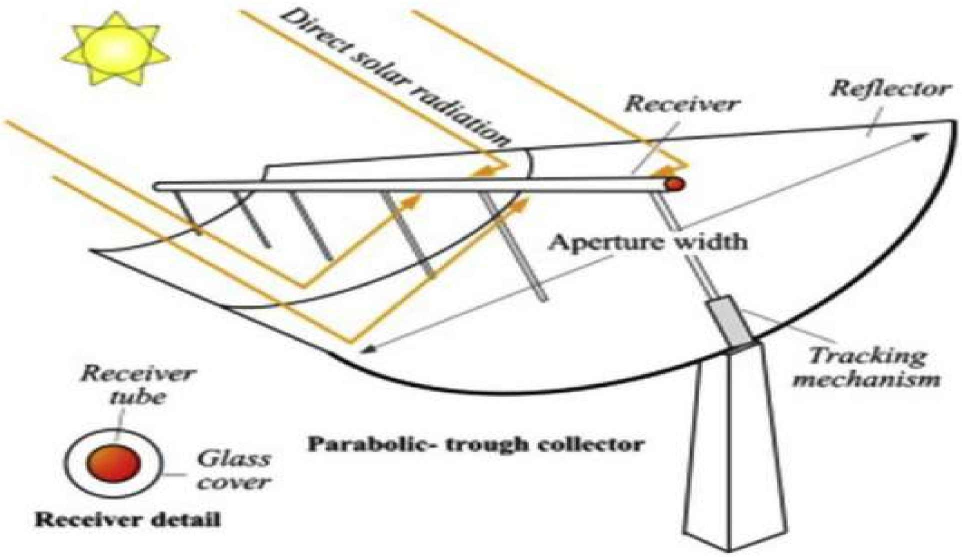

Figure 2-10: Schematic Diagram of a Parabolic Trough System[23]

2.5.3 Parabolic Dish Reflector System

This CSP system utilizes a point focus parabolic dish to converge incident irradiance into a receiver located at its focus. This system employs a dual-axis tracking mechanism (polar or altazimuth) to track the sun's location and ensure that the incident irradiance is always perpendicular to the normal of the dish, resulting in maximum working efficiency and productivity. This system achieves the highest concentration ratio based on its design and can reach temperatures above 800^0C [24].
Tubular cavity receivers combined with a Stirling engine are the primary practical design for the PDR system. The Stirling engine operates by transferring heat generated from solar irradiance to a cold sink. The work produced in that heat transfer process drives an electric power generator [25].
PDR systems are widely used for modular electricity generation systems. Figure 2-11 shows schematic for a PDR system

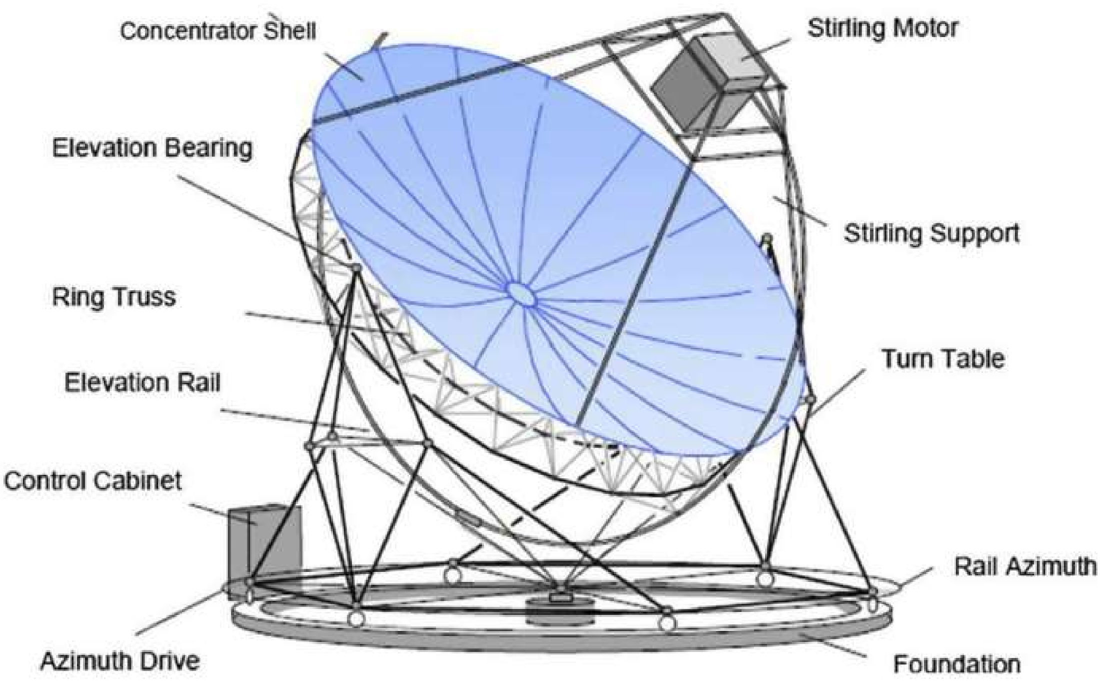

Figure 2-11: Schematic diagram PDR system [26]

2.5.4 Heliostat Field Collector System

This CSP power generation system utilizes an array of computer-controlled dual-axis flat mirrors called heliostats. These mirrors concentrate incident sun radiation onto a solar receiver atop a central tower. The receiver can be tubular, cavity, or volumetric, depending on the design of the plant. This CSP system has significant applications in commercial power generation [27].

The HFC system can be utilized in power cycles such as Brayton and Rankine as well as combinate cycles that. The heat transfer fluid employed in these cycles is molten salts. HFC systems can cope with temperatures higher than 1200^0C results in overall higher efficiency.

According to the U.S. Energy Information Administration, the HFC system is an attractive option for large scale electricity generation as it only requires a single central receiver, which reduces thermal energy losses due to large transport distances such as in linear Fresnel and trough systems. Figure 2-12 shows a schematic of a HFC system.

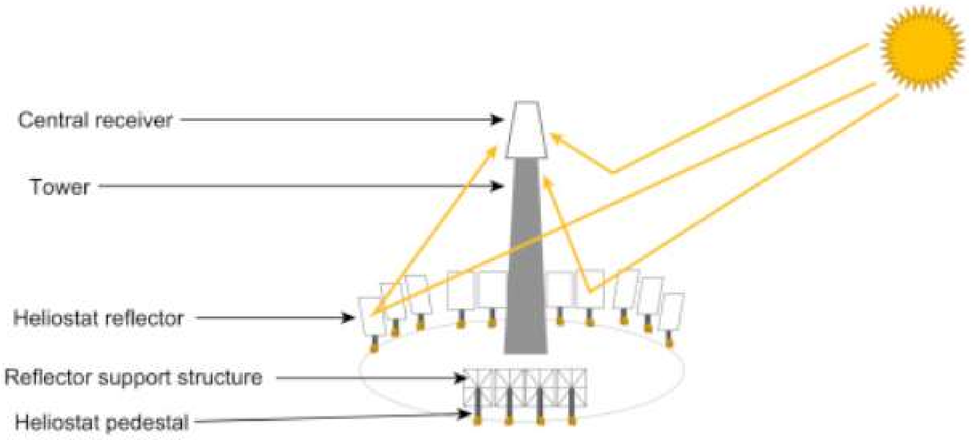

Figure 2-12: Schematic of a HFC system [24]

2.6 Thermodynamic Power Cycles utilized by CSP Systems

A thermodynamic cycle describes the processes involved in the conversion of thermal energy to useful work. In CSP systems, thermal energy is generated from solar irradiance then converted to mechanical work or electrical power. CSP plants, depending on their configuration, majorly utilize the Rankine, Brayton, and Stirling cycles as well as novel cycles like Kalina cycles. A combination of cycles can be employed to improve the overall efficiency of the system.

2.6.1 Brayton Cycle

This cycle is one of the most popular thermodynamic cycles in the CSP industry. They are ubiquitous in point concentration CSP systems. In a Brayton cycle, air is primarily the working fluid. This cycle can be either open (working fluid is used once through the system) or (working fluid used several times before being expelled from the system).

Open Brayton cycles differ from closed Brayton cycles in the number of process elements. The process elements of an open-cycle are a compressor, combustion chamber, and a turbine, whereas, in a closed-cycle, a condensing unit (heat exchanger) is included after the working fluid exits the turbine.

In the application of this cycle to CSP systems, a receiver replaces the combustion chamber, thereby heating the working fluid that exits the compressor with concentrated solar irradiance [28].

Like the Stirling cycle, the Brayton cycle is also used for generating electricity in a modular solar power set-up via a Brayton micro-turbine. Figure 2-13 shows a schematic diagram of an open solar Brayton cycle.

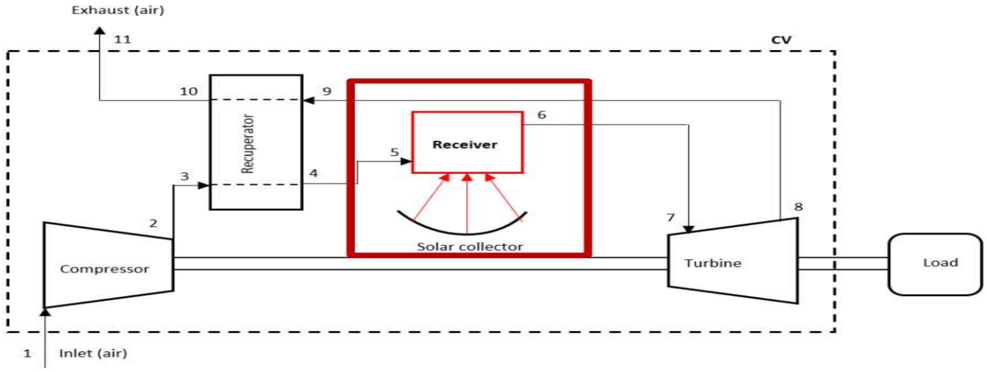

Figure 2-13:Schematic diagram of an Open Solar Brayton Cycle [29]

2.6.2 Stirling Cycle

This cycle primarily finds its application in PDR systems. A Stirling engine is required for this cycle. These engines are mounted at the focus of the PDR systems, thereby receiving the concentrated radiation through the receiver aperture, which enables power generation from a single dish.

In solar applications, the concentrated solar irradiance is used to heat and expand the working fluid (air or hydrogen) and, in turn, drives a piston, operating a linear or crank-shaft mechanism to power an alternator, thereby generating electricity. A radiator cools the working fluid, which is then fed to the expansion chamber.

Stirling engine is an attractive option for stand-alone and distributed solar power generators due to small size, simple operation, and low maintenance [30]. Stirling engines are majorly used in modular parabolic dish systems to generate power. Mobility is the hallmark of the modular approach to solar power generation as it allows for installations in rural and remote areas to provide a source of electricity to small communities [31]. Brayton microturbines are becoming a more attractive option for the small-scale and modular approach to solar power generation due to substantial costs involved in constructing and installing Stirling engines [32]. Figure 2-14 shows a solar Stirling engine in a parabolic dish system.

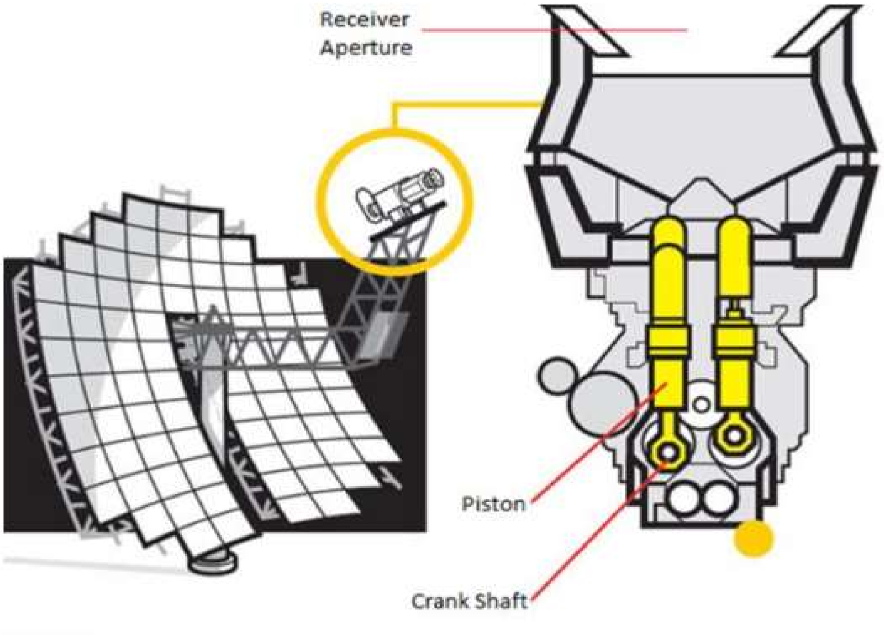

Figure 2-14:Solar Stirling Engine in a parabolic dish system [33]

2.6.3 Rankine Cycle

This thermodynamic cycle operates as a closed cycle. The working fluid employed in this cycle is usually water. There are four stages in a simple Rankine Cycle: compression of working fluid (liquid water) to high pressure via the pump, vaporization of the water via the heat exchanger/steam generator, expansion via the turbine and condensation of the steam back to the initial liquid state via the condenser [34].

In CSP applications, the heat is supplied to the system by a solar collector that heats the working fluid via concentrated solar irradiance. Steam Rankine cycles have been found to offer high thermal efficiencies for temperatures up to 600°C.

Figure 2-15 shows a schematic of this process.

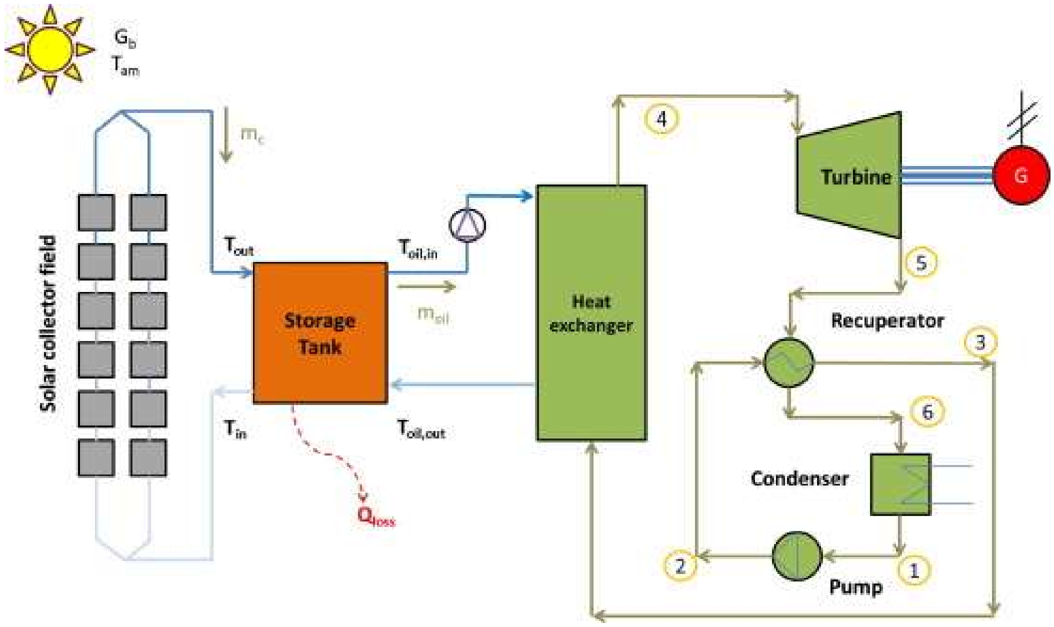

Figure 2-15:Schematic diagram of a Solar Rankine Cycle [35]

2.6.4 Kalina Cycle

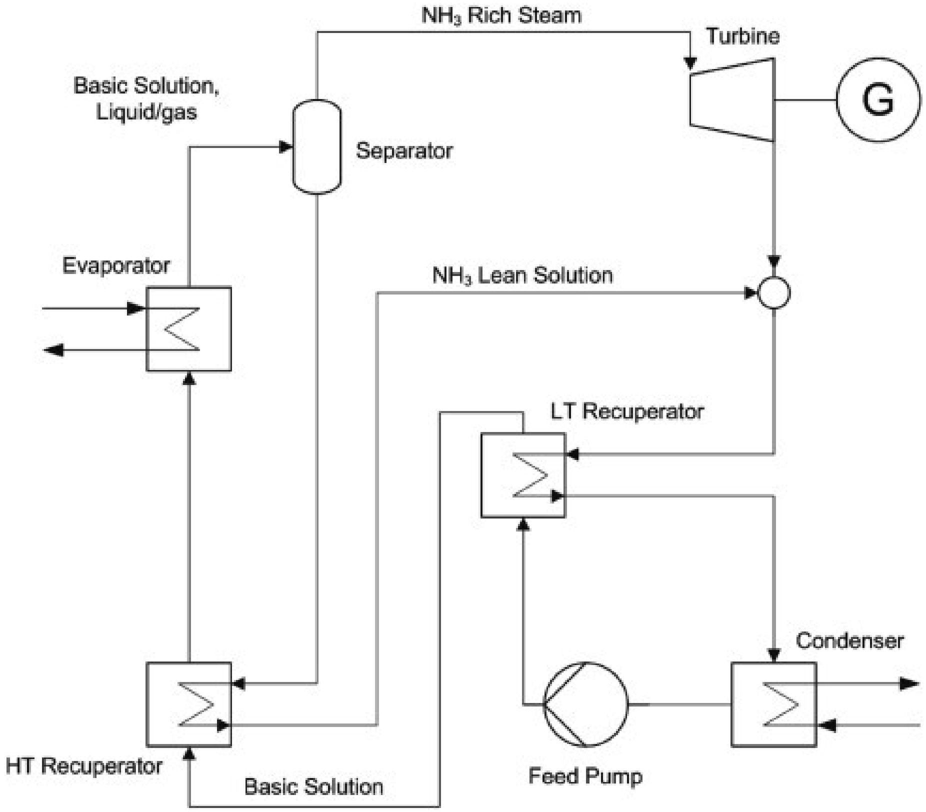

Figure 2-16: Schematic Diagram of a Kalina Cycle [36]

Like the Rankine cycle, this new thermodynamic cycle operates as a closed cycle. The working fluid utilized in this cycle is an adjustable mixture of water and ammonia and with their different boiling points . The resulting solution can boil over a broader temperature range ergo more heat can be extracted from a reservoir containing this fluid and allowing for higher thermal efficiencies [36]. This cycle is still being explored for CSP systems and is planned for use in combined cycles.

2.6.5 Combinate Cycles

The efficiency of a thermodynamic cycle helps in ascertaining the energy output for any energy input into the cycle. Increasing the efficiency of the system is paramount to ensure optimal utilization of the supplied to the system. Combining cycle is a method of increasing cycle efficiency. In most combinate cycles, waste energy at the heat sink of the primary cycle serves as the heat source for the secondary cycle [37].

A major combinate cycle configuration is the Brayton-Rankine cycle. Figure 2-17 presents a schematic diagram of a Brayton-Rankine cycle. In CSP applications, the receiver is a solar thermal collector.

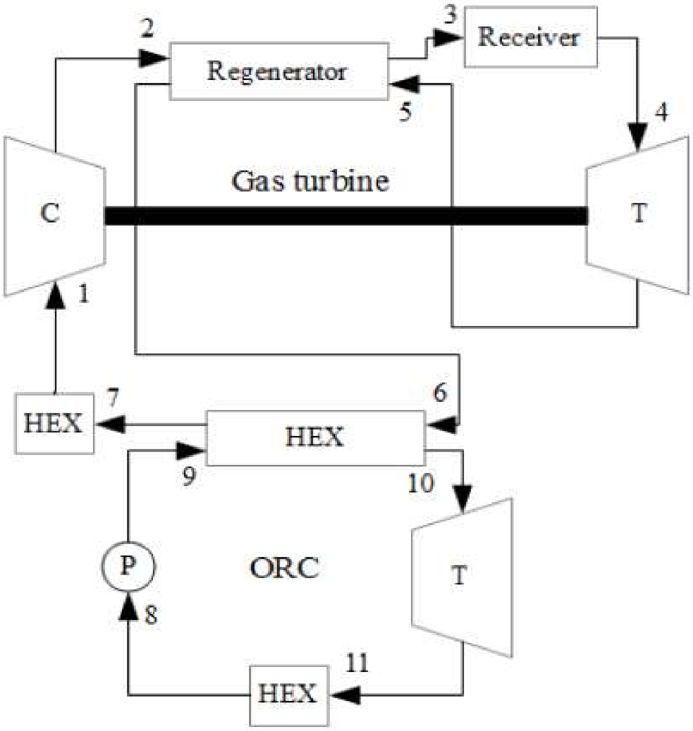

Figure 2-17:Schematic diagram of a Brayton-Rankine cycle [37]

2.7 Thermal Energy Storage (TES) in CSP Systems

Power plants that incorporate CSP systems constitute an engorging proportion of future power generation globally. The storage of solar thermal energy is essential to ensure processes that rely on this energy source can continue uninterrupted due to the intermittent nature of solar irradiance. CSP plants can incorporate thermal energy storage (TES), thereby solving the time mismatch between the intermittent solar energy supply and electricity demand profiles, and allow for efficient utilization of the turbine and other power-block components.

Thermal energy storage can be realized through;

- Sensible Heat Storage
- Latent Heat Storage
- Thermo-Chemical Heat Storage

Figure 2-18 shows three categories of thermal energy storage systems as well as their sub-categories and processes and materials involved in each.

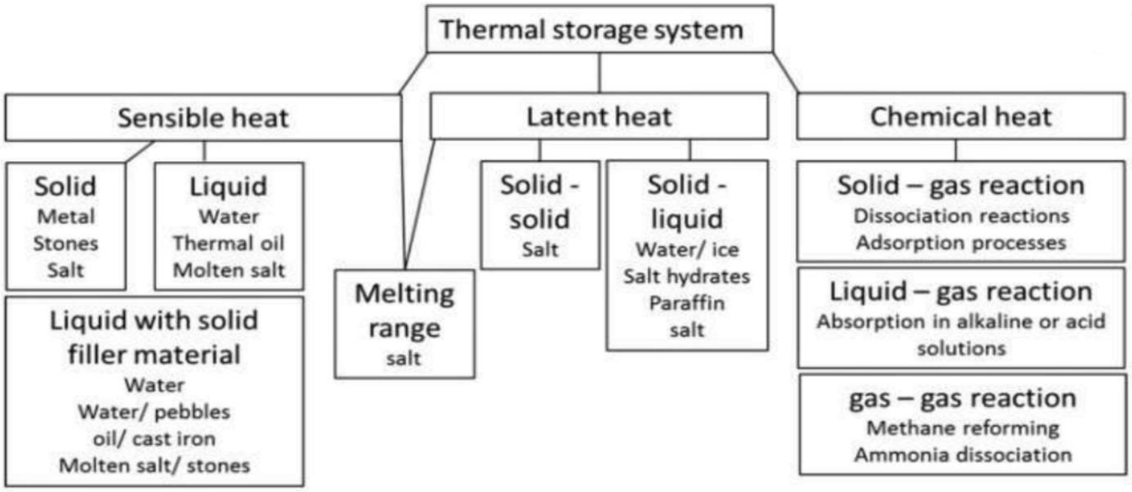

Figure 2-18: Categories of TES systems [38]

2.7.1 Sensible Heat Storage (SHS)

This type of storage is used extensively in CSP facilities. The amount of thermal energy stored depends on specific heat capacity (c_p) of the TES media and the temperature differential (ΔT) between the charge and discharge phases of the TES media. The TES media can be solid, liquid, or a solid-liquid suspension. It does not undergo any phase change or chemical reactions during storage. Equation 2-2 below expresses the amount of thermal energy stored by a given mass (m) of SHS material [39];

$$Q_{stored} = \int_{t_i}^{t_f} M\, c_p dt \qquad \text{(2-2)}$$

2.7.2 Latent Heat Storage (LHS)

This storage mode has significant potential to offset large-scale energy in CSP systems.
Thermal energy can be stored by taking advantage of the enthalpy of phase change (L) that occurs during phase transitions at a nearly constant temperature, as well as the specific heat of the storage medium. Solid-solid transitions, solid-liquid transitions, solid-gas transitions, and liquid-gas transitions are all possible in these systems. Despite the fact that they have large latent temperatures Due to the substantial volumetric limits of solid-gas and liquid-gas transformations, they are generally not used for energy storage applications. Thermal energy is stored during solid-solid phase transitions because the crystalline structure of the material is altered during the transition. This thermal storage method is less favorable due to the limited latent heats that are realized as a result of these transitions.

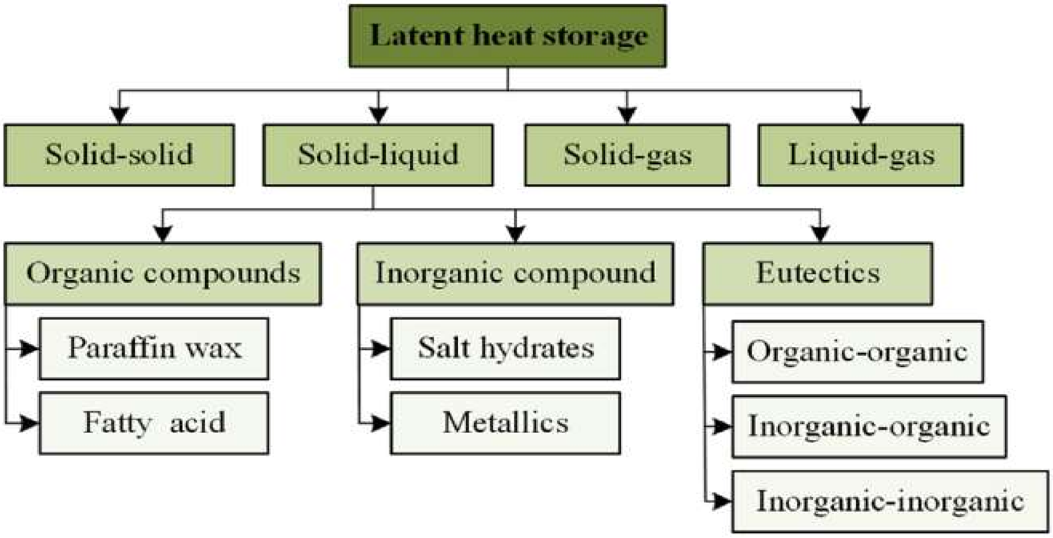

Figure 2-19: Categories of LHS and classification of PCMs [40]

Phase change materials have higher storage capacity (50 to 150 kWh/t) and storage efficiencies between 75 and 90%, unlike those in SHS [38]. The amount of thermal energy stored by a given mass (m) of PCM can be expressed by equation 2.3 [15] below;

$$\boldsymbol{Q_{stored} = \int_{t_i}^{t_m} m\, c_p dt + mfL + \int_{t_m}^{t_f} m\, c_p dt} \tag{2-3}$$

where t_m is the melting/liquidus temperature, in °C; t_i is the initial temperature, in °C; t_f is the final temperature, in °C; M is the mass of the PCM, in kg; c_p is the specific heat capacity, in J/(kg·°C); f is the melt fraction; and L is the latent heat of fusion, in J/kg

The most significant advantage of LHS over SHS is the high energy storage density that can be achieved with a minimal temperature differential between the two systems. An illustration of the difference between a SHS system and an LHS system composed of a single PCM is shown in Figure 2-20. Figure 2-21 illustrates the difference between a SHS system and an LHS system composed of cascade PCMs. There is a factor of three between the heat stored in the LHS system and the heat stored in the SHS system for the small temperature difference covering the phase transition. When there is a significant temperature difference, the advantage of the LHS is reduced to 6:4 = 1.5.

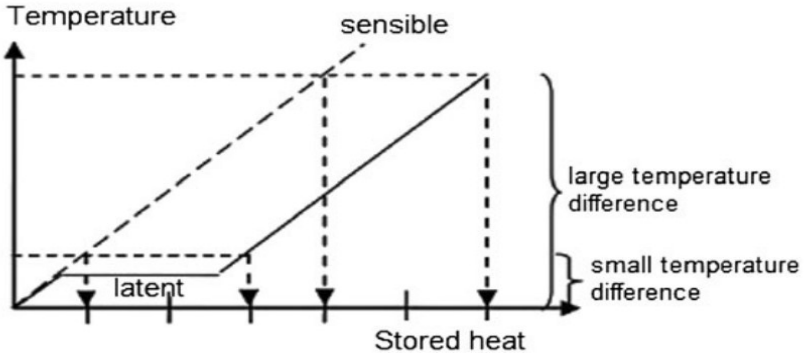

Figure 2-20: Comparison of stored heat between SHS and LHS with single PCM [7]

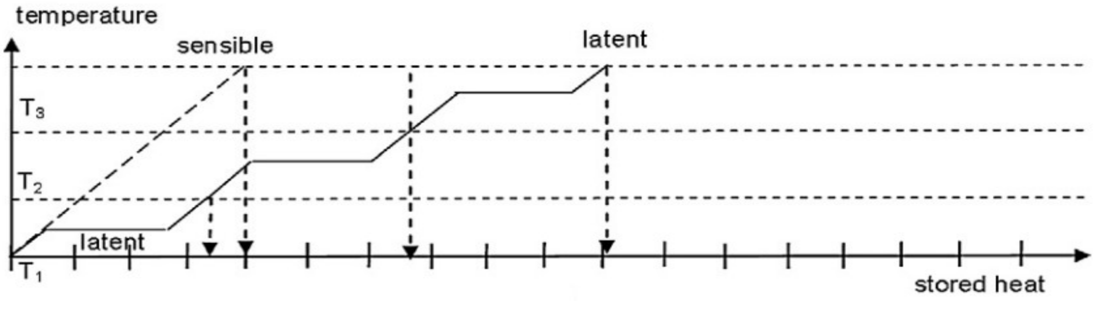

Figure 2-21: Comparison of stored heat between SHS and cascade LHS [4]

2.7.3 Thermo-Chemical Heat Storage (TCHS)

This mode of storage utilizes the chemical properties of the TES material rather than physical ones. It involves a cyclical process of reversible chemical reactions between reactant pairs and the absorption and evolution of thermal energy in breaking and reforming molecular bonds. The charge cycle is an endothermic reaction, while the discharging cycle is exothermic. In CSP systems, the endothermic heat of reaction is from concentrated solar irradiance and the heat stored is a function of the total amount (m) and fraction of material reacted (f_r) as well as the endothermic heat of reaction (h_r). Equation 2-4 gives the mathematical relationship for thermal energy stored in this system [41]. Equation 2-5 illustrates the reversible reaction during the charge and discharge cycles[42];

$$Q_{stored} = f_r m \Delta h_r \tag{2-4}$$

$$XY + Q_{endothermic} \leftrightarrow X + Y - Q_{exothermic} \tag{2-5}$$

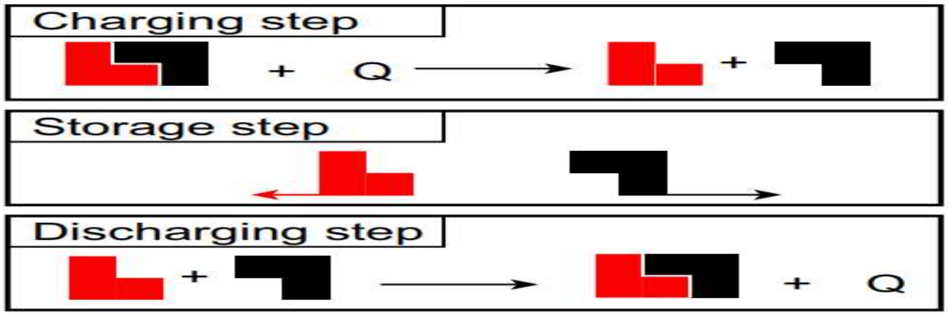

Figure 2-22: Charing, Storage and Discharging of a TCHS

TCHS has a higher energy content than LHS. Its actual performance, however, is highly dependent on the reactor design and reaction kinetics because it is reliant on adsorption/desorption or other chemical reactions. TCHS can be further classified based on the types of reactant pair system employed. They include [7];

- Hydroxide system
- Metallic Hydrides
- Carbonate system
- Redox system
- Sulfur based system

2.8 Phase Change Materials (PCMs) in LHS

Phase change materials are arguably the most significant component of any LHS system. They determine the operating conditions of every LHS. However, PCMs most possess certain properties/ characteristics before they can be deployed in LHS systems. These properties can be classified into [43];

- Thermo-physical (High thermal conductivity and enthalpy of phase transition, low volumetric expansivity during phase change, high density)
- Kinetic and chemical (Chemical stability, material compatibility, non-toxic, non-flammable, limited supercooling)
- Economics (Large-scale availability and cost of PCM)

2.8.1 Classification of PCMs

PCMs used in LHS systems are broadly characterized based on their physical transformation for heat absorption and desorption characteristics. The following are the three major categories of PCMs [43];

- Organic PCMs: These are organic compounds that can go through several melting and solidification cycles without phase separation and crystallize with little or no super-cooling.
- Inorganic PCMs: These are inorganic compounds that do not appreciably supercool and whose latent heat of fusion do not degrade with melting and solidification cycles cycling.
- Eutectic PCMs: These are a combination of two or more low melting point materials that have comparable melting and freezing points.

Table 2-2 highlights the advantages and disadvantages of each of the major PCM classes.

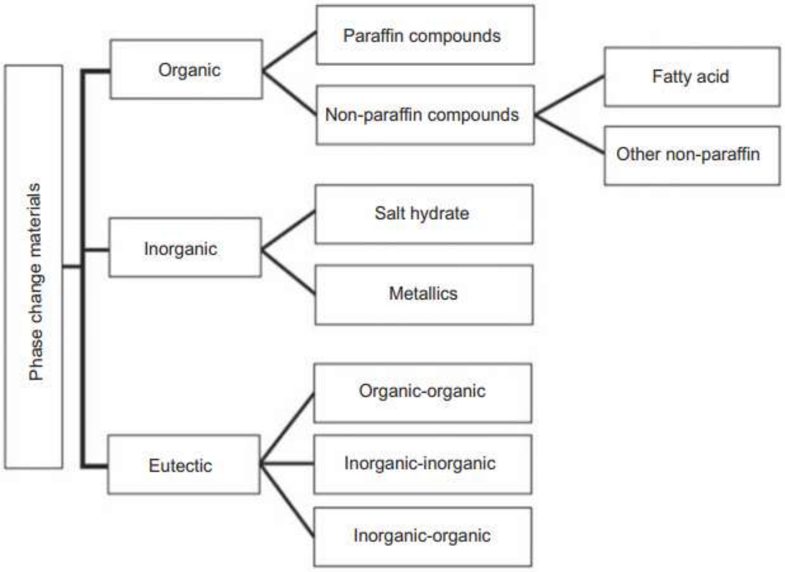

Figure 2-23: Classification of PCMs according to composition [44]

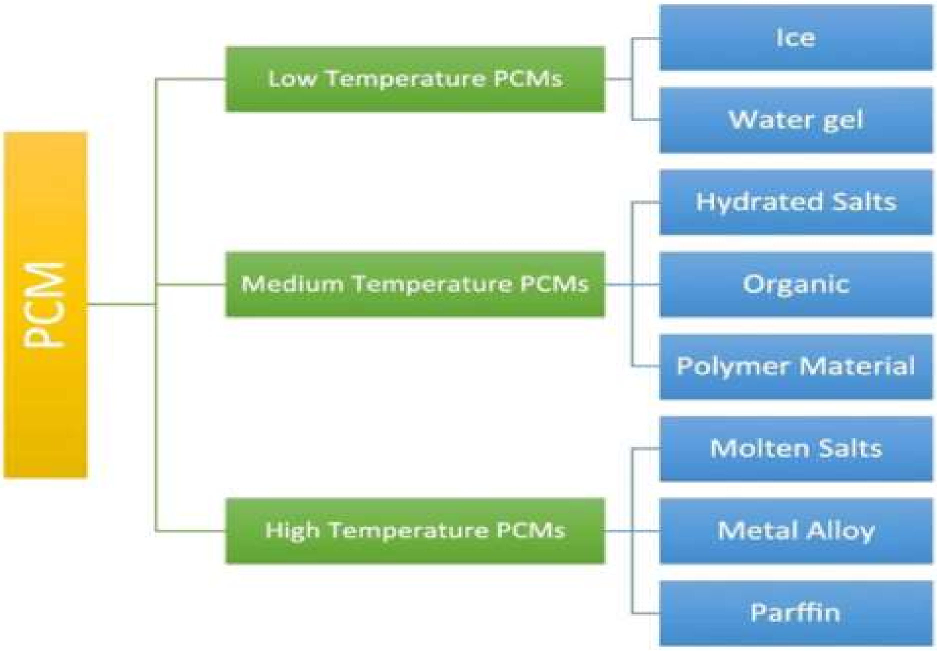

Figure 2-24: Classification of PCMs by temperature application [45]

Table 2-2: Advantages and Disadvantages of PCM Classes [46]

CLASSIFICATION	ADVANTAGES	DISADVANTAGES
Organic PCMs	*Available in a wide range of temperature conditions*	*Low thermal conductivity*
	High enthalpy of fusion *No super-cooling* *Noncorrosive* *High chemical stability and recyclable* *Compatible with a variety of different materials*	*Change in volume that is disproportionately large* *Flammability*
Inorganic PCMs	*High enthalpy of fusion* *High thermal conductivity* *Low volumetric expansivity* *Low-cost availability*	*Super-cooling* *Corrosive*
Eutectics PCMs	*Sharp melting temperature* *High thermal storage density per unit volume*	*There is a scarcity of test data for thermophysical characteristics that is currently available.*

Table 2-3: Sub Classification of Organic and Inorganic PCMs [46]

CLASSIFICATION	SUB-CLASSIFICATION	DESCRIPTION
Organic PCMs	*Paraffin compounds*	*They are composed of a mixture of primarily straight chain n-alkenes (CH3—(CH2)—CH3) that crystallize and release a significant amount of latent heat.*
	Non-paraffin compounds	*They are composed of many esters, fatty acids, alcohols, and glycols that have a higher latent heat of fusion than paraffins.*
Inorganic PCMs	*Hydrated Salts*	*These are alloys of inorganics salts that contain water of crystallization. The general formula is* $AB.nH_2O$
	Metallics	*These are low-melting point metals and their alloys with high thermal conductivities and high operating temperatures*

2.9 Development of LHTES Systems

For the purpose of developing a system for storing latent heat thermal energy, it is necessary to have a thorough understanding of three essential topics: phase transition materials, container materials, and heat exchangers. The flow chart below depicts the several processes/stages that must be completed in order for the LHTES system to be completed:

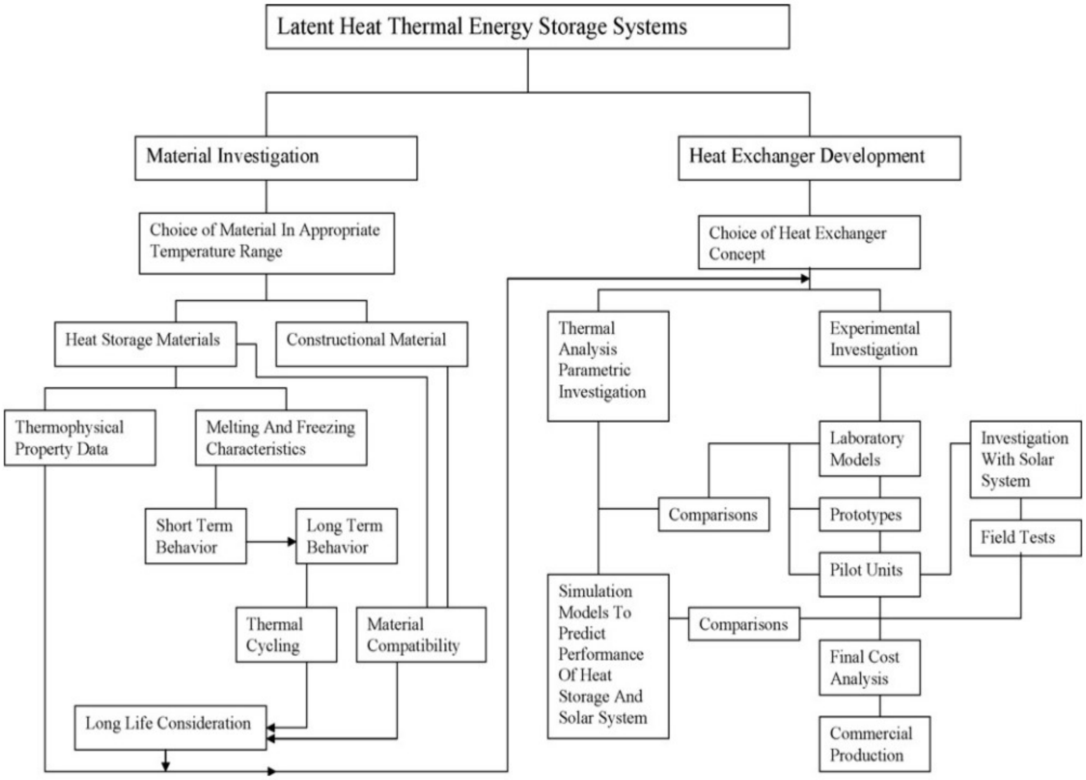

Figure 2-25: Flowchart of the different stages of LHTES Development [47]

2.10 Performance Enhancement Techniques in LHTES

Enhancement of latent heat storage systems has become an interesting research area since the global paradigm shift to renewable energy utilization to satisfy energy demands. This section will try to survey some of the techniques adopted for LHS performance enhancement.

There are three key parameters which have a positive correlation with heat transfer rate in any heat transfer process. These are the heat transfer area (A), temperature difference (ΔT) and thermal conductivity coefficient (k) between the objects transferring heat [48]. Their relationship is expressed in the equation;

$$\dot{\boldsymbol{Q}} = \boldsymbol{kA\Delta T} \qquad \textit{(2-6)}$$

Techniques for improving the performance of latent heat thermal energy storage can be categorized into three groups [4]:

- Improving the thermal conductivity of the PCM
- Heat transfer surface area extension
- Enhancing the uniformity/ consistency of the heat transfer process.

a. **Improving the PCM thermal conductivity:** All materials have a certain level of resistance to the transmission of heat energy. Decreasing the thermal resistance of the phase change material is an effective means of raising the heat transfer coefficient and, as a result, of increasing the rate of latent heat storage. This can be accomplished by increasing the thermal conductivity of the PCM with the employment of;

  - Porous materials of high thermal conductivity (metal foams, expanded graphite foams and expanded rocks) and nanoparticulate additives to form a stable composite PCM (CPCM).
  - Dispersion of low density additive materials (carbon fibers)

b. **Extending heat transfer surface area:** The rate of heat transfer is directly proportional to the surface area thus increasing the area of heat transfer enhances the heat transfer performance. The heat transfer between the heat transfer fluid (HTF) and PCM can be increased by extending the area of heat transfer using;

  - Extended metal surfaces and Finned tubes (extended surfaces placed radially/ axially on either the HTF side or PCM side)

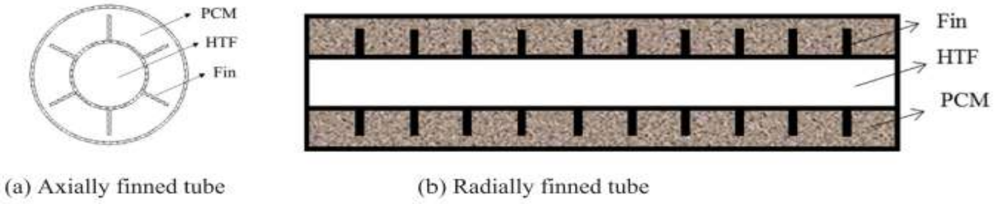

Figure 2-26: Schematic of finned tube LHS system [49]

- Encapsulated PCM (nano-capsules, micro/macro-capsules filled with PCM)

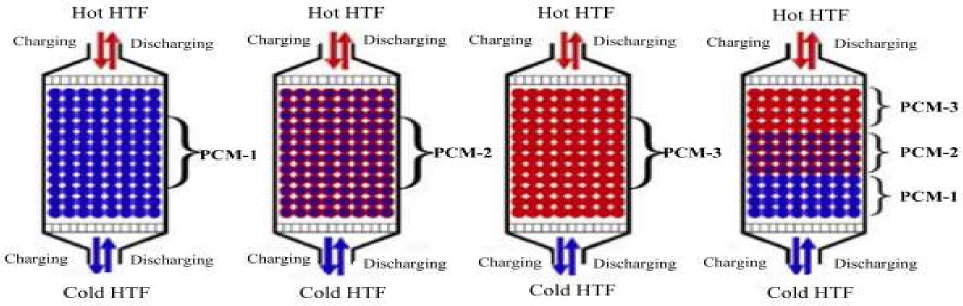

Figure 2-27: Schematic of LHS units with encapsulated PCM [4]

c. **Improving uniformity of heat transfer process:** Controlling a practically uniform temperature difference across the thermal energy storage system during the entire heat transfer process can improve the efficiency of the heat transfer process significantly. This can be achieved using;

- Multi-Stage Cascaded LHS Systems with multiple PCMs (PCMs arranged successively according to increasing or decreasing melting points)

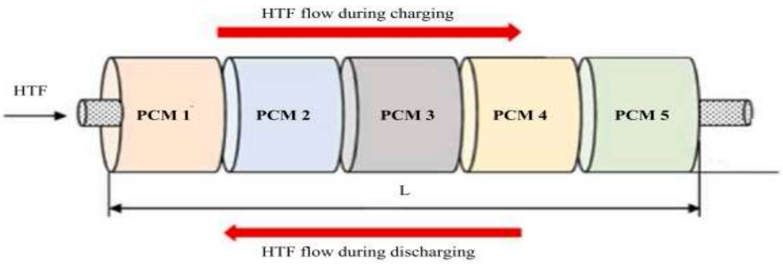

Figure 2-28: Schematic of multi-stage LHS system [50]

This research work aims the optimize the charging and discharging efficiency of a LHS system by extending the heat transfer area by employing macro-encapsulations of novel geometries and a 3 stage cascade system using high temperature inorganic PCMs.

2.11 Cascaded latent heat storage system thermal performance and optimization for utility-scale energy storage

Cascaded thermal storage PCMs (CTSPCMs), have recently emerged as a feasible technology for large-scale utility energy storage applications, especially when combined with solar energy storage systems. As previously stated, the thermal performance of heat storage systems with a single PCM must be checked on a frequent basis, especially in systems where the heat transfer fluid (HTF) and the surrounding environment have a considerable temperature differential. Furthermore, the rapid drop in HTF temperature causes an unfavorable drop in phase-change heat driving force, lowering the system's efficiency [51].

On the other hand, the concept of cascaded PCMs, which is defined as a collection of several types of PCMs that are arranged in descending order of their melting temperatures and that are used to both increase the storage capacity of the system as well as store thermal energy of varying grades [52]. The following succinctly summarizes the advantages of cascaded thermal storage PCMs over single stage thermal storage PCMs;

- As a result of the increased driving power for PCM heat transfer, the CTSPCMs can be employed in applications with a substantially wider operating temperature range and a more consistent temperature difference between the phase change material and the heat transfer fluid than previously possible [53].
- Increasing the temperature differential between the output heat transfer fluid and the surrounding environment will allow you to completely use the thermal energy contained in the heat transfer fluid. As a result, charging and discharging procedures are completed more quickly [53].
- The cascaded thermal storage PCMs significantly improve the working temperature range of the storage system while also increasing its energy efficiency [54].
- Cascaded thermal storage PCMs systems have the potential to improve overall thermal storage performance while also allowing for numerous thermal energy utilizations across a wide temperature range, which should be relevant for large-scale industrial and home solar heating and cooling applications, among other things [55]. The primary disadvantages of CTSPCMs, on the other hand, are the complexity and high operating costs of cascaded thermal storage systems, as well as the difficulty in keeping them synchronized during the PCM phase change processes. As a result, their performance in heat storage systems may be limited [56].

2.12 Applications of LHTES Systems

The applications of latent heat thermal energy storage systems fall into two broad categories: thermal protection (or inertia) and thermal storage. The thermal conductivity of the substance is one of the distinctions between these two significant fields of application. While low conductivity values are suitable in some circumstances of thermal protection, they can create a serious difficulty in storage systems, where there may be sufficient energy stored but inadequate capacity to quickly discharge it. The table below highlights some of the applications of LHTES:

Table 2-4: Sub Applications of Latent Heat Thermal Energy Storage [57] [58] [59]

S/N	APPLICATIONS
1	Building applications (PCM Wallboards, Trombe wall, shutters, under-floor heating systems, ceiling boards)
2	Cooling of engines (electric and combustion)
3	Cooling: use of off-peak rates and reduction of installed power, ice-bank
4	Food agroindustry, wine, milk products (absorbing peaks in demand), greenhouses
5	Heating and sanitary hot water: using off-peak rate and adapting unloading curves
6	Medical applications: transport of blood, operating tables, hot–cold therapies
7	Passive storage in bioclimatic building/architecture (HDPE + paraffin)
8	Safety: temperature maintenance in rooms with computers or electrical appliances
9	Softening of exothermic temperature peaks in chemical reactions
10	Solar green houses
11	Solar power plants
12	Solar water and air heating systems
13	Spacecraft thermal systems
14	Thermal comfort in vehicles
15	Thermal protection of electronic devices (integrated in the appliance)
16	Thermal protection of food: transport, hotel trade, ice-cream, etc.
17	Thermal storage of solar energy for electricity generation

2.13 Summary

This literature study reviewed the solar energy resources available in Africa & South Africa. South Africa receives an abundance of solar radiation with a high DNI necessary for CSP systems to peak performance. The various of CSP systems, Thermal energy storage technologies, performance enhancement techniques, and classes of PCMs available for latent heat storage.

CHAPTER THREE

3. Theoretical Formulation

3.1 Heat Transfer Mechanisms in Cascade LHTES

In latent heat thermal energy storage units, a cascaded arrangement of numerous PCMs with various melting points can be used to improve the efficiency of LHS when a substantial temperature differential storage system is required. The use of numerous phase change materials (PCMs) in a cascading arrangement improves the thermal performance of an LHS system by ensuring that the temperature difference between the phase change materials and the heat transfer fluid remains almost constant during melting and solidification.

For solar applications, thermal energy enter the LHS system via conduction and convection from a chosen heat transfer fluid which receives heat via solar radiation. Heat losses via conduction and convection from the system can be mitigated using insulating material around the TES vessel that houses the cascaded encapsulated PCMs. For optimal heat transfer to the PCMs, encapsulation materials with high thermal conductivity and low volumetric thermal expansivity are to be employed. Spherical encapsulation will be taken into consideration as the based encapsulation geometry of this study.

3.1.1 Conduction

This heat transfer mechanism occurs between the PCM and the walls of the spherical encapsulation. The steady state of heat conduction through a hollow spherical encapsulation with an inner radius of r_1 and an outer radius of r_2 and composed of a material with a constant thermal conductivity k. The temperatures of the inner and outer surfaces are kept constant, but they are at different temperatures T_1 and T_2 respectively. The geometrical symmetry of the heat flow shows that it is restricted to the radial direction exclusively [60]. During the charging cycle, the temperature T_2 at the outer surface is greater than temperature T_1 at the inner surface, the heat flows radially inwards and vice versa during the discharge cycle. Applying Fourier's law of heat conduction to the hollow spherical encapsulation, the relationship can be expressed as [60];

$$\dot{Q}_{cond} = \frac{4\pi k(T_2 - T_1)r_1 r_2}{r_2 - r_1} \qquad (3\text{-}1)$$

3.1.2 Convection

Convection and conduction are similar as both heat transfer mechanisms require the presence of a medium. However, they are different in that convection requires the presence of a fluid medium and fluid motion. In this case, convection occurs between the phase change material and the heat transfer fluid through the spherical encapsulation. Heat transfer is enhanced by this fluid motion due to the flowing of warmer and colder volumes of fluid coming into contact with a surface. As a result, the rate of heat transfer through a fluid via convection is greater than the rate of heat transfer via conduction. The rate of heat due to convection is expressed by [61];

$$\dot{Q}_{conv} = hA_s(T_{htf} - T_{pcm}) \tag{3-2}$$

The heat transfer coefficient *h* depends on the fluid properties and the type of convection (natural or forced).

3.1.3 Radiation

Radiative heat transfer is distinct from conduction and convection in that it can occur in the absence of a medium. Radiation acts as a heat gain mechanism by reflecting and concentrating solar radiation onto the receiver. This energy is then transferred to the heat transfer fluid via conduction through the absorber tubes and into the thermal energy storage system via convective heat transfer between the heat transfer fluid and phase change materials via their encapsulation. The net radiative heat transfer entering the CSP system can be expressed by;

$$\dot{Q} = G_{solar} \cdot \eta_{opt} \cdot A_{concentrator} - A\epsilon\sigma(T_s^4 - T_{amb}^4) \tag{3-3}$$

Where G_{solar} is the solar power constant, η the optical efficiency of the CSP system and *A* is the total area of the concentrator.

3.2 Heat Transfer Analysis of Phase Change Problems

Through a variety of numerical and experimental investigations, the study of the heat transfer characteristics of melting and solidification processes in latent heat thermal energy storage systems has resulted in the development of numerous correlations that relate their thermal performance and dimensionless numbers. The following are the thermal performance parameters for which correlations have been developed:

- PCM Liquefaction Time
- PCM Liquefaction Rate
- Temperature Profile
- Liquid Volume Fraction

Table 3-1: Description of common dimensionless parameters used in the analysis of phase change problems [4] [61]

DIMENSIONLESS PARAMETER	**FORMULA**	**SIGNIFICANCE**
Biot, Bi	$\boldsymbol{Bi = \frac{kl}{\lambda}}$	This is the ratio of the resistance of conductive to convective heat transfer. It establishes the temperature homogeneity of a solid.
Nusselt, Nu	$\boldsymbol{Nu = \frac{kd}{\lambda}}$	This is the ratio of conductive to convective thermal resistance. It quantifies the amount of heat transported by a flowing fluid in comparison to the amount of heat transferred by conduction.
Fourier, Fo	$\boldsymbol{Fo = \frac{\lambda\tau}{\rho c_p l^2}}$	This number characterizes the quantity of heat that is transferred into a body or system per unit area.
Stephan, Ste	$\boldsymbol{Ste = \frac{c_p \Delta t}{L}}$	This is the ratio of the thermal capacity of the melted material and the latent heat of the same material.
Rayleigh, Ra	$\boldsymbol{Ra = \frac{g\beta_t \Delta t l^3}{av}}$	The threshold of convection is determined by this value. Heat transmission is predominantly conduction below a certain value of the Rayleigh number.
Prandtl, Pr	$\boldsymbol{Pr = \frac{a}{v}}$	This is a close approximation of the momentum diffusivity to thermal diffusivity ratio. Effective heat conduction with dominant thermal diffusivity is indicated by a low Pr. Effective heat convection with dominant momentum diffusivity is indicated by a high Pr.
Reynolds, Re	$\boldsymbol{Re = \frac{vd}{v}}$	This is a ratio of inertial to viscous forces. It establishes the laminar or turbulent nature of the flow.
Grashof, Gr	$\boldsymbol{Gr = \frac{g\beta_t \Delta t l^3}{v^2}}$	This approximates the buoyant force to viscous force ratio.

Table 3-2: Correlations for thermal performance derived using dimensionless numbers [4]

CORRELATION	INTERPRETATION OF CORRELATION
$\frac{V}{V_o} = 4.73Fo^{0.906}Ste^{1.538}Ra^{0.002}$	It describes the volume fraction of melted material throughout the course of a test run in terms of Fo, Ste, and Ra.
$\tau_m = \frac{l^2}{2\alpha(1+w)Ste}[1 + (0.25 + 0.17w^{0.7})Ste]$	Duration of the melting process
$\lambda_{eq}(\tau) = 0.228\phi_t Ra(\tau)^{0.25}\left(1 - \frac{d(\tau)}{d}\right)^{0.25}$	Equivalent thermal conductivity
$A(\tau)[1 - lnA(\tau)] = 1 - 4\int_0^{\tau} \lambda_{eq}(\tau)d\tau$	Dimensionless melting rate $[1 - A(\tau)]$

The description of the terms in each of the correlations and dimensionless parameter are in the nomenclature section of this dissertation.

3.3 Formulation of Phase Change Problem

3.3.1 Moving Boundary Conditions

The two thermal processes for latent heat thermal energy storage systems are melting and solidification. The Stefan condition, also known as the moving boundary condition, explains the phase change process of PCMs, which includes shifting the phase border between phases [62]. The PCM phase moves from a solid to a mushy state, then to a liquid state during the melting (charging) process, and vice versa during the solidification (discharging) process [63]. Melting and solidification heat transfer mechanisms can be controlled by conduction, convection, or both at the same time.

The Stephan condition is the most difficult part of addressing liquid-solid phase change problems [55] . Numerical approaches to melting problems can be divided into deforming and fixed grid schemes based on how moving boundary conditions are treated numerically. Rearranging the mesh determines where the interface is located in a deforming grid scheme; however, in a fixed grid scheme, the phase boundary is not explicitly monitored; instead, a phase fraction variable is introduced that is a function of the temperature/enthalpy and determines the phase boundary position [64].

The implicit non-linearity at the moving interfaces (where the rate of displacement is determined by latent heat loss or absorption at the boundary) of phase change systems poses a difficult problem in predicting their behavior [62].

The Stephan condition represented by the differential energy equation describes the phase transition process [41], [63], [65].

$$\boldsymbol{\rho L \frac{ds(\tau)}{d\tau} = k_s \frac{\delta t_s}{\delta \tau} - k_l \frac{\delta t_l}{\delta \tau}} \qquad \textit{(3-4)}$$

Stephan's condition can be solved using boundary integral methods, which are very straightforward to apply and require no mesh adjustment [66]. However, in these methods, the phase change interface moves together with the nodal points which are strictly located on the boundaries.

3.3.2 Formulations of Energy Conservation Equation for Phase Transition Problems

Due to the fact that the solid-liquid boundaries move at a rate defined by the quantity of latent heat received or lost at the boundaries, the analysis of heat transfer problems in phase transition processes is difficult. In order to solve the energy conservation equation, there are several ways for solving phase transition problems, including analytical, experimental, and numerical methods that use one-dimensional, two-dimensional, or three-dimensional models and computational fluid dynamics. Table 3-3 gives some formulations of the energy conservation equation for phase transition problems by various researchers:

Table 3-3: Energy conservation formulations for phase transitions problems [4]

CONSERVATION EQUATION	PARAMETERS DESCRIPTION	REFERENCE
$\frac{\partial t}{\partial \tau} = \frac{a\,\partial}{r^w \partial r}\left(r^w \frac{\partial T}{\partial r}\right)$ $r(\tau) \leq r \leq l;\ \ T = T_{cr};\ \ r \leq r(\tau)$	*$1 + w = lA/V$ with* *$w = 0$ – Insulated PCM slab,* *$w = 1$ – PCM Cylinder* *$w = 2$ – PCM Sphere* *T_{cr} – critical temperature* *r – radius*	[67]
$\frac{\partial h}{\partial \tau} = \frac{1}{r}\frac{\partial}{\partial r}\left(ar\frac{\partial k}{\partial r}\right) + \frac{\partial}{\partial z}\left(a\frac{\partial k}{\partial r}\right) - \rho L\frac{\partial f}{\partial \tau}$	*With phase change: $H(T) = h(T) + \rho_L f(T) L$, $h(T) = \int_{T_m}^{T} \rho c_p dT$, $f(T)$ is the liquid fraction of melted PCM, t_m is the melting temperature and r, z are the radial and axial coordinates respectively*	[68]
$\rho_{HTF} c_{p,HTF}\left(\frac{\partial T_{HTF}}{\partial \tau} + v\frac{\partial T_{HTF}}{\partial x}\right) = \frac{4k}{d}(T_{PCM} - T_{HTF}) + \lambda_{HTF}\frac{\partial^2 T_{HTF}}{\partial x^2}$ and $\frac{\partial h_{PCM}}{\partial \tau} = \frac{1}{r}\frac{\partial}{\partial r}\left(\lambda_{PCM} r \frac{\partial T_{PCM}}{\partial r}\right) + \frac{\partial}{\partial x}\left(\lambda_{PCM}\frac{\partial T_{PCM}}{\partial x}\right)$	*where x and r are the axial and radial coordinates*	[69]
$\rho\frac{\partial H}{\partial \tau} = \frac{1}{r}\frac{\partial}{\partial r}\left(\lambda r\frac{\partial t}{\partial r}\right) + \frac{1}{r}\frac{\partial}{\partial \theta}\left(\frac{\lambda}{r}\frac{\partial T}{\partial \theta}\right)$	*with phase change formula:* *solid region ($t \leq t_m - \varepsilon$): $H = c_p t$,* *interface ($t_m - \varepsilon \leq t_m + \varepsilon$): $H = c_p t + (L/2\varepsilon)t - t_m + \varepsilon$,* *liquid region ($t \geq t_m + \varepsilon$): $H = c_p t + L$* *where r is the radial coordinate, θ is the angular coordinate, and ε is the remittance*	[70]
$c_p\frac{\partial T}{\partial \tau} + c_p\nabla\left(\vec{u}T\right) - \nabla\cdot\left(\frac{\lambda}{\rho}\nabla \mathrm{T}\right) = -L\left(\frac{\partial f}{\partial T} + \nabla\left(\vec{u}f\right)\right)$	*c_p is the mixture heat capacity, T is the temperature, τ is the time, in s; u is the velocity vector, λ is the mixture thermal conductivity, ρ is the mixture density, L is the latent heat of fusion and f is the liquid fraction*	[71]

3.3.3 Numerical Methods for Simulating Phase Transitions

Generally, phase change heat transfer analysis is significantly more complex than single phase heat transfer analysis, owing to the following reasons [4]:

1. Due to the mobility of the solid-liquid interface during phase transition, the problem is nonlinear.
2. Due to buoyancy-driven natural convection in the liquid, there is a dearth of understanding of how heat transfers at the solid-liquid interface.
3. Uncertainty regarding the heat resistance of the container's interaction with the solid PCM
4. Thermal induced volumetric expansivity associated with phase transitions
5. The existence and arrangement of holes in a solid
6. The flow problems connected with HTF

As a result, numerical methods such as the enthalpy formulation, the effective heat capacity method, or the temperature-transforming model are frequently used to describe phase changes.

The enthalpy formulation technique is the most appropriate for most applications, provided that the numerical scheme at the interface remains unchanged. This is a widely used technique for solving the phase transition problem in a fixed domain. This technique has the major advantage of obviating the requirement for explicit treatment of the moving boundary [72].

The enthalpy is considered as a dependent variable in the enthalpy formulation approach, and the latent heat flow is expressed in terms of the volumetric enthalpy H as a function of the PCM temperature t, the only unknown variable [73] [74].

$$\frac{\partial H}{\partial \tau} = \nabla\big(\lambda(\nabla T)\big) \qquad \textit{(3-5)}$$

The phase transition problem is greatly simplified when utilizing an enthalpy technique because the governing equations for the two phases are identical; interface conditions are automatically established, resulting in the production of a mushy zone between the two phases. There are no sharp discontinuities in this zone that could cause numerical instability. As a result, the model's efficacy is dependent on the thickness and quality of this mushy zone's discretization [75].

The main advantages of the enthalpy method are as follows;

- The governing equation is analogous to that of a single phase.
- There is no criterion to satisfy at the solid-liquid interface because the interface condition is met automatically.
- The enthalpy formulation permits the existence of a mushy phase between the two phases.

The effective heat capacity technique approximates the phase change material's latent heat capacity during the phase change process across a phase change temperature interval by taking into account the effective heat capacity of the phase change material. The effective heat capacity of a phase change material is proportional to the amount of energy gained or released during the phase transition process, but not to the temperature range in which the material is melted or solidified during the process [76].

In the temperature transforming model, the apparent heat capacity and enthalpy formulation approaches are combined to generate a hybrid model.

3.3.4 Solution Techniques for Simulation Models

Analytical and numerical methods are the proven methods to solving simulation models. The analytical techniques employed provide approximate solutions. The table highlights the various approximate analytical techniques;

Table 3-4: Approximate Analytical Solution Methods

METHOD	**APPROXIMATE SOLUTION METHOD**	**REFERENCE**
Analytical	*Heat Balance Integral*	[77]
	Variational Technique	
	Isothermal Migration	[78]
	Source and Sink Method	[79]
	Perturbation Method	[80]
	Periodic Solution	[81]

One common problem of these approximate techniques is that they are limited to one-dimensional analysis and become extremely difficult to apply when dealing with multidimensional scenarios.

When it comes to solving simulation models, numerical methods are more powerful. Finite difference, finite element, and finite volume are examples of such methods. The numerical approaches are designed to assist in the resolution of specific PCM problems as well as the characterization of new or prospective materials. The use of computational fluid dynamics (CFD), which is based on the finite volume technique, has the highest potential in the current research in this field, according to the latest findings.

3.4 Mathematical Modelling of Phase Change Problems

3.4.1 Numerical Methods for Simulating Phase Transitions in spherical PCM packed bed systems

Despite the experimental findings, the complicated transient nature of the latent packed bed thermal energy storage system, as well as the prohibitively high cost of set ups, necessitate the use of numerical models to completely analyze the system's performance and determine its capabilities. Many approaches for forecasting the thermal performance of a packed bed Latent Heat Thermal Energy Storage (LHTES) system, which is composed of a cylindrical tank filled with spheres containing phase change materials, have been developed in response to this constraint [82]. These numerical models that have be derived for this purpose can be mainly divided into two groups [83];

1. **Single phase model:** This model is ideal for studying fixed beds with large thermal conductivity and thermal capacity than the working fluid. In this instance, the instantaneous temperatures of both the solid and liquid phases are identical [84]. The solid and fluid phases are treated as a single phase in this model since their instantaneous temperatures are identical, and so both phases are discretized wholly. The energy equation can be expressed thus [82];

$$\boldsymbol{\epsilon \cdot \rho_{HTF} \cdot c_{p,f} \cdot \frac{\partial T}{\partial \tau} + (1-\epsilon)\rho_{PCM}\frac{\partial H}{\partial \tau} + \rho_f \cdot c_{p,f} \cdot u \cdot \frac{\partial T}{\partial y} = +k_{eff,r}\left(\frac{\partial^2 T}{\partial r^2} + \frac{\partial T}{2 \cdot \partial r}\right)} \qquad \textit{(3-6)}$$

   The first two terms of the formula represent the heat transfer fluid's accumulative term and the PCM, respectively. The third term reflects the HTF's convective term, the terms on the right of the equality reflect the conduction in the axial and radial direction respectively.

2. **Two phase model**: In this model, the solid and fluid phases are analyzed separately, and the boundary between the solid and fluid contact is defined by Nusselt correlations. There are three distinct two-phase model topologies and they as described thus;
   a. **Schumann's Model** [85]: In this model, heat transfer is assumed to be one-dimensional and does not account for heat conduction in either the fluid or solid phases in any direction. The model solely takes into account convection between solid and liquid phases as well as heat losses to the ambient environment. The energy conservation equations for the HTF (3.6) and solid PCM (3.7) are written independently, as in all two phase models, and must be solved simultaneously.
   b.

$$\boldsymbol{\epsilon \cdot \rho_f \cdot c_{p,f} \cdot \left(\frac{\partial T_f}{\partial \tau} + u\frac{\partial T_f}{\partial y}\right) = h_{PCM-HTF} \cdot \left(T_{PCM} - T_f\right) - U_L \cdot \left(T_f - T_{amb}\right)} \qquad \textit{(3-7)}$$

$$(1-\epsilon)\cdot\rho_{PCM}\cdot\frac{\partial H}{\partial\tau}=h_{PCM-HTF}\cdot\left(T_f-T_{PCM}\right) \tag{3-8}$$

This method's simplicity can be attributed to the use of a lumped capacitance methodology on solid particles and the assumption of convection coefficients that are independent of time and spatial location.

c. **Concentric Dispersion Model** [86]**:** Specifically, this model assumes the packed bed to be an isotropic porous material made up of separate spherical particles that are not connected to one another. Based on the assumption of a thermal gradient within the solid particles and no inter-particle heat transfer, it is only possible for heat to be transferred between the fluid and the bed in this model. This is the only approach that is capable of solving this problem of heat distribution in solid particles. Incorporating axial heat conduction in the heat transfer fluid and/or the PCM is a viable option. Each of the HTF (3-9) and PCM (3.10) at the boundary and each of the PCM inside the sphere (3-11) has its own set of energy conservation equations, which are solved simultaneously.

$$\epsilon\cdot\rho_f\cdot c_{p,f}\cdot\left(\frac{\partial T_f}{\partial\tau}+u\frac{\partial T_f}{\partial y}\right)=\epsilon\cdot k_f\frac{\partial^2 T}{\partial y^2}+h_{PCM-HTF}\cdot\left(T_{PCM}-T_f\right)-U_L\cdot\left(T_f-T_{amb}\right) \tag{3-9}$$

$$(1-\epsilon)\cdot\rho_{PCM}\cdot\frac{\partial H}{\partial\tau}=(1-\epsilon)\cdot k_{PCM}\frac{\partial^2 T}{\partial y^2}+h_{PCM-HTF}\cdot\left(T_f-T_{PCM}\right) \tag{3-10}$$

$$\rho_{PCM}\cdot\frac{\partial H}{\partial\tau}=\frac{1}{r^2}\cdot\frac{\partial}{\partial r}\left(k_{pcm}\cdot r^2\cdot\frac{\partial T}{\partial\tau}\right) \tag{3-11}$$

If the fluid temperature is considered to be consistent throughout the container, the cylindrical container is divided into elements along its axial axis. A common assumption is that all spheres of the same height behave in the same way; additionally, just one sphere is normally discretized and solved at a time.

d. **Continuous Solid Phase Model** [87]**:** In contrast to a collection of separate solids, it considers the packed bed system to be a continuous porous medium. However, despite the fact that it can examine heat conduction in both the axial and radial directions for both solid and fluid phases, it is typically discretized in one dimension to consider just axial thermal conduction. Each of the energy conservation equations for the fluid PCM (3-12) and solid PCM (3-13) is depicted below and is solved simultaneously [82]

$$\epsilon\cdot\rho_{HTF}\cdot c_{p,f}\cdot\left(\frac{\partial T_f}{\partial\tau}+u\frac{\partial T_f}{\partial y}\right)=k_{f,y}\frac{\partial^2 T}{\partial y^2}+k_{f,r}\left(\frac{\partial^2 T}{\partial r^2}+\frac{\partial T}{r\cdot\partial r}\right)+h_{PCM-HTF}\cdot\left(T_{PCM}-T_f\right)-U_L\cdot\left(T_f-T_{amb}\right) \tag{3-12}$$

$$(1-\epsilon)\cdot\rho_{PCM}\cdot\frac{\partial H}{\partial\tau}=k_{PCM,y}\frac{\partial^2 T}{\partial y^2}+k_{PCM,r}\left(\frac{\partial^2 T_{PCM}}{\partial y^2}+\frac{\partial T_{PCM}}{r\cdot\partial r}\right)+h_{PCM-HTF}\cdot\left(T_f-T_{PCM}\right) \qquad (3\text{-}13)$$

The Table 3-5 presents the drawbacks of employing the aforementioned numerical models.

Table 3-5: Limitations of Numerical Models [82]

MODEL	**LIMITATIONS**
Single Phase	*In order for HTF and PCM to have the same instantaneous temperature, the underlying assumption of same instantaneous temperature is only valid when using solid particles with extremely high thermal conductivities.*
Schumann's	*The inability to account for thermal diffusion within solid particles has resulted in no temperature gradients being considered in the spheres, and heat conduction being eliminated from the model due to the fact that convection is the dominant driver of heat transmission.*
Concentric dispersion	*Increased computational costs*
Continuous solid phase	*Increased computational cost when modeling 2-D heat transfer and an inability to model thermal gradients inside the particles*

3.4.2 Heat Transfer Simulation Model in Two-Dimensions

There are two primary methods for simulating 2-D heat transfer for phase transitions. They include;

i. **Enthalpy Formulation:** As previously described, the enthalpy function is a function of temperature [88]. The energy conservation of a phase transition process can be quantified mathematically in terms of the total volumetric enthalpy and temperature for constant thermophysical properties, as given in the equation [75] [89]:

$$\frac{\partial H}{\partial \tau} = \nabla(\lambda_k(\nabla T)) \qquad \textit{(3-14)}$$

The volumetric enthalpy of PCM is equal to the sum of its sensible and latent heat and is given by the following expression [41]:

$$H\,(T) \;=\; h\,(T) \;+\; \rho_L f\,(T)\,L \qquad \textit{(3-15)}$$

The sensible volumetric enthalpy is given as **[75]**:

$$h(T) = \int_{T_m}^{T} p_k c_{p,k} dT \qquad \textit{(3-16)}$$

For isothermal phase transition, the liquid fraction of the melted PCM [90] is expressed as:

$$f(T) = \begin{cases} 0, & T < T_m\,(solid) \\ 0-1, & T = T_m\,(mushy) \\ 1, & T > T_m\,(liquid) \end{cases} \qquad \textit{(3-17)}$$

Following the above equations, the enthalpy of the PCM can be expressed for different temperature thresholds by [4]:

$$H = \begin{cases} \int_{T_m}^{T} \rho_s c_s dT\,, & T < T_m\,(solid) \\ \rho_l f L, & T = T_m\,(melting) \\ \int_{T_m}^{T} \rho_l c_l dT + \rho_l L\,, & T > T_m\,(liquid) \end{cases} \qquad \textit{(3-18)}$$

Alternatively, the energy conservation equation for a two dimensional heat transfer in the PCM and HEX container material can be expressed in differential form respectively as [4]:

$$\frac{\partial h}{\partial \tau} = \frac{\partial}{\partial x}\left(\alpha \frac{\partial h}{\partial x}\right) + \frac{\partial}{\partial y}\left(\alpha \frac{\partial h}{\partial y}\right) - \rho_l L \frac{\partial f}{\partial \tau} \qquad \textit{(3-19)}$$

$$\frac{\partial h_f}{\partial \tau} = \frac{\partial}{\partial x}\left(\alpha_f \frac{\partial h}{\partial x}\right) + \frac{\partial}{\partial y}\left(\alpha_f \frac{\partial h}{\partial y}\right) \qquad \textit{(3-20)}$$

ii. **Numerical solution:** The energy conservation problem can be solved using the control volume discretization technique [88]. The domain is divided into elementary control volumes, which are then utilized to integrate the equation after they have been separated [4]. In the PCM, the differential variant of the energy conservation equation for a two-dimensional heat transfer is solved using a fully implicit finite difference method. The finite difference equation for PCM is accomplished by integrating (3-15) across each control volume. The discretization of (3-15) for Δx = Δy leads to the following scheme [4]:

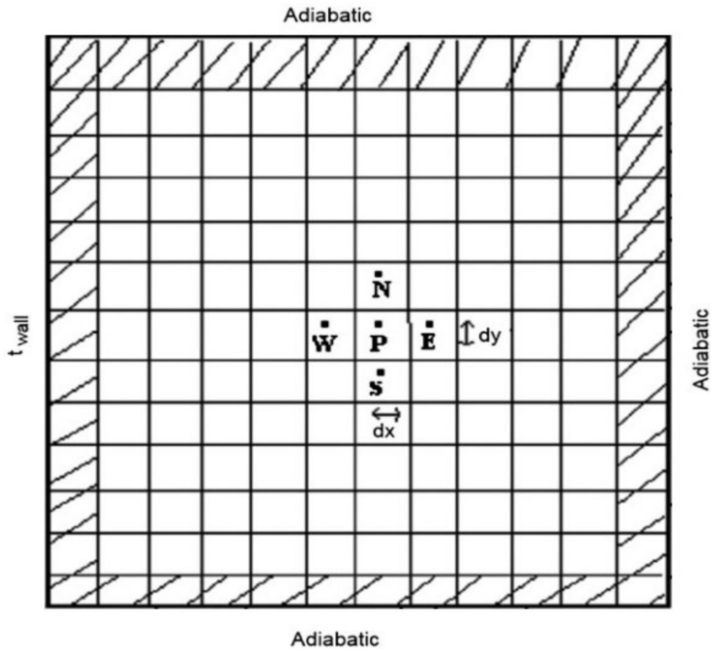

Figure 3-1: Two-Dimensional Domain [43]

$$\boldsymbol{h_P = h_P^0 + \alpha R(h_E - 4h_P + h_W + h_N + h_S) + \rho_l L(f_P^0 - f_P^k)} \qquad \textit{(3-21)}$$

$$\boldsymbol{a_E h_E + a_W h_W + a_N h_N + a_s h_S = Q} \qquad \textit{(3-22)}$$

where:

$$\boldsymbol{a_E = a_W = a_N = a_s = -\alpha R} \qquad \textit{(3-23)}$$

$$\boldsymbol{a_P = 1 - a_W - a_N - a_s - a_E - a_P} \qquad \textit{(3-24)}$$

$$\boldsymbol{Q = h_P^0 + \rho_l L\left(f_P^0 - f_P^k\right),\ \ R = \frac{dT}{(dx)^2}} \qquad \textit{(3-25)}$$

The superscript (^{0}) indicate quantities from a previous time step, and the subscripts W, E, P, N, S indicate the cardinal directions with P as the center. Using a matrix technique with three diagonals, it is possible to solve equation (3-22) completely. The source term Q, which keeps track of the evolution of latent heat, is a basic component of the current fixed grid enthalpy approach, and the melt fraction is the driving factor [4]. The enthalpy equation solution is used to repeatedly compute the value of this parameter. If phase transition occurs around the P_{th} node, the melt fraction can be represented as:

$$\boldsymbol{f_P^{k+1} = \frac{-a_E h_E - a_W h_W - a_N h_N - a_s h_S + h_P^0}{\rho_l L + f_P^0}} \qquad \textit{(3-26)}$$

$$\boldsymbol{f = \begin{cases} 0, & if\ (f)^{k+1} \leq 0 \\ 1, & if\ (f)^{k+1} \geq 1 \end{cases}} \qquad \textit{(3-27)}$$

In order for convergence to be achieved at a given time step, the difference in the total enthalpy fields must be less than or equal to a permissible error.

3.4.3 Heat Transfer Simulation Model in Three-Dimensions

Simulating phase transitions Material heat transfer within a given range of phase change temperatures requires a numerical technique that frequently leverages the enthalpy-porosity concept to account for the solid-liquid interface. This technique includes a mixed solid-liquid phase area during the phase change. The region is described by a parameter called liquid fraction, which has a value between 0 and 1. The porosity effect is found to be equivalent to that of the porous media's liquid volume component in the mushy zone [88]. Computational fluid dynamic software such as Fluent, is used to conduct the numerical calculations because of the increased complexity of a 3-D model.

The following assumptions are taken into account for simplicity of the model [4]:

a. The axial conduction and viscous dissipation of the fluid are extremely minimal and are therefore neglected.
b. Both the phase change material and the porous matrix material are homogeneous and isotropic.
c. Temperature has no effect on the thermophysical properties of the PCM and HTF; nevertheless, the properties of the PCM in the solid and liquid phases may differ.
d. This model is based on the assumption that the PCM has a single mean melting temperature T_m
e. Radiant heat transfer has a negligible effect.

CHAPTER FOUR

4. Simulation and Validation Study

4.1 Overview of Computational Fluid Dynamics Analysis

4.1.1 Background of Computational Fluid Dynamics (CFD)

Using computer-based simulations and numerical algorithms, computational fluid dynamics (CFD) has proven to be extremely useful in the analysis of systems involving heat transfer, fluid flow, and related phenomena. Computational fluid dynamics (CFD) is a mathematical technique that predicts the behavior and properties of a system by solving the set of governing mathematical equations such as conservation of mass, momentum, energy, and species, as well as related phenomena. Due to the increasing levels of computing power and availability of commercial CFD packages, CFD modelling, and simulation techniques have become powerful and ubiquitous for industrial and non-industrial applications. CFD helps to overcome design and experimental cost constraints as well as have a substantial reduction in lead times [91].

The results of CFD analyses are useful in a variety of situations such as:

- New design conceptual studies
- Product development in great detail
- Redesign
- Troubleshooting

The fluid flow problem is governed by the continuity, conservation of mass, Navier-Stokes and energy equations. Analytical approaches can produce extremely few solutions due to the non-linear components in these equations. Discretization converts the differential equations regulating fluid flow into a set of algebraic equations that may be solved numerically to yield an approximate solution. CFD has a number of distinct advantages over experiment-based approaches to fluid system design [92]:

- Significantly reduced lead times and expenses associated with new design
- Capacity to investigate systems in which controlled experiments are difficult or impossible
- Capacity to investigate hazardous conditions within and beyond the regular operating limitations of a system
- Results are practically limitless in their level of detail

CFD codes are based on numerical algorithms for solving problems involving fluid flow. To render their problem-solving capability more accessible, all commercial CFD software includes sophisticated user interfaces for entering problem parameters and examining the results. As a result, all code comprises three components: (a) a preprocessor, (b) a solver, and (c) a postprocessor are required [93].

4.1.2 Methodology for the CFD Analysis of the packed bed latent heat thermal energy storage systems

For this research, the simplified three dimensional domain of the 3-stage cascade latent heat thermal energy storage system is a closed system that consist of a cylindrical tank, heat transfer fluid domain, spherical encapsulation and phase change materials. These steps summarize the methodology employed in this CFD analysis:

- Definition of computational domain geometry
- Discretization (meshing) of computational domain. The meshing may be uniform or non-uniform
- Definition of physical models relevant to the simulation
- Definition of boundary and initial conditions since phase transitions problems are transient
- Define convergence conditions
- Initiating simulation, which solves the governing equations iteratively as transient
- Post-processing simulated results for analysis and visualization

4.2 Computational Fluid Dynamics Modeling of LHTES

The commercial CFD package is utilized for the transient simulation of the 3-stage cascade packed bed latent heat thermal energy storage system that employ PCM encapsulation.

4.2.1 System Configuration

The computational domain to be modelled will consist of packed bed cylindrical tank filled with an array of encapsulated PCM. A cylindrical tank design for the packed bed was selected as a result of several factor which include; uniform cross-sectional area across the length the bed, ease of insulation, even stacking of the PCMs encapsulations within tank and the circular cross-section allows for consistent strength across the length of the cylinder under high pressure conditions. The 3D geometry of the packed bed was generated by ANSYS Space Claim software. The spherical capsule design will be the base model design. Other capsule designs will be of the same volume as the spherical design to ensure accurate results and zero discrepancies during the comparative data analysis.

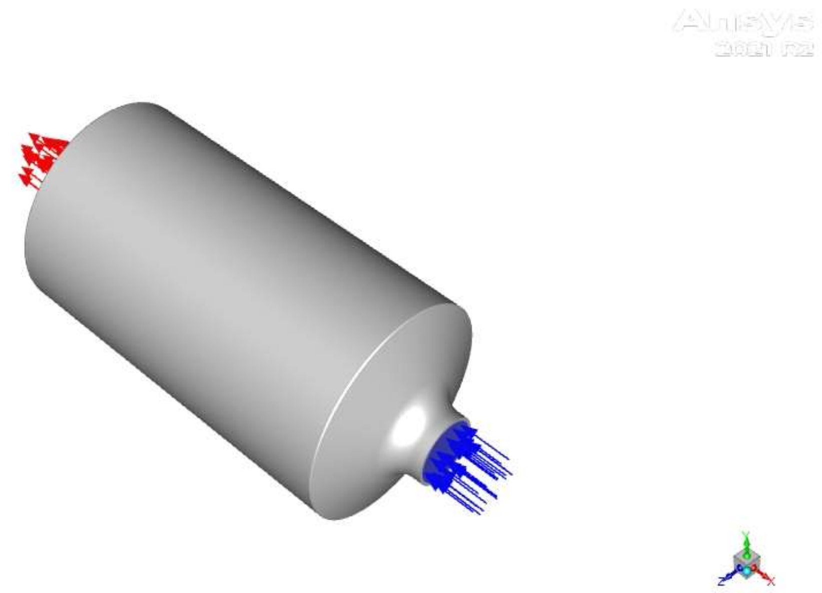

Figure 4-1: 3D Rendering of a packed bed thermal energy storage system

These new capsule geometries are developed to increase the surface area of heat transfer along the flow direction as well as improve the flow characteristics around capsules. The capsules arrangements in the tank will be in the two layouts described as follows;

- **Layout 1:** The PCM capsules are arranged in a concentric circular array and are separated by 2 mm from each other in the radial and axial/ flow directions. There are nine sets of encapsulation arrays along the flow direction and each PCM will occupy three sets of the encapsulation array respectively. The capsules containing the KNO_3 PCM (mid-section) is rotated 15^0 for the normal. Each circular array consists of 19 PCM encapsulations arranged in 1-6-12 formation from the center.

- **Layout 2:** The PCM capsules are arranged in a concentric circular array and are separated by 2 mm from each other in the radial directions. There are nine sets of encapsulation arrays along the flow direction and each PCM will occupy three sets of the encapsulation array respectively. Each circular array consists of 19 PCM encapsulations arranged in 1-6-12 formation from the center for odd numbered arrays and 2-9-8 formation for even numbered arrays. The odd numbered encapsulation are similar to the layout 1 configuration save for the mid-section 15^0 rotation. The even numbered encapsulation however deviate as the align to the midpoint of the interstices odd numbered encapsulations.

Table 4-1: Bed Length Change Percentage Between Layouts

S/N	ENCAPULSATION GEOMETRY	LAYOUT 1 BED LENGTH (mm)	LAYOUT 2 BED LENGTH (mm)	%LENGTH CHANGE
1	***Sphere***	*245*	*216.52*	*-11.62%*
2	***Cylinder-Sphere Hybrid***	*314.39*	*288.39*	*-8.27%*
3	***Elliptical Torus***	*330.85*	*330.85*	*0.00%*
4	***Ellipsoid***	*371.56*	*326.28*	*-12.19%*
5	***Ovaloid***	*451.28*	*451.28*	*0.00%*
6	***Half Capped Cone***	*473.69*	*432.56*	*-8.68%*
7	***Double Arc-Edged Cone***	*474.05*	*407.57*	*-14.02%*
8	***Bi-Triangular Torus***	*508.28*	*508.28*	*0.00%*
9	***Top Curved Cone***	*589.61*	*447.05*	*-24.18%*

Table 4-2: Bed Diameter Change Percentage Between Layouts

S/N	ENCAPULSATION GEOMETRY	LAYOUT 1 BED DIAMETER (mm)	LAYOUT 2 BED DIAMETER (mm)	% DIAMETER CHANGE
1	***Sphere***	*137*	*164*	*19.71%*
2	***Bi-Triangular Torus***	*112*	*134*	*19.64%*
3	***Cylinder-Sphere Hybrid***	*112*	*134*	*19.64%*
4	***Double Arc-Edged Cone***	*112*	*134*	*19.64%*
5	***Ellipsoid***	*112*	*134*	*19.64%*
6	***Elliptical Torus***	*112*	*134*	*19.64%*
7	***Half Capped Cone***	*112*	*134*	*19.64%*
8	***Top Curved Cone***	*112*	*134*	*19.64%*
9	***Ovaloid***	*99.8*	*119.34*	*19.58%*

Nine (9) models have been generated using Ansys Space-Claim and they are described as follows:

Spheres: This PCM encapsulation which will serve as a baseline for all the encapsulation designs as it is currently used in the industry practice. The spheres are of 25mm diameter, arrayed along the axial direction of the for each of the PCMs. The total area and volume provided per capsule by this encapsulation 1963.50mm^2 and 8181.23mm^3. Figure 4-2 shows the array of the described encapsulations in the 2 layouts.

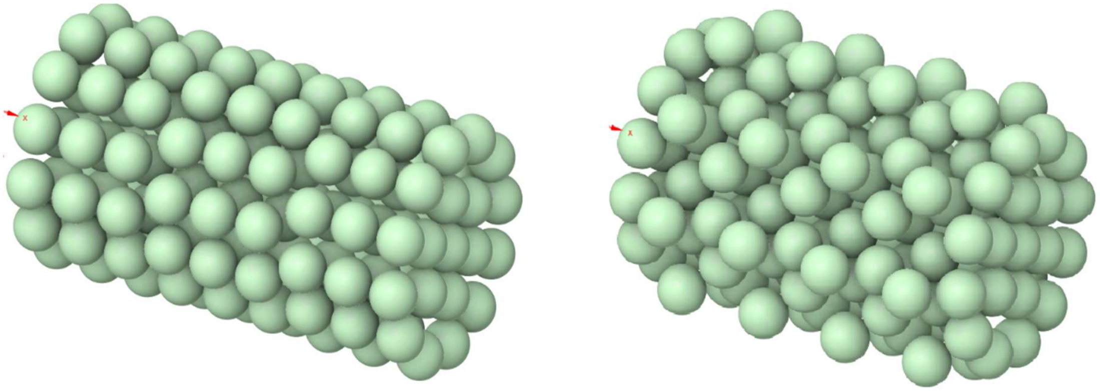

Figure 4-2: Sphere Encapsulation Array in Layout 1 & 2

Cylinder-Sphere Hybrids: This design incorporates a short cylinder capped with 2 hemispheres on each end. It improves the total area per capsule by 4.67% for the same volume of the spherical encapsulation and a corresponding increase in bed length. The dimensions of the capsule are given in Table 4-3. Figure 4-3 shows the array of the described encapsulations in the 2 layouts.

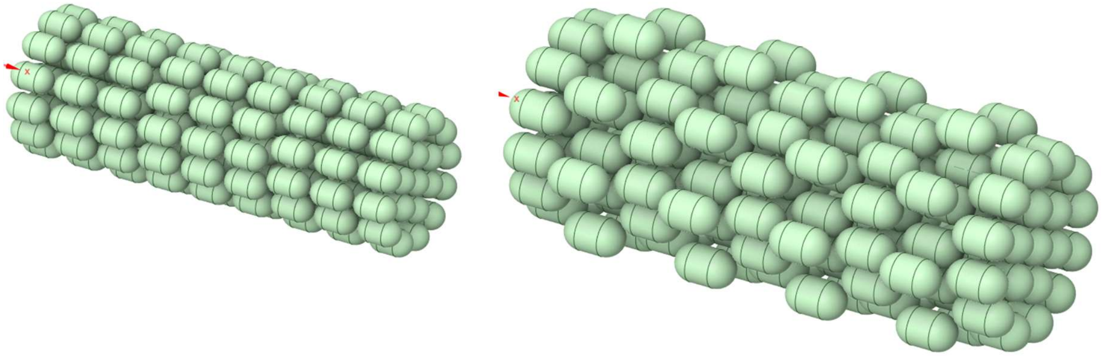

Figure 4-3: Cylinder-Sphere Hybrids Encapsulation Array in Layout 1 & 2

Ellipsoids: This capsule is an ellipse of revolution around the central major axis. The dimensions of the semi-major and semi-minor axis are given in Table 4-3. It improves the total area per capsule by 7.12% for the same volume of spherical encapsulation and a corresponding increase in bed length. Figure 4-4 shows the array of the described ellipsoids.

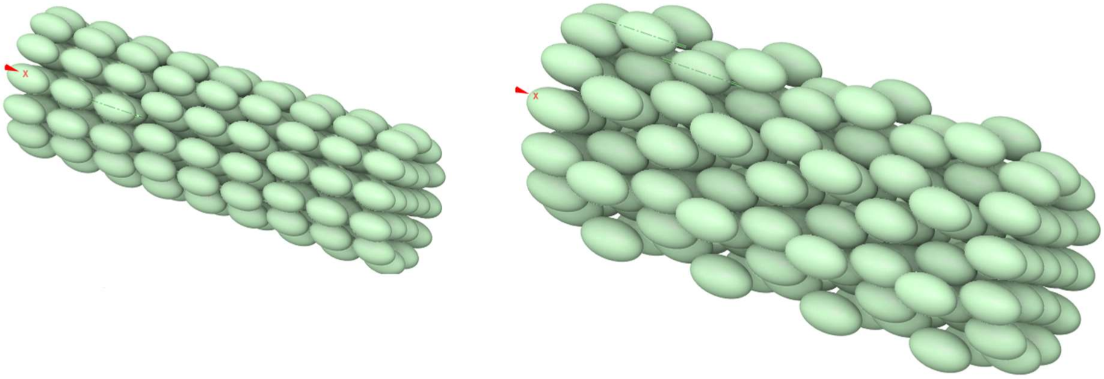

Figure 4-4: Ellipsoid Encapsulation Array in Layout 1 & 2

Half Capped Cones: This capsule consists of two base-jointed conical frustums with two spherical caps at the midpoints of the slant heights. The base radius and height of the conical frustum as well as the spherical cap radius and cap height are given in Table 4-3. It improves the total area per capsule by 22.83% for the same volume of spherical encapsulation and a corresponding increase in bed length. Figure 4-5 shows the array of the described encapsulations in the 2 layouts.

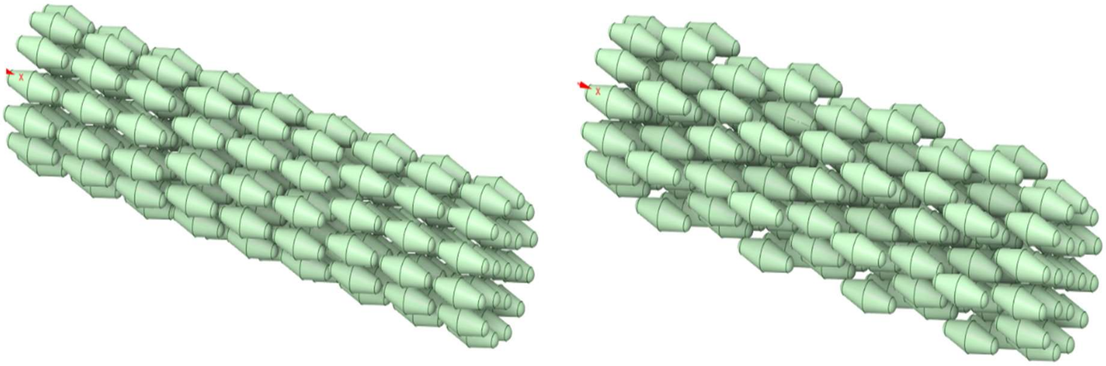

Figure 4-5: Half Capped Cone Encapsulation Array in Layout 1 & 2

Double Arc Capped Cone: This capsule is a composite solid that consists of two conical frustums with two spherical caps at the lower radius end and the bases are joined by an arc segment of revolution around the central axis of the composite geometry. The base radius and height of the conical frustum as well as the spherical cap radius, cap height and arc segment area are given in the Table 4-3. It improves the total area per capsule by 24.26% for the same volume of spherical encapsulation and a corresponding increase in bed length. The figure below shows the array of the described encapsulations in the 2 layouts.

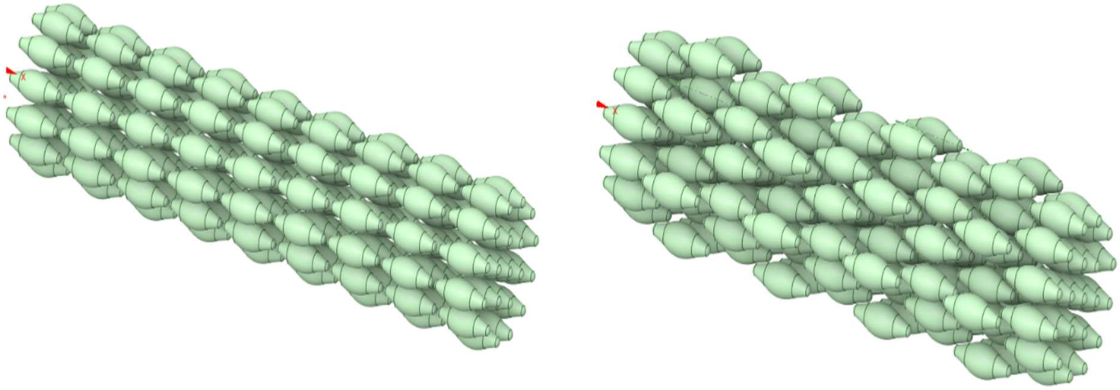

Figure 4-6: Double Arc Capped Cone Encapsulation Array in Layout 1 & 2

Ovaloid: This capsule is a solid of revolution developed revolving an arc segment around a central axis and capping its end with spherical caps. The overall solid approximated and oval of revolution. The arc segment area and spherical cap radius and height are given in Table 4-3. It improves the total area per capsule by 27.39% for the same volume of spherical encapsulation and a corresponding increase in bed length. Figure 4-7 shows the array of the described encapsulations in the 2 layouts.

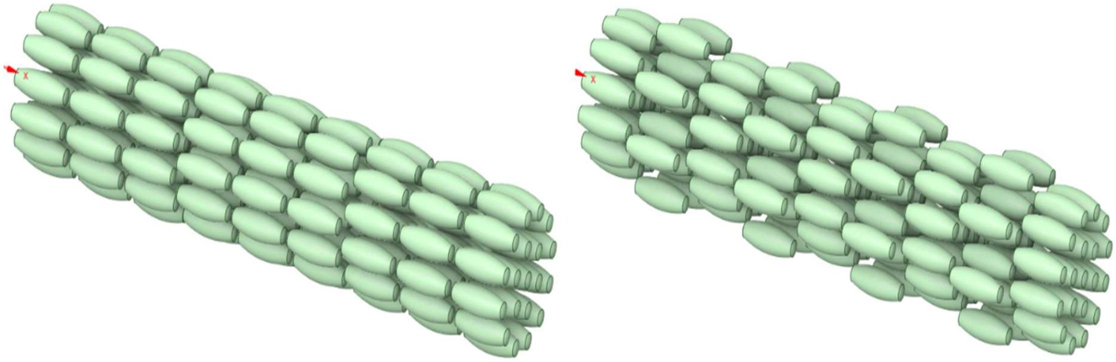

Figure 4-7: Ovaloid Encapsulation Array in Layout 1 & 2

Top Curved Cones: This capsule is a solid of revolution developed making arcs between the mid-points of the hypotenuses of the triangular cross-section of two base-jointed triangles and revolving around the central axis of the area formed. The base, height of the triangular cross-sections and segment are given in Table 4-3. It improves the total area per capsule by 27.39% for the same volume of spherical encapsulation and a corresponding increase in bed length. Figure 4-8 shows the array of the described encapsulations in the 2 layouts.

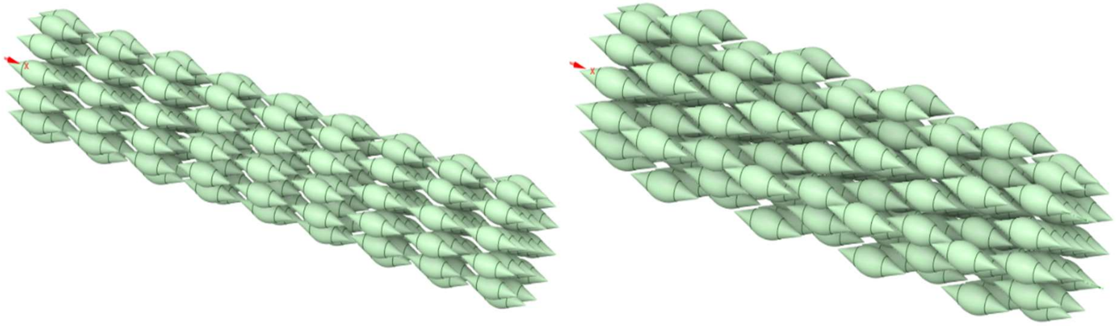

Figure 4-8: Top Curved Cone Encapsulation Array in Layout 1 & 2

Elliptical Torus: This capsule is a solid of revolution developed by revolving an elliptical cross-sectional area around an axis parallel to the major axis of the elliptical cross-section. The distance between the center of the ellipse and the parallel axis is called the radius of gyration (R_G). This capsule design supports flow across inner and outer faces simultaneously. The dimensions of the semi-major, semi-minor axis and radius of gyration are given in Table 4-3. It improves the total area per capsule by 41.12% for the same volume of spherical encapsulation and a corresponding increase in bed length. Figure 4-9 shows the array of the described encapsulation.

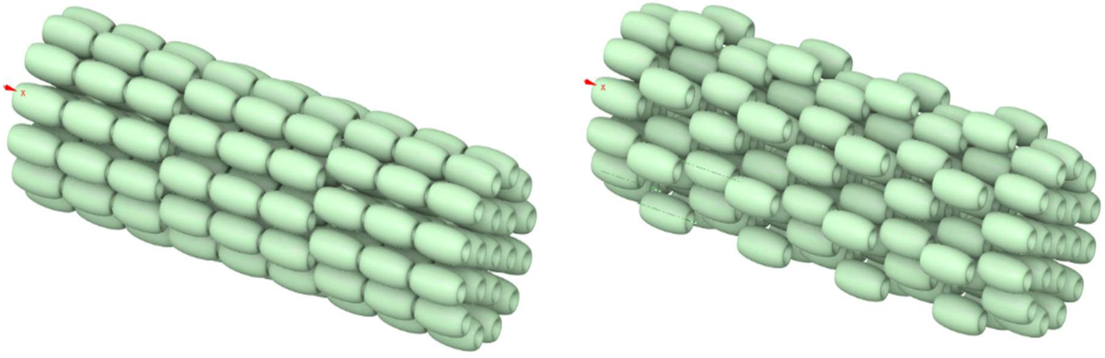

Figure 4-9: Elliptical Torus Encapsulation Array in Layout 1 & 2

Bi-Triangular Torus: This capsule is a solid of revolution developed by revolving an two base-jointed triangular cross-sectional area around an axis parallel to the height of the triangular cross-section. The distance between the center of the triangular cross-sections and the parallel axis is called the radius of gyration (R_G). This capsule design also supports flow across inner and outer faces simultaneously to a wider degree. The dimensions of the base, height and radius of gyration are given in Table 4-3. It improves the total area per capsule by 110.59% for the same volume of spherical encapsulation and a corresponding increase in bed length. This capsule has the maximum area achieved by any of the geometries developed. Figure 4-10 shows the array of the described encapsulation.

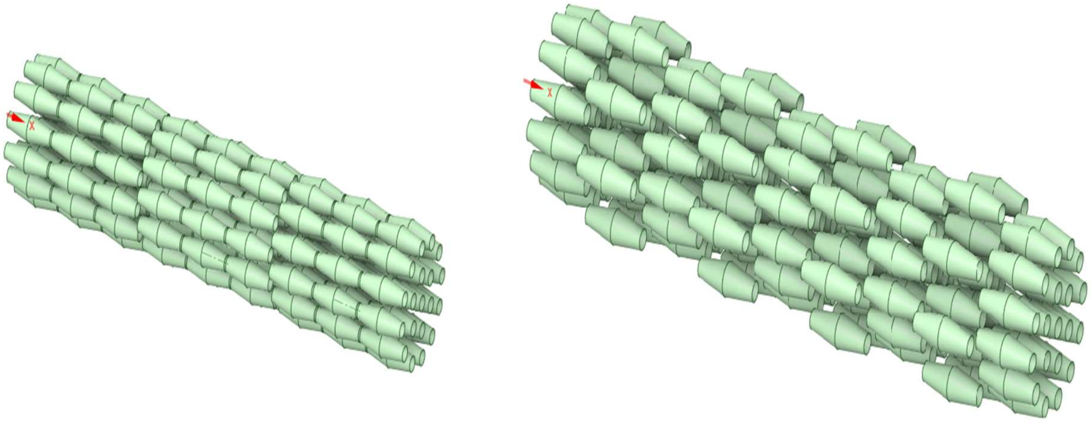

Figure 4-10: Bi-Triangular Torus Encapsulation Array in Layout 1 & 2

Table 4-3: Capsule Volume Equations and Dimensions

S/N	CAPSULE GEOMETRY	CAPSULE VOLUME EQUATION	GIVEN PARAMETERS	PARAMETER DEFINITION
1	***Sphere***	$V = \frac{4}{3}\pi r^3$	$r = 12.5mm$	r – sphere radius
2	***Cylinder-Sphere Hybrid***	$V = \frac{4}{3}\pi r^3 + \pi r^2 h$	$r = 10mm$, $h = 12.71mm$	r – sphere/ cylinder radius, h – height of cylinder
3	***Ellipsoid***	$V = \frac{4}{3}\pi abc$	$a = c = 10mm$, $b = 19.53mm$	a - semi-minor axis, b - semi-major axis, c - height of ellipsoid
4	***Half Capped Cone***	$V = \frac{2\pi h_f}{3}(R^2 + Rr + r^2) + \frac{\pi h}{3}(3r^2 + h^2)$	$r = 5mm$, $h = 3.88mm$, $R = 10mm$, $h_f = 21.32mm$	R – conical frustum base radius, h_f - frustum height r – spherical cap base/ frustum top radius, h – cap height
5	***Double Arc-Capped Cone***	$V = A_s(2\pi R_G) + \frac{2\pi h_f}{3}(R^2 + Rr + r^2) + \frac{\pi h}{3}(3r^2 + h^2)$	$R = 6.75mm$, $r = 3.38mm$, $h = 2.39mm$, $h_f = 10.332mm$, $R_G = 4.522mm$ $A_S = 223.64mm^2$	R – conical frustum base radius, h_f - frustum height r – spherical cap base/ frustum top radius, h – cap height
6	***Top Curved Cone***	$V = A_T(2\pi R_G)$	$R_G = 3.69mm$ $A_T = 352.85mm^2$	A_T – area under segment + triangular area, R_G – radius of gyration
7	***Ovaloid***	$V = A_s(2\pi R_G) + \frac{\pi h}{3}(3r^2 + h^2)$	$r = 5mm$, $h = 1.89mm$, $R_G = 6.01mm$ $A_S = 310.12mm^2$	A_S – area under segment, R_G – radius of gyration, r – spherical cap base, h – cap height
8	***Elliptical Torus***	$V = \pi ab(2\pi R_G)$	$a = 4mm$, $b = 17.27mm$ $R_G = 6mm$	a - semi-minor axis, b - semi-major axis R_G – radius of gyration
9	***Bi-Triangular Torus***	$V = bh(2\pi R_G)$	$b = 8mm$, $h = 27.13mm$ $R_G = 6mm$	b – base h - height R_G – radius of gyration

Table 4-4: Different views of each Capsule Geometry

S/N	CAPSULE GEOMETRY	PLAN VIEW	ISOMETRIC VIEW	SECTIONAL VIEW
1	*Sphere*	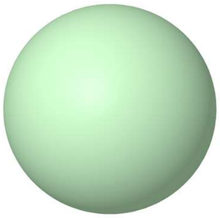	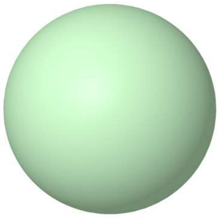	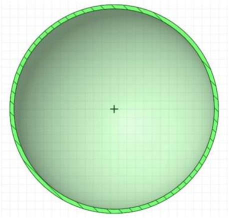
2	*Cylinder-Sphere Hybrid*	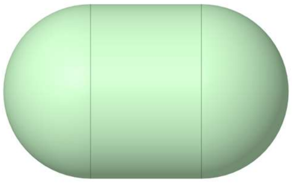	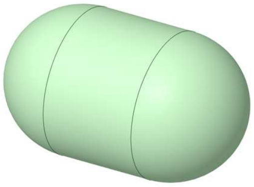	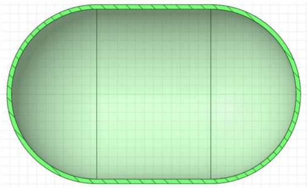
3	*Ellipsoid*	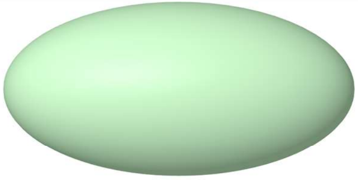	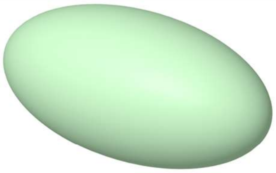	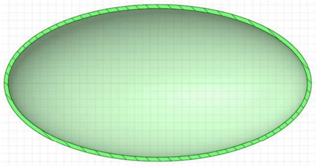
4	*Half Capped Cone*	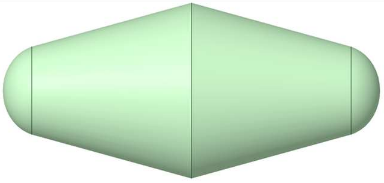	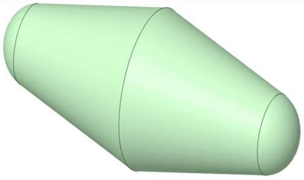	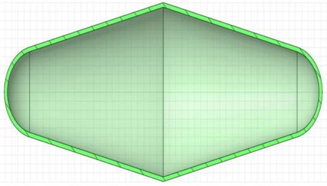
5	*Double Arced Capped Cone*	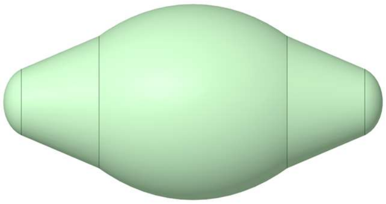	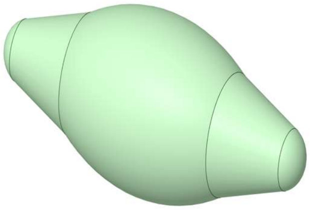	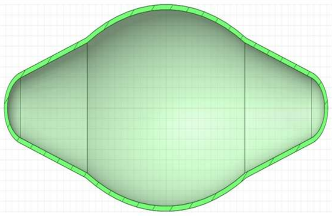
6	*Top Curved Cone*	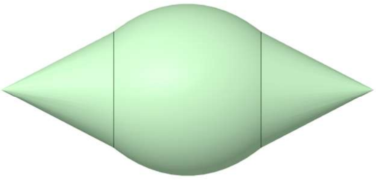	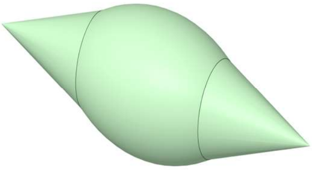	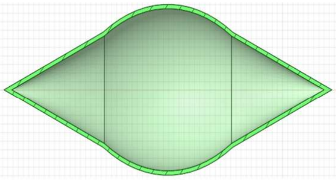
7	*Ovaloid*	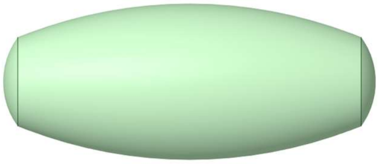	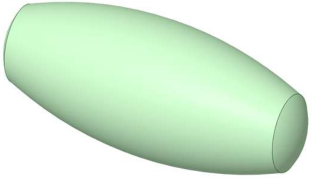	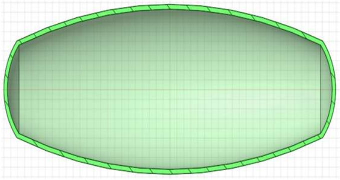

8	*Elliptical Torus*	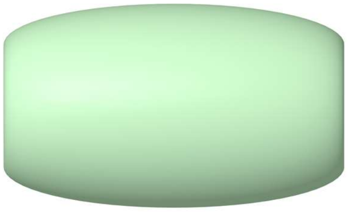	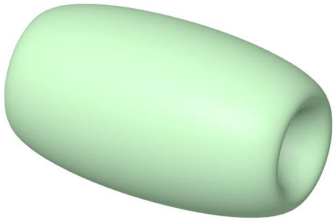	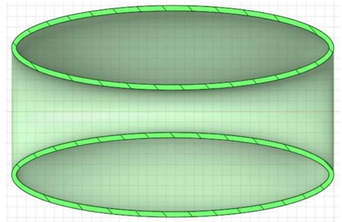
9	*Bi-Triangular Torus*	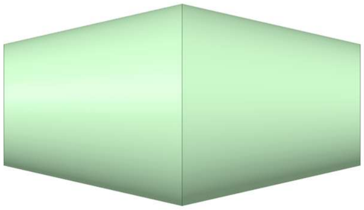	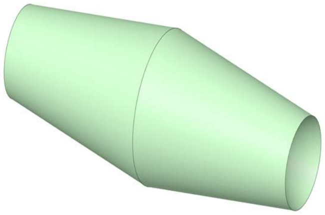	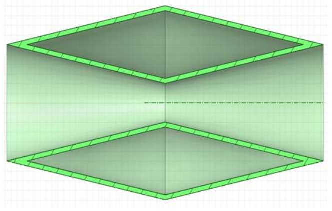

Table 4-5: Percentage Increase in Capsule Surface Area

S/N	ENCAPULSATION GEOMETRY	CAPSULE VOLUME (mm^3)	CAPSULE SURFACE AREA (mm^2)	PERCENTAGE SURFACE AREA INCREASE (%)
1	*Sphere*	*8,181.23*	*1,963.50*	-
2	*Cylinder-Sphere Hybrid*		*2,055.13*	*4.67*
3	*Ellipsoid*		*2,103.39*	*7.12*
4	*Half Capped Cone*		*2,411.74*	*22.83*
5	*Double Arced Cone*		*2,439.91*	*24.26*
6	*Ovaloid*		*2,479.82*	*26.30*
7	*Top Curved Cone*		*2,501.36*	*27.39*
8	*Elliptical Torus*		*2,770.81*	*41.12*
9	*Bi-Triangular Torus*		*4,134.84*	*110.59*

Table 4-6: Bed Length & Diameter Change comparison between Sphere and other encapsulation in Layout 1

S/N	ENCAPULSATION GEOMETRY	BED LENGTH (mm)	% LENGTH INCREASE	BED DIAMETER (mm)	%DIAMETER DECREASE
1	***Sphere***	*245*	-	*137*	-
2	***Cylinder-Sphere Hybrid***	*314.39*	*28.32%*	*112*	*-18.25%*
3	***Elliptical Torus***	*330.85*	*35.04%*	*112*	*-18.25%*
4	***Ellipsoid***	*371.56*	*51.66%*	*112*	*-18.25%*
5	***Ovaloid***	*451.28*	*84.20%*	*99.8*	*-27.15%*
6	***Half Capped Cone***	*473.69*	*93.34%*	*112*	*-18.25%*
7	***Double Arced Cone***	*474.05*	*93.49%*	*112*	*-18.25%*
8	***Bi-Triangular Torus***	*508.28*	*107.46%*	*112*	*-18.25%*
9	***Top Curved Cone***	*589.61*	*140.66%*	*112*	*-18.25%*

Table 4-7: Bed Length & Diameter Change comparison between Sphere and other encapsulation in Layout 2

S/N	ENCAPULSATION GEOMETRY	BED LENGTH (mm)	%LENGTH INCREASE	BED DIAMETER (mm)	%DIAMETER DECREASE
1	***Sphere***	*216.52*	*-*	*164*	*-*
2	***Cylinder-Sphere Hybrid***	*288.39*	*33.19%*	*134*	*-18.29%*
3	***Ellipsoid***	*326.28*	*50.69%*	*134*	*-18.29%*
4	***Elliptical Torus***	*330.85*	*52.80%*	*134*	*-18.29%*
5	***Double Arced Cone***	*407.57*	*88.24%*	*134*	*-18.29%*
6	***Half Capped Cone***	*432.56*	*99.78%*	*134*	*-18.29%*
7	***Top Curved Cone***	*447.05*	*106.47%*	*134*	*-18.29%*
8	***Ovaloid***	*451.28*	*108.42%*	*119.34*	*-27.23%*
9	***Bi-Triangular Torus***	*508.28*	*134.75%*	*134*	*-18.29%*

4.2.2 Material Properties

The thermal differential between the intake temperature of the heat transfer fluid and the PCM fusion temperature has a substantial impact on the latent heat storage performance during the charging and discharging cycles. Phase change material melting can be improved by using many PCMs of decreasing melting temperature in a sequential order, rather than a single PCM with a decreasing temperature differential in the HTF flow direction. The packed bed TES system is used to test three PCMs (KOH, KNO_3, and $NaNO_2$) with melting points more than 300°. These selected PCMs are of the inorganic variety whose characteristics are described in Table 2-2, making them suitable candidates for this high temperature thermal energy storage system. The molten salt mixture (60% wt $NaNO_3$ + 40% wt KNO_3) is employed as the HTF because of its low vapor pressure and thermal stability. PCM capsules and storage tanks are made of stainless steel (SS316), a corrosion-resistant material. The properties of the PCMs and HTF are given in Table 4-8 [94].

Table 4-8: Thermophysical properties of PCMs and HTF

S/N	PARAMETERS	PHASE	$NaNO_2$	KNO_3	KOH	HTF ($60\%NaNO_3+40\%KNO_3$)
1	***Melting Temperature (°C)***	*Solidus*	*277.32*	*333.00*	*378.00*	*N/A*
		Liquidus	*303.65*	*336.00*	*380.00*	
2	***Latent Heat (kJ/kg)***	*N/A*	*199.60*	*266.00*	*149.70*	*N/A*
3	***Specific Heat Capacity (J/kg.K)***	*Solid*	*1,385.00*	*1,439.00*	*1,470.00*	$1443 - 0.172T_{HTF}$
		Liquid	*1,531.00*	*1,480.00*	*1,470.00*	
4	***Density (kg/m3)***	*Solid*	*2,097.00*	*1,900.00*	*2,044.00*	$2090 - 0.636T_{HTF}$
		Liquid	*1,846.00*	*1,890.00*	*2,044.00*	
5	***Heat Conductivity (W/m.K)***	*Solid*	*0.56*	*0.50*	*0.50*	$0.443 - 0.00019\,T_{HTF}$
		Liquid	*0.48*	*0.50*	*0.50*	
6	***Viscosity***	*Liquid*	$0.187118 - 0.876094 \times 10^{-3}T + 1.41024 \times 10^{-6}T^2 - 7.71608 \times 10^{-10}T^3$	$0.0501676 - 0.164572 \times 10^{-3}T + 1.86335 \times 10^{-7}T^2 - 7.12497 \times 10^{-11}T^3$	$0.0527561 - 1.66134 \times 10^{-4}T + 1.80314 \times 10^{-7}T^2 - 6.66494 \times 10^{-11}T^3$	$0.022714 - 1.2 \times 10^{-4}T_{HTF} + 2.281 \times 10^{-7}T_{HTF}^2 + 1.474 \times 10^{-10}T_{HTF}^3$

Table 4-9: Thermophysical properties of SS316 Stainless Steel

S/N	PARAMETERS	PHASE	SS316
1	Specific Heat Capacity (J/kg.K)	Solid	502.48
2	Density (kg/m3)		8,030.00
3	Heat Conductivity (W/mK)		16.27

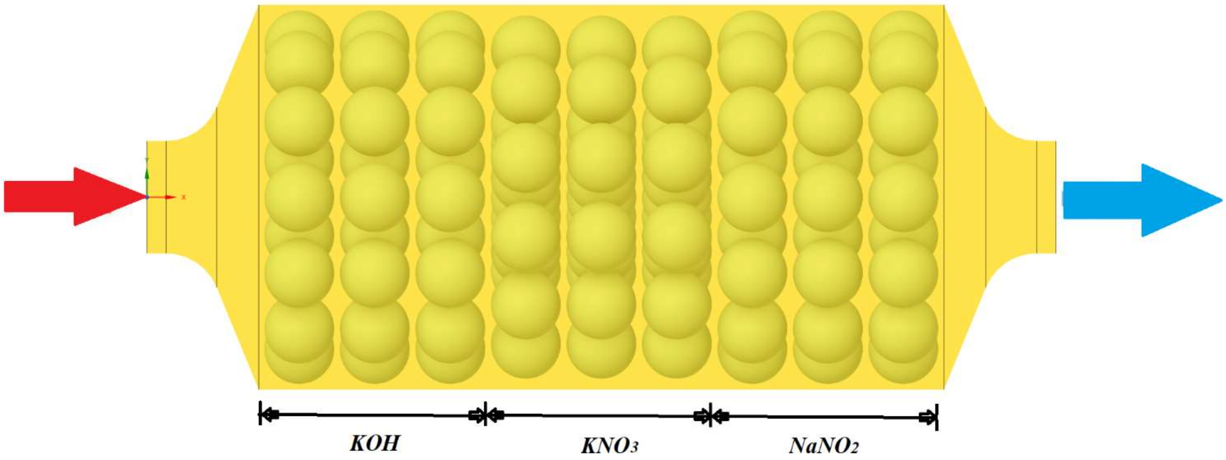

Figure 4-11: Schematic of TES computational domain with PCMs

Molten salts are often utilized for high-temperature TES and the selected PCMs (KOH, KNO_3, and $NaNO_2$) fall into this category. Thermal stability is a major determinant for selecting thermal storage materials as it affects how well a thermal energy storage (TES) system performs. Because nitrate molten salts are thermally stable, heat can be held at a variety of high temperatures.

4.2.3 Governing Equations

Simulating the thermal behavior of a packed bed thermal energy storage system with encapsulated PCM, as described apriori, requires some assumptions to account for the PCM's phase transition and simplification of the 3-D model [95]:

- Due to the isotropic and homogeneous nature of the solid and liquid phases, their thermophysical properties are assumed to remain constant.
- Thermal equilibrium exists at the solid–liquid interface in both phases.
- The density variation caused by phase changes is linear.

The equations of continuity, momentum and energy are applied for the three-dimensional packed bed TES model using the enthalpy–porosity formulation for phase transition. They can be constructed as follows using the above assumptions:

Enthalpy equation: $$H = \begin{cases} \int_{T_m}^{T} \rho_s c_s dT\,, & T < T_m\ (solid) \\ \rho_l f L, & T = T_m\ (melting) \\ \int_{T_m}^{T} \rho_l c_l dT + \rho_l L\,, & T > T_m\ (liquid) \end{cases} \tag{4-1}$$

Continuity equation: $$\frac{\partial \rho}{\partial \tau} + \nabla(\rho u) = 0 \tag{4-2}$$

Momentum equation: $$\rho \frac{\partial u}{\partial \tau} = -\nabla p + \mu \nabla^2 u + \rho g + S\,, \tag{4-3}$$

$$S = -\frac{C(1-f^2)}{f^3+\Omega} u \tag{4-4}$$

Energy equation: $$\rho \frac{\partial H}{\partial \tau} = k \nabla^2 T \tag{4-5}$$

In equations (4-3) and (4-4), the Carman–Kozeny equation is used to define the Darcy's law–type treatment of porous media. S is a damping source term that pertains to this treatment. The Carman-Kozeny equation assumes a linear relationship between the temperature and liquid fraction (f) (4-6). In the source term S, a porosity constant, C, is associated with the geometry of a mushy zone, which is 1.0×10^5 in the present study.

Liquid fraction: $$f(T) = \begin{cases} 0, & T < T_m\ (solid) \\ 0-1, & T = T_m\ (mushy) \\ 1, & T > T_m\ (liquid) \end{cases} \tag{4-6}$$

4.2.4 Mesh, Boundary and Initial Conditions

Due to the availability of a high powered computer capable of vast computational speeds sufficient to handle the amount of calculations involved in this investigation, a 3-D axisymmetric model is selected. The use of the 3-D model will fully capture the exact of the heat transfer in the system and reduce any numerical errors and deviations that might abound in a 2-D model approximation of the same system. Triangular and rectangular mesh elements were used for precision, and mesh sizes ranged from 1 to 0.01 mm with orthogonal quality.

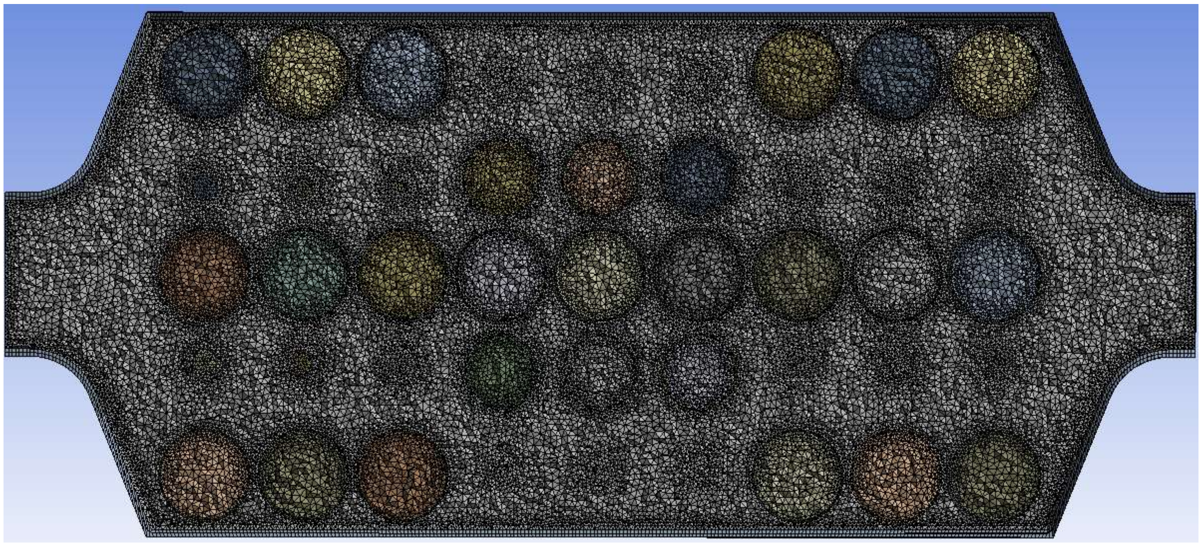

Figure 4-12: 3-D Mesh grids used for simulation (Spherical encapsulation)

The following are assumptions necessary for the boundary conditions to be applicable:

- The HTF maintains a consistent temperature and velocity.
- The line of symmetry is regarded to be the tank's center.
- Thermal exchange between the tank exterior and the ambient is negligible due to thermal insulation.
- The packed bed generates no internal heat.
- Thermal radiation is negligible.
- PCMs undergo phase change in three stages: solid → phase transition → liquid.

The initial and boundary conditions employed to solve the governing equation are as follows,

Initial conditions:

a) Initial temperature, $T_{PCM} = 30°C$ at $\tau = 0$ (charging cycle)
b) PCM conditions are the end of the charging cycle are considered as the PCM initial conditions for the discharge cycle.

Boundary conditions:

c) Inlet: at $z = 0$, $T_{HTF} = 400°C$ at $\tau < \tau_c$, $T_{HTF} = 200°C$ at $\tau_c < \tau \leq \tau_d$ and $v_{HTF} = 0.1$ m/s.
d) Outlet: $\left.\frac{dP}{dz}\right|_{z=H} = 0, \left.\frac{dT_{HTF}}{dz}\right|_{z=H} = 0, \left.\frac{dT_{HTF}}{dz}\right|_{z=H} = 0$
e) Packed bed walls: $u = v = 0$
f) Axisymmetric: $\left.\frac{dT_{HTF}}{dr}\right|_{r=0} = 0, \left.\frac{dT_{PCM}}{dr}\right|_{r=0} = 0, \frac{du}{dr} = 0, \frac{dv}{dr} = 0$
g) Insulated tank walls: $\left.\frac{\partial T_{HTF}}{\partial r}\right|_{r={}^{D}/_{2}} = 0, \left.\frac{\partial T_{PCM}}{\partial r}\right|_{r={}^{D}/_{2}} = 0$
h) no slip boundary conditions were assumed on the internal and external surface of capsules

4.2.5 Simulation Solution Procedure

ANSYS Fluent 2021 R2 is the commercial software employed to perform the 3-D packed bed TES model heat transfer simulations by solving the governing equations using the boundary and initial conditions. The control volume technique is used to model the fluid flow. The governing equations are calculated using a pressure-based solver. The SIMPLE algorithm with a second order pressure correction and a Rhie-Chow distance-based flux type achieves the pressure–velocity coupling. For the purpose of discretizing the temporal terms, the second-order implicit scheme is utilized. A second-order upwind technique is utilized for advective term discretization contained within the momentum equation. For the purpose of discretizing energy equations, the second order upwind approach is utilized. The thermal conductivity, specific heat capacity and density, are taken as constant before and after phase transition and vary linearly during phase transition. In order to achieve stable convergence, relaxation factors of 0.3, 0.5, and 0.9 are applied to the pressure, momentum, and liquid volume fraction, respectively. If the residuals are lower than the convergence criterion of 10^{-3}, 10^{-6}, and 10^{-9}, which are determined for continuity, momentum, and energy equations, respectively, the solutions are considered converged. Navier-Stokes equations were solved using the realizable k-epsilon turbulence model with scalable wall treatment alongside solidification and melting model [92].

4.2.5 Mesh Independency Check

The thermal energy storage tank that was filled with PCMs that were enclosed in spheres underwent a mesh independence test. The mesh is varied and has sensitive areas and was auto-generated by the commercial software package to provide the most suitable mesh for the complex geometry of multiple components. Four grid sizes were considered given in Table 4-10. PCM temperature simulations for the charging phase of the spherical capsule were conducted using the various grid sizes. The results of the simulations revealed that the extra fine and fine mesh scenarios produced comparable outcomes while requiring less calculation time. Except for the additional computational work, extremely fine would have been preferable. As a result, the extra fine mesh was selected for the heat transfer analysis of the TES unit .

Table 4-10: Mesh grid parameters

GRID	**Extremely Fine**	**Extra Fine**	**Fine**	**Moderately Fine**
NODES	4,121,260.00	3,084,905.00	1,969,696.00	1,610,466.00
ELEMENTS	23,362,328.00	17,684,389.00	11,249,720.00	9,368,362.00
ELEMENT SIZE	0.9	1	1.2	1.4

4.2.6 CFD Model Validation

Differences between predicted numerical results and past experimental findings were measured to ensure a proper assessment of the use of the enthalpy–porosity formulation on ANSYS Fluent. Experimental data from Raul et all [1] were used to validate the current model. To conduct their research, they used a packed bed LHS encapsulated PCMs setup. The experimental apparatus comprises a cylinder-type packed bed , a canned motor pump for circulating the HTF, a reservoir tank for the HTF, a heat exchanger, twenty-two 500 W electric heaters, and a three-way valve. The parameters of the PCM, HTF and packed bed and capsule dimensions are given in the table below.

Table 4-11: Experimental Setup Parameters

PARAMETERS	VALUE
PCM	A164 (T_m = 168.7°C)
Bed inner diameter	170mm
Bed height	360mm
Bed wall thickness	3.4mm
Capsule diameter	29mm
Capsule wall thickness	1mm
Porosity	0.6
HTF	Hytherm 600
HTF Inlet Temperature	191°C
Inlet and Outlet Diameter	20.87mm
Capsule and Bed Material	SS316

Six T-type thermocouples are inserted into the capsules in different axial and radial (90mm gaps along the direction of fluid flow) directions of LHTES to analyze PCM temperature changes.

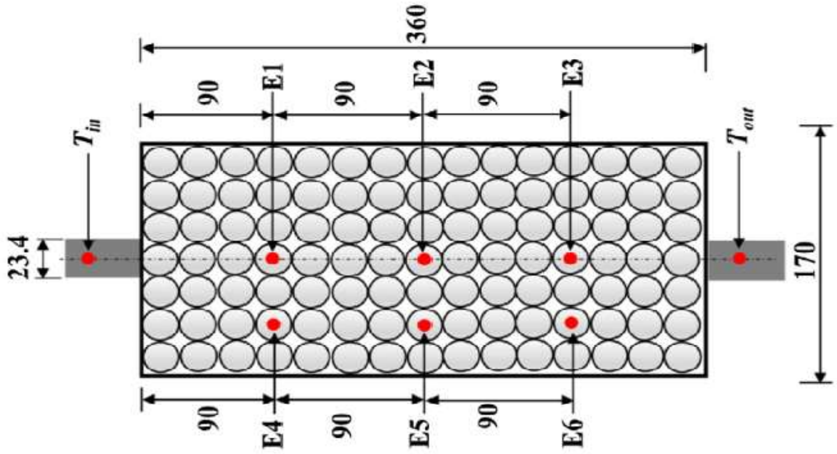

Figure 4-13: Cross-section of Experimental setup indicating the positions of the thermocouples and bed dimensions [1]

Figure 4-14 contrasts the experimental and simulated temperature distribution of capsules at H = 270mm, which corresponds to the distance from the start of the bed length to the thermocouples E3 and E6 as shown in Figure 4-13, during the charging and discharging cycles.

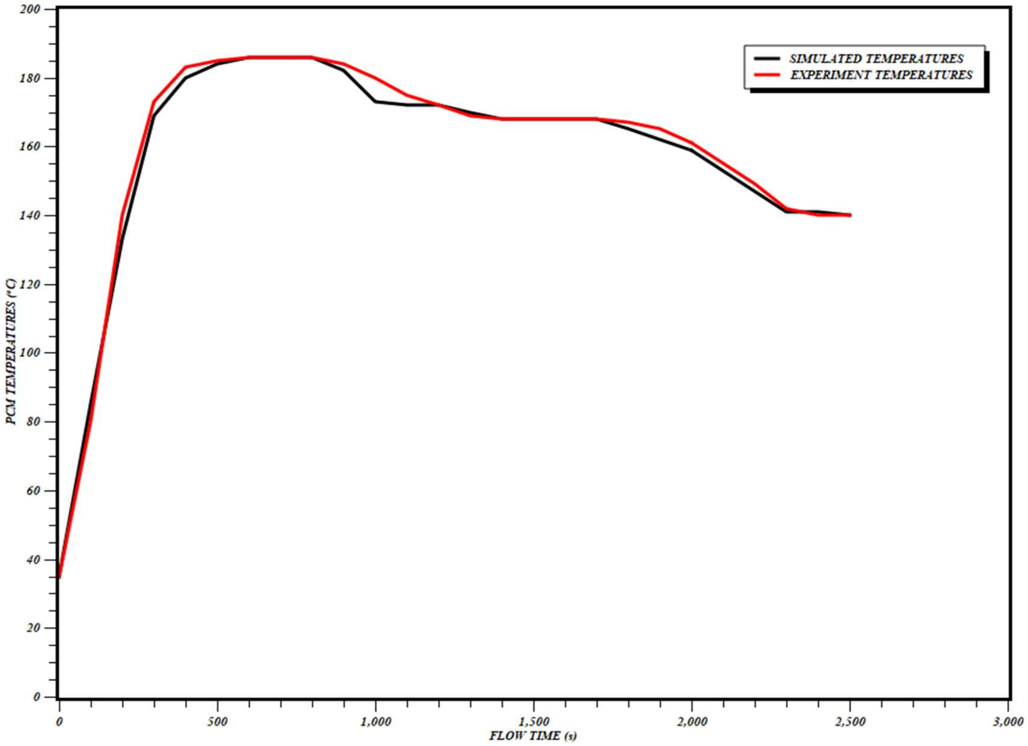

Figure 4-14: Simulated and experimental temperature distribution of capsules at H = 270 mm

As can be observed, the trends of both curves are highly comparable, with the greatest relative difference being only approximately 3%. In the experimental setup, the entrance and exit portions of the tank are not entirely insulated, resulting in some heat loss and differences between the empirical and simulated heat transfer coefficients. Despite these disparities, the proposed model's numerical results look comparable with previously acquired experimental data, allowing for more exact predictions.

CHAPTER FIVE

5. Results, Comparative Data Analysis and Discussions

5.1 Introduction

5.1.1 Results Overview

Various types of PCMs can be employed to improve heat transfer between the HTF and the capsules. The rate of heat transfer or, more broadly, the performance of LHTES during charging and discharging processes is primarily determined by the temperature differential between the HTF and phase change temperatures of the capsules, as well as the total surface area of the PCM encapsulation.

Using ANSYS Fluent CFD package, simulation runs were performed to study the performance of a 3 stage cascaded thermal energy storage with different encapsulation geometries. The rate of melting and solidification of the PCM during both the energy charging and discharging modes were investigated for each PCM encapsulation geometry. There are nine (9) different PCM encapsulations and 2 different PCM layouts arrangements listed in Table 4-3 were studied. The PCMs are arranged in decreasing order of their melting point within each encapsulation layer.

Case 1 is the base case with which the other cases were compared. It consists of 171 spheres of 12.5mm radius and with a total surface area of 1963.50mm^2. The total surface area increases with each new geometric configuration while the volume of each new encapsulation remains constant. Case 2 is a cylinder capped with two hemispheres of radius 10mm and height 17.21mm. The case has a 4.67% area increase per capsule. Case 3 is an ellipsoid whose semi-major, rotational axes are 19.53mm, 10mm and 10mm respectively and it has a 7.12% area increase from the base encapsulation. Case 4 is a frustum capped with hemispheres at the mid-point of the slant height of cone. This case increases the total surface area by 22.83%. Case 5 is complex encapsulation comprising of hemispheres, frustrum and an arc of revolution. This geometric configuration increases the area 24.26% from the base case. Case 6 is an approximate ovaloid whose surface area increases by 26.30% from the base case. Case 7 is comprises of two cones whose base radii and connect by an arc of revolution. This increases the area by 27.39 as compared to the base. Case

8 is a torus with an ellipse as the geometry of revolution. It improves the base case area by 41.12% while maintaining the same volume. Case 9 is similar to Case 8. It is a torus with a parallelogram (Bi-Triangle) as the geometry of revolution and it differs from the base case area by 110.59% for the same volume of the base case. Simulations of each case were run considering 2 different packing layouts described above in 4.2.1.

The results from the CFD simulations are presented in the form of PCM temperature distributions, PCM specific thermal energy, transient liquid fraction and temperature contours of the cross-section of the encapsulation. One PCM encapsulation was selected for each of the 3 PCM layers to serve as indicators (P1, P2, P3) for the physical properties and behaviors been investigated. The relative positions of these three indicators are given in the figure below (Case 1);

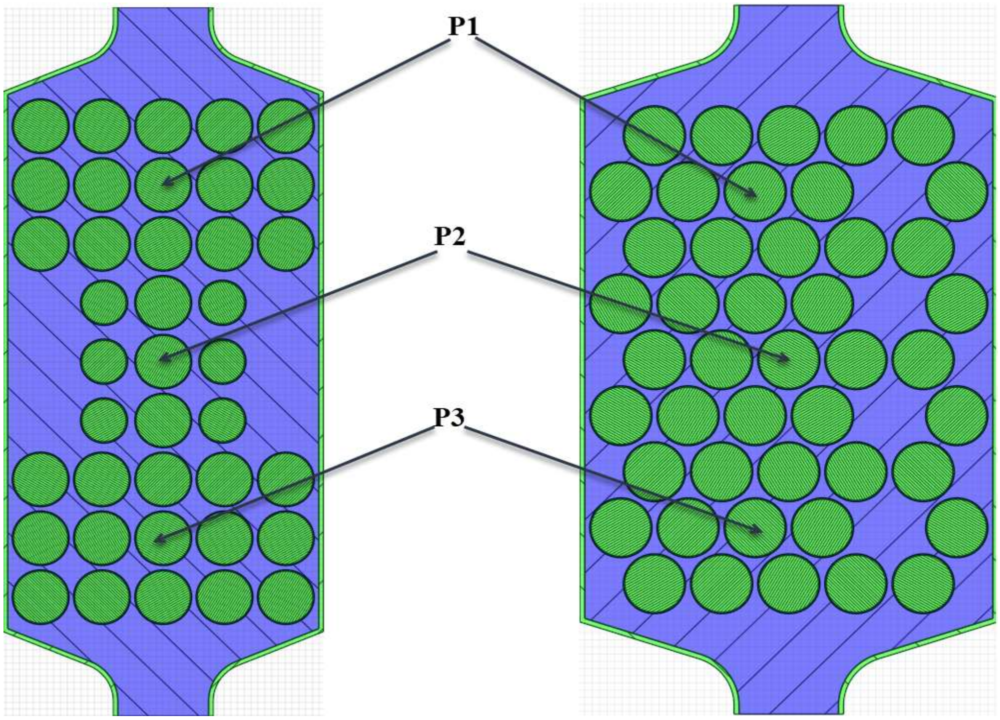

Figure 5-1: Relative positions of property indicators (P1, P2, P3)

Table 4-8 shows the thermophysical properties that were employed to perform transient numerical simulations of TES unit during charging and discharging cycles at constant HTF flow rate of 0.1m/s. In all the cases during the charging cycle, the simulation begins with the PCM in full-solid state at room temperature (T_{PCM} = 30°C). The HTF (60% wt $NaNO_3$ + 40% wt KNO_3) is circulated at a constant temperature (T = 400°C) which is above the fusion temperatures of the cascaded PCMs (T_{KOH} = 378°C, T_{KNO3} = 333°C, T_{NaNO2}=227.32°C). Thus, the PCM initiates melting with the flow of the heat transfer fluid form the inlet and a melted layer adjacent to the encapsulation wall gradually advances towards the whole PCM. The charging process is completed when the PCMs are in thermal equilibrium with the heat transfer fluid and all three temperature indicators have attain the same temperature value of the HTF (400°C for charging and 200°C for discharging). The discharging cycle (PCM solidification) starts immediately after reaching complete thermal equilibrium. In this cycle, the temperature of the HTF from the inlet is reduced by a factor of 0.5 of the charging cycle HTF temperature (T_{HTF} = 200°C) to initiate the solidification of the PCMs by conducting heat to the now 'cold' HTF. With increasing flow time, the solidification gradually advances to cover the whole PCM. The increased area with each new case significantly motivates faster charging and discharging rates.

5.2 Result Plots

5.2.1 PCM Temperature Distributions

The temperature distributions of the encapsulated PCM at the three thermophysical properties indicators (P1, P2, P3) in the LHTES unit for the nine PCM encapsulation geometries being numerically investigated are shown in Figure 5-2, Figure 5-3, Figure 5-4, Figure 5-5, Figure 5-6, and Figure 5-7 at constant inlet HTF temperatures and flow rate during the charging and discharging cycles for the two packed bed layouts.

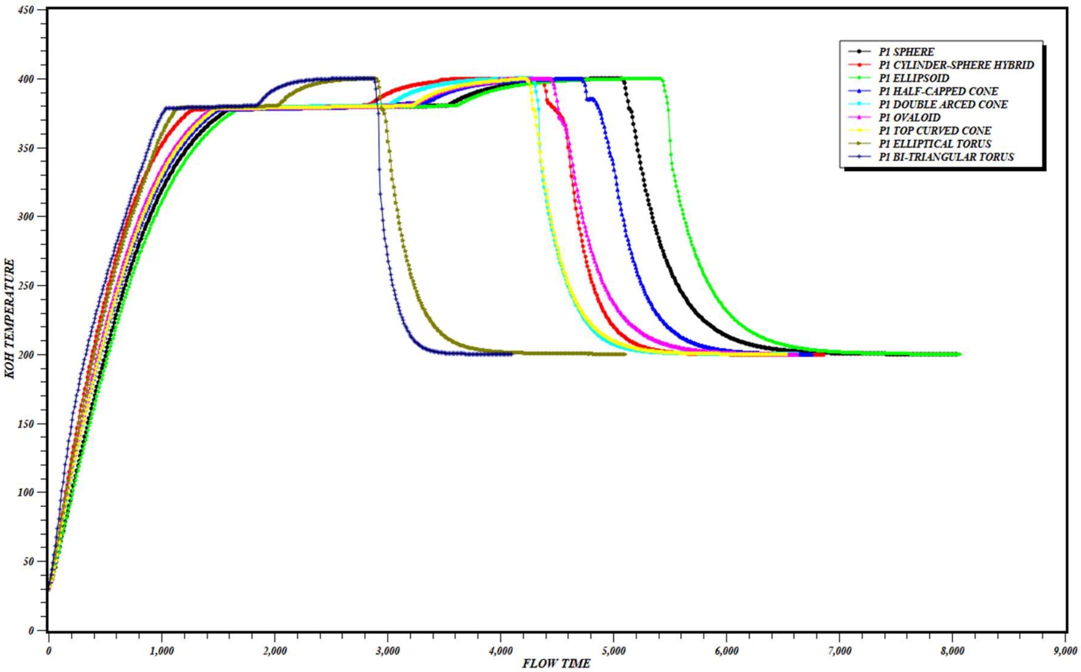

Figure 5-2: : PCM Temperature Distributions at P1 for Layout 1

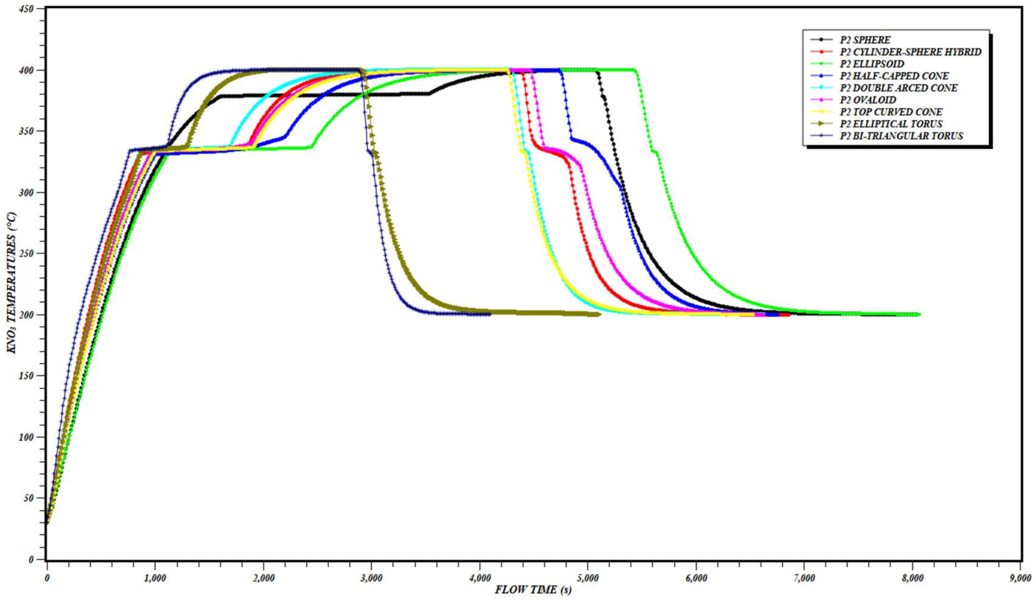

Figure 5-3: PCM Temperature Distributions at P2 for Layout 1

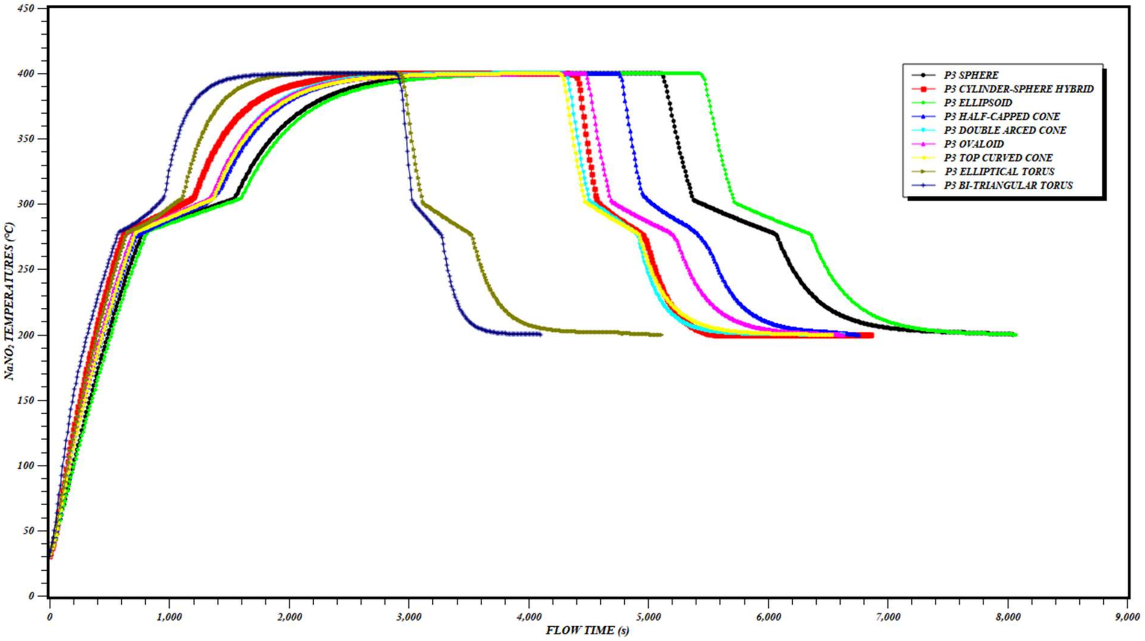

Figure 5-4: PCM Temperature Distributions at P3 for Layout1

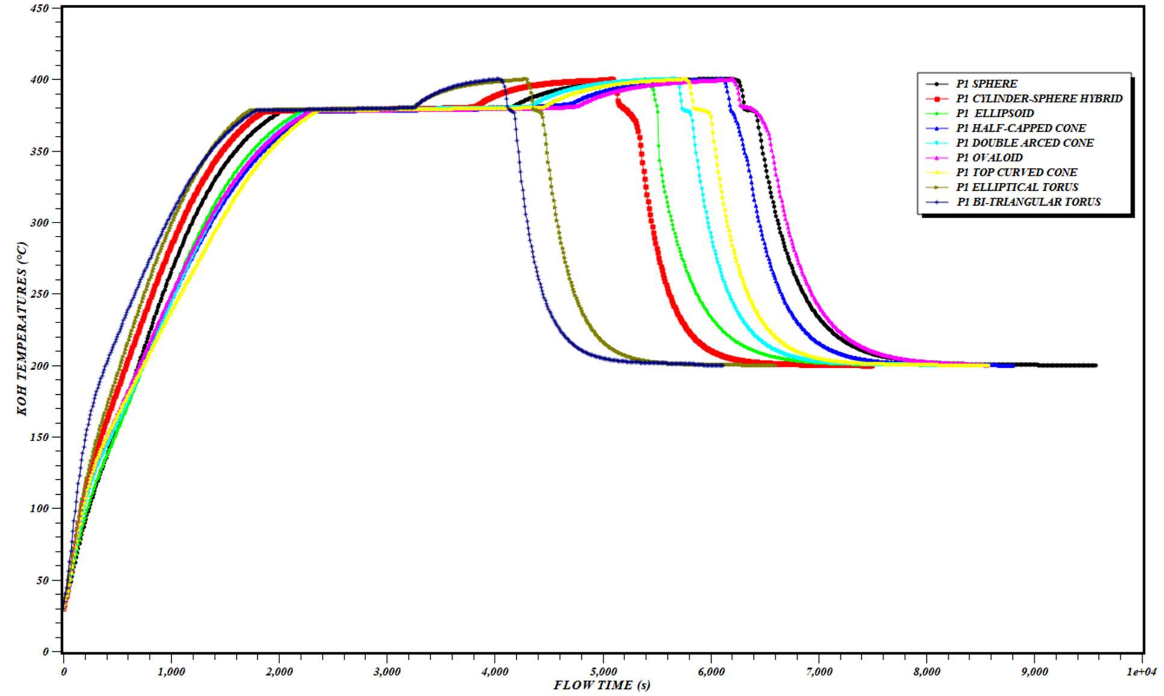

Figure 5-5: PCM Temperature Distributions at P1 for Layout 2

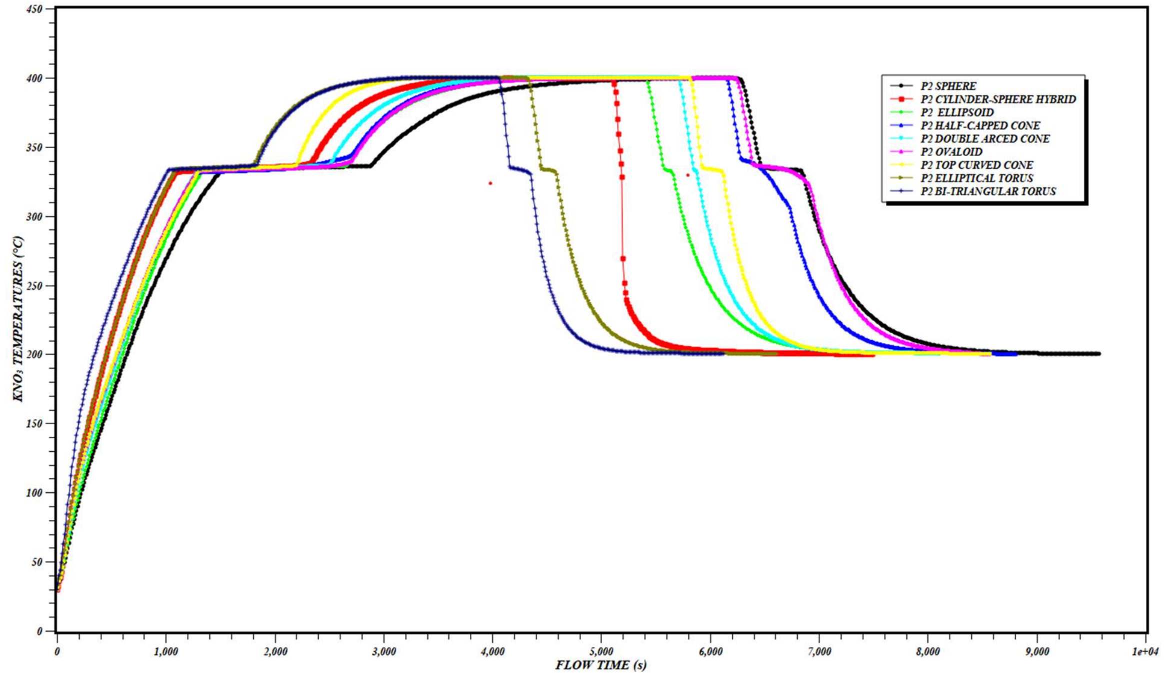

Figure 5-6: PCM Temperature Distributions at P2 for Layout 2

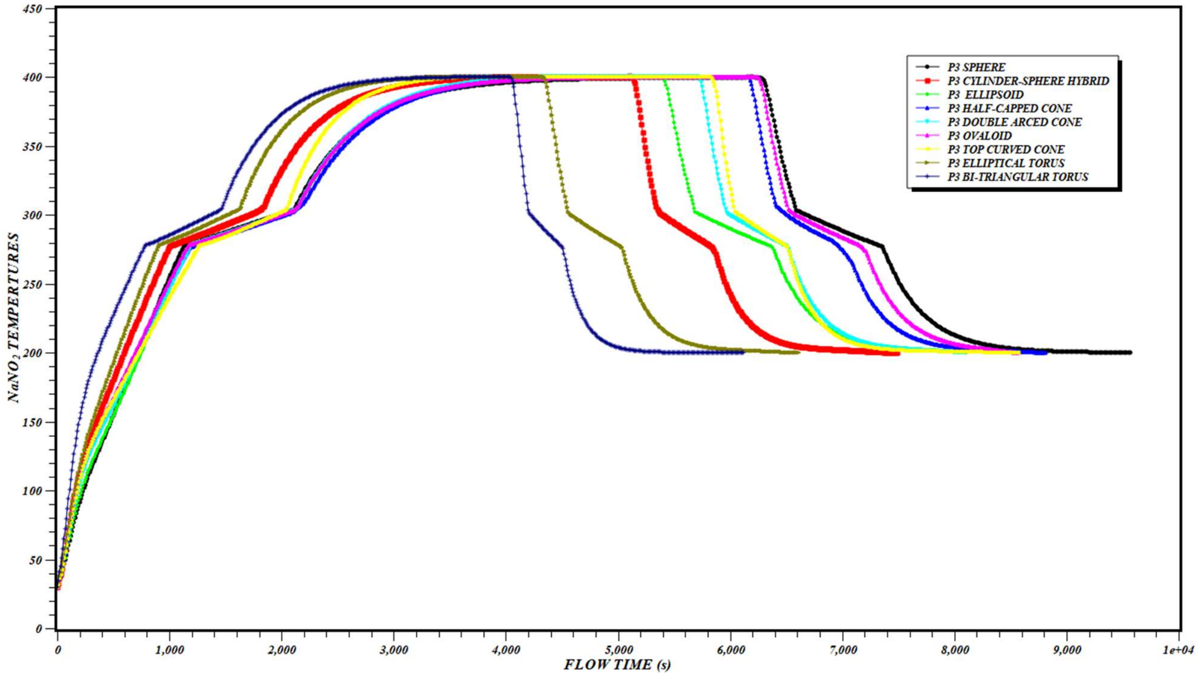

Figure 5-7: PCM Temperature Distributions at P3 for Layout 2

From the graphical illustrations presented in Figure 5-2, Figure 5-3 and Figure 5-4, the charging cycle begins at t = 0. The PCM temperatures as measured at P1, P2, P3 begins to increase fairly linearly as the HTF flows through the inlet through the packed bed and exits the tank at the outlet. The temperature increase continues till the phase change threshold is reached. The time required to reached this threshold varies with each capsule design. Case 9 having the shortest time and Case 2 the longest time relatively. During phase change, the PCM temperatures drift from the solidus to liquidus temperature, the signifies total phase transformation. As a result of the HTF flowing at a constant 400°C, the PCMs temperatures exceed their individual phase temperatures. The PCM temperatures steadily increase till they attain thermal equilibrium with the HTF. The discharge cycle features an exponential temperature decrease till P1, P2 and P3 are in thermal equilibrium with the inlet discharge temperature of 200°C. At P1 and P2, the time required for PCM phase change during discharge is relatively shorter in comparison to the charging cycle. At P3 however, the phase change time during discharge is nearly equivalent to that of charging phase. This can be attributed to the rise in HTF temperature along the packed bed as the fluid flow through different PCM layers .It is also evident that the charging and discharging times decreases with each new capsule geometry. This is due to the increased surface area of each capsule, the presence of a central hollow (Case 8 and Case 9) and relatively high SVR. Case 9 performs best in terms of shorter charging and discharging times whilst Case 3 has the longest cycle time for this layout. Figure 5-5, Figure 5-6, and Figure 5-7 present very similar patterns as Figure 5-2, Figure 5-3 and Figure 5-4. They differ mostly in terms of the cycle flow time in which the former has the longer cycle completion time.

5.2.2 PCM Specific Thermal Energy Profiles

The effect of the PCM capsule design on the specific energy distributions are illustrated in the results from the numerical simulations of the LHTES in the charging and discharging cycles for the five PCM cases being investigated at the three indicators.

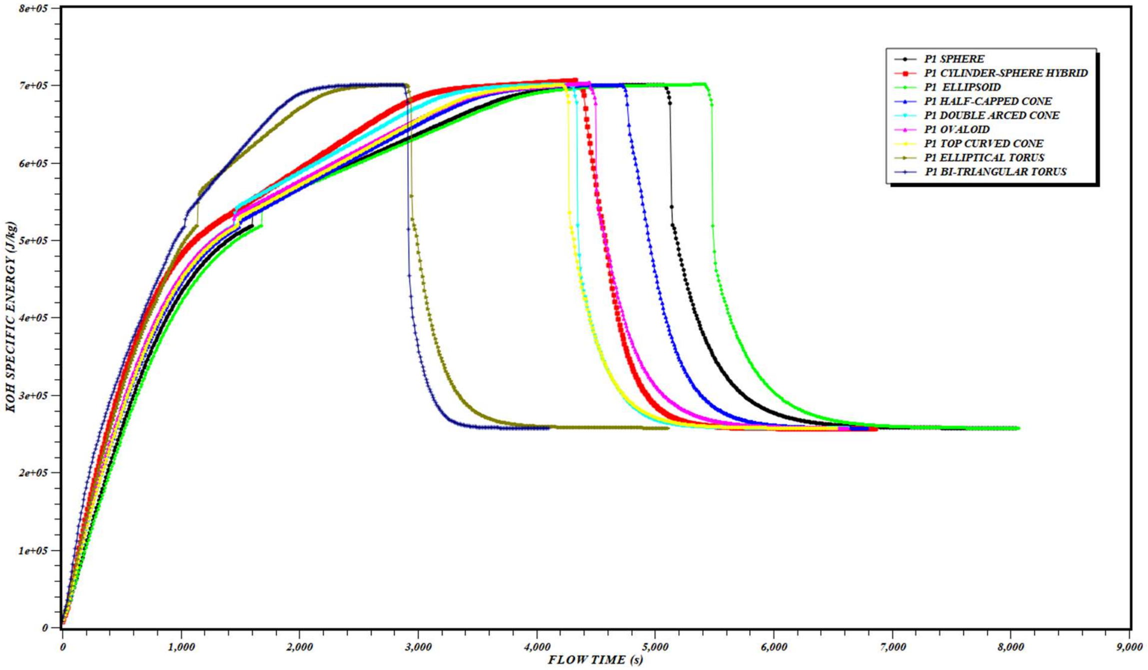

Figure 5-8: : PCM Specific Energy Distributions at P1 for Layout 1

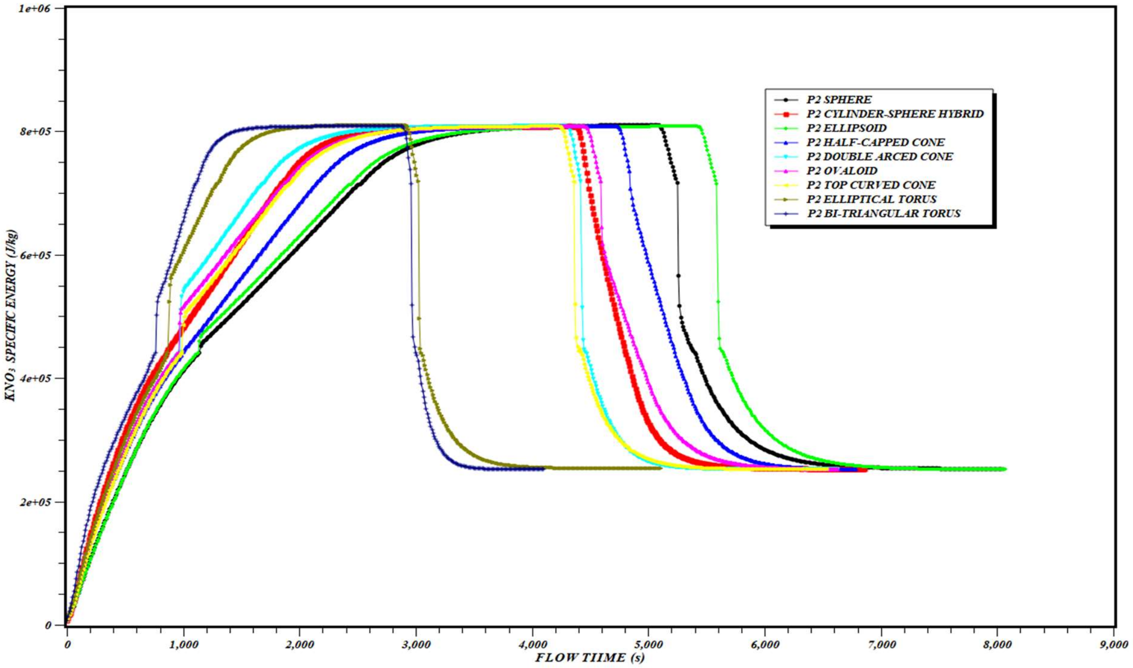

Figure 5-9: PCM Specific Energy Distributions at P2 for Layout 1

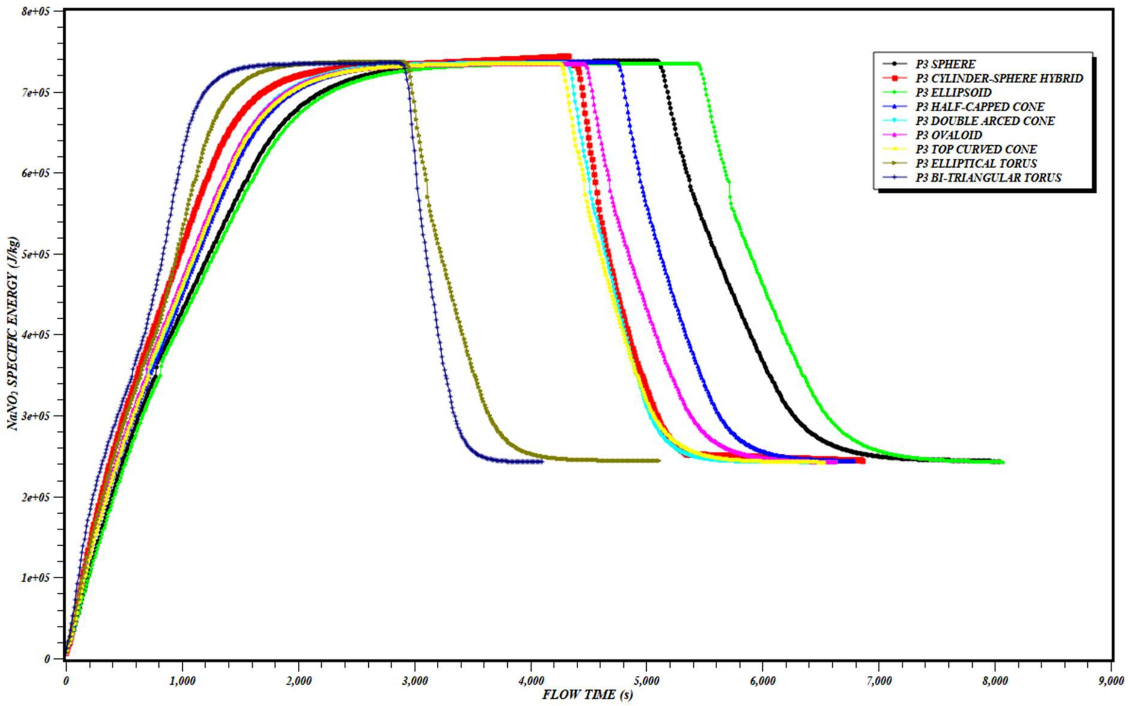

Figure 5-10: PCM Specific Energy Distributions at P3 for Layout 1

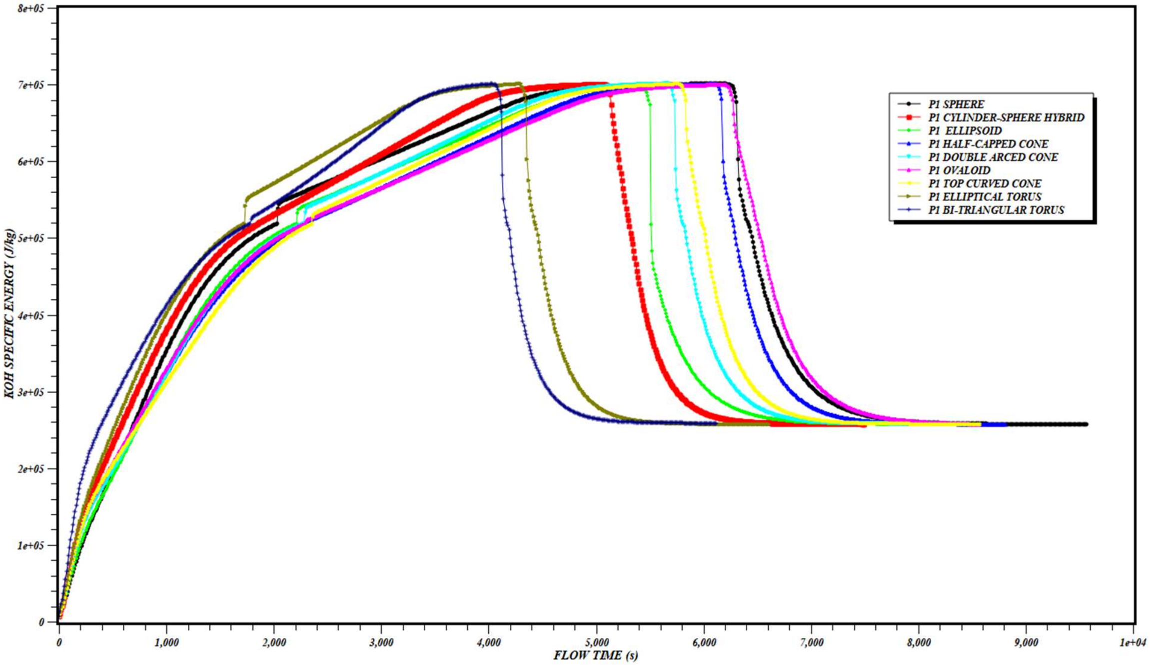

Figure 5-11: PCM Specific Energy Distributions at P2 for Layout 2

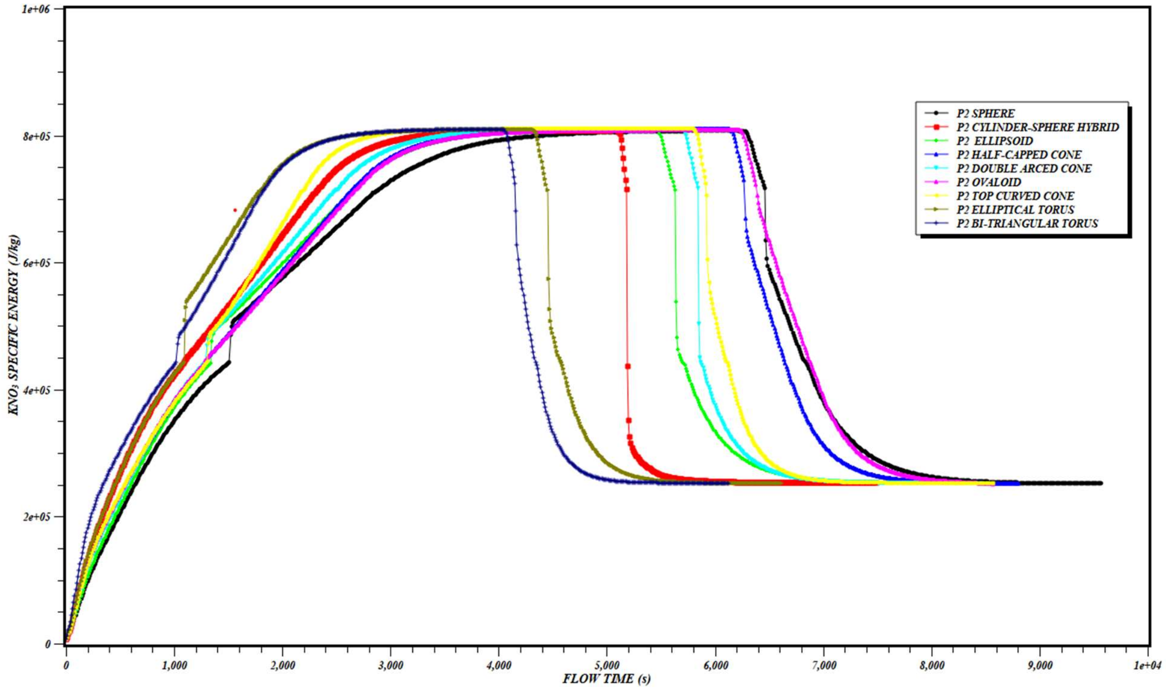

Figure 5-12: PCM Specific Energy Distributions at P2 for Layout 2

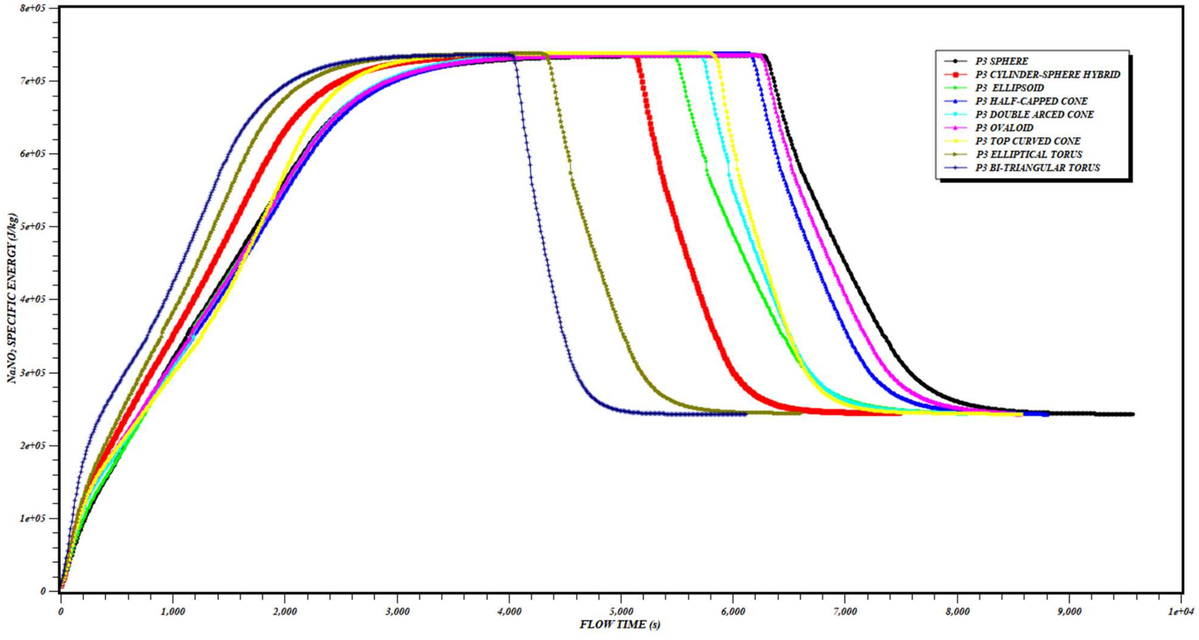

Figure 5-13: PCM Specific Energy Distributions at P3 for Layout 2

5.2.3 PCM Transient Liquid Fraction Contours

The transient liquid fraction contours from the CFD simulations of the LHTES during charging and discharging for the nine PCM cases and two layouts at the three indicators are given below;

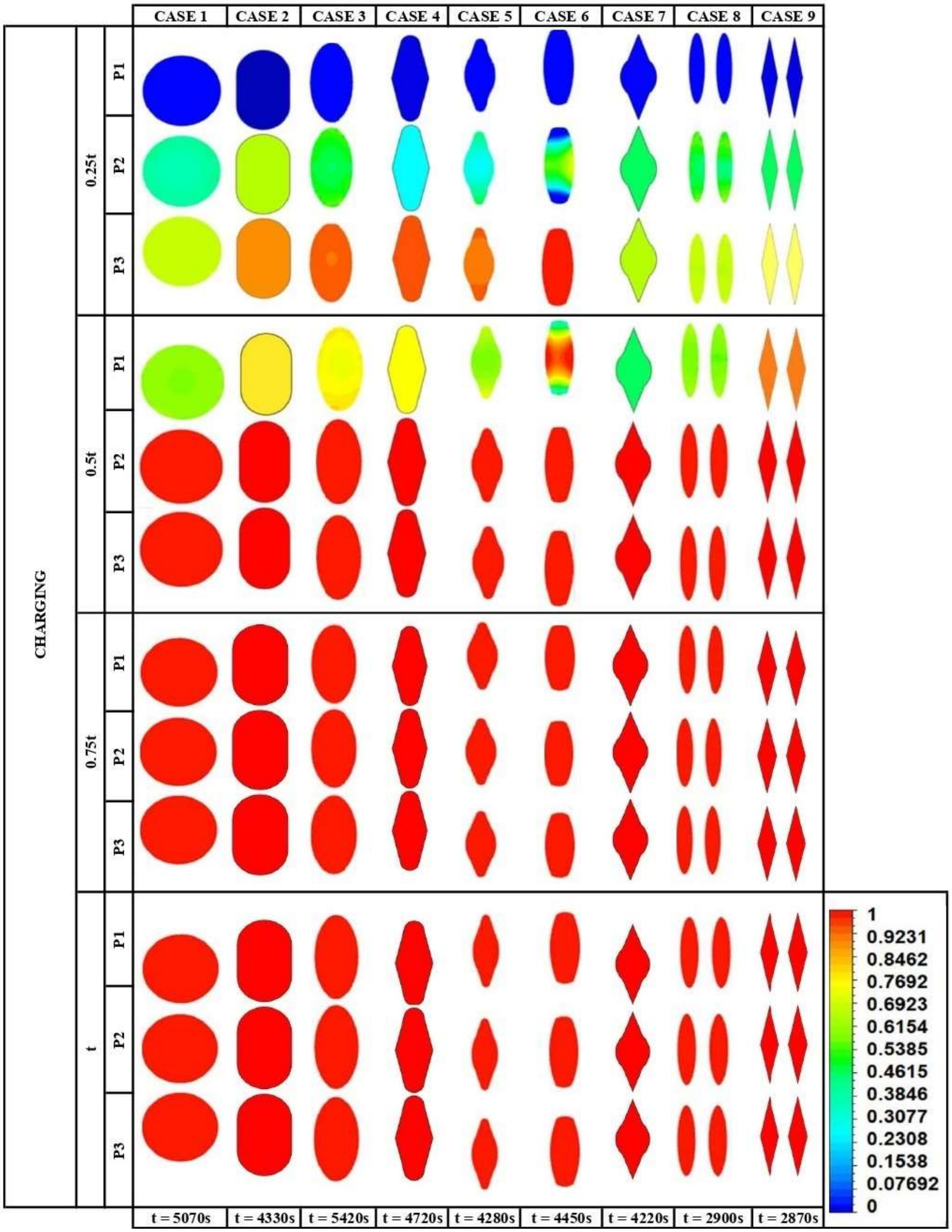

Figure 5-14:Transient Liquid Fraction Contours for Charging Cycle Cases 1-9 (Layout 1)

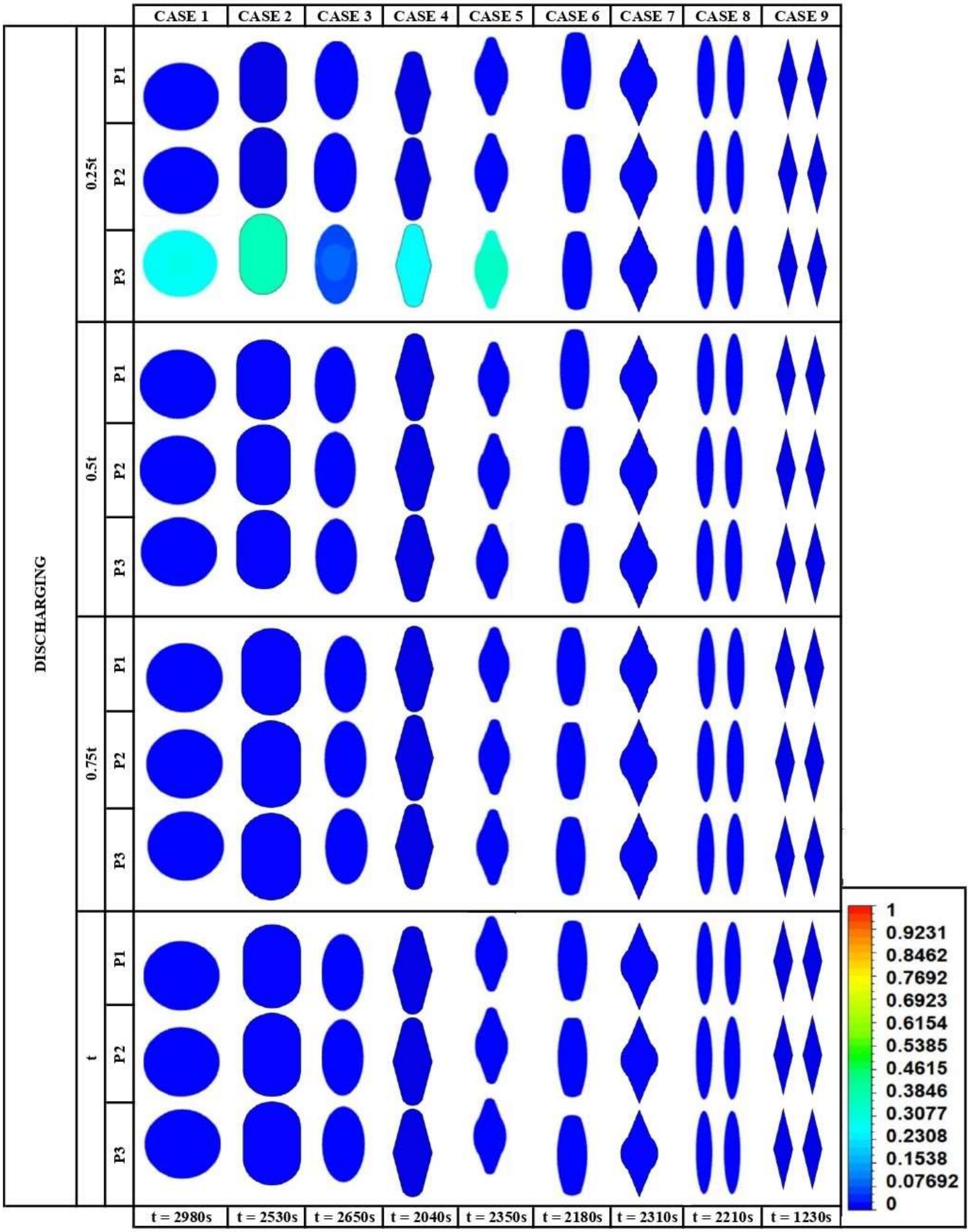

Figure 5-15: Transient Liquid Fraction Contours for Discharging Cycle Cases 1-9 (Layout 1)

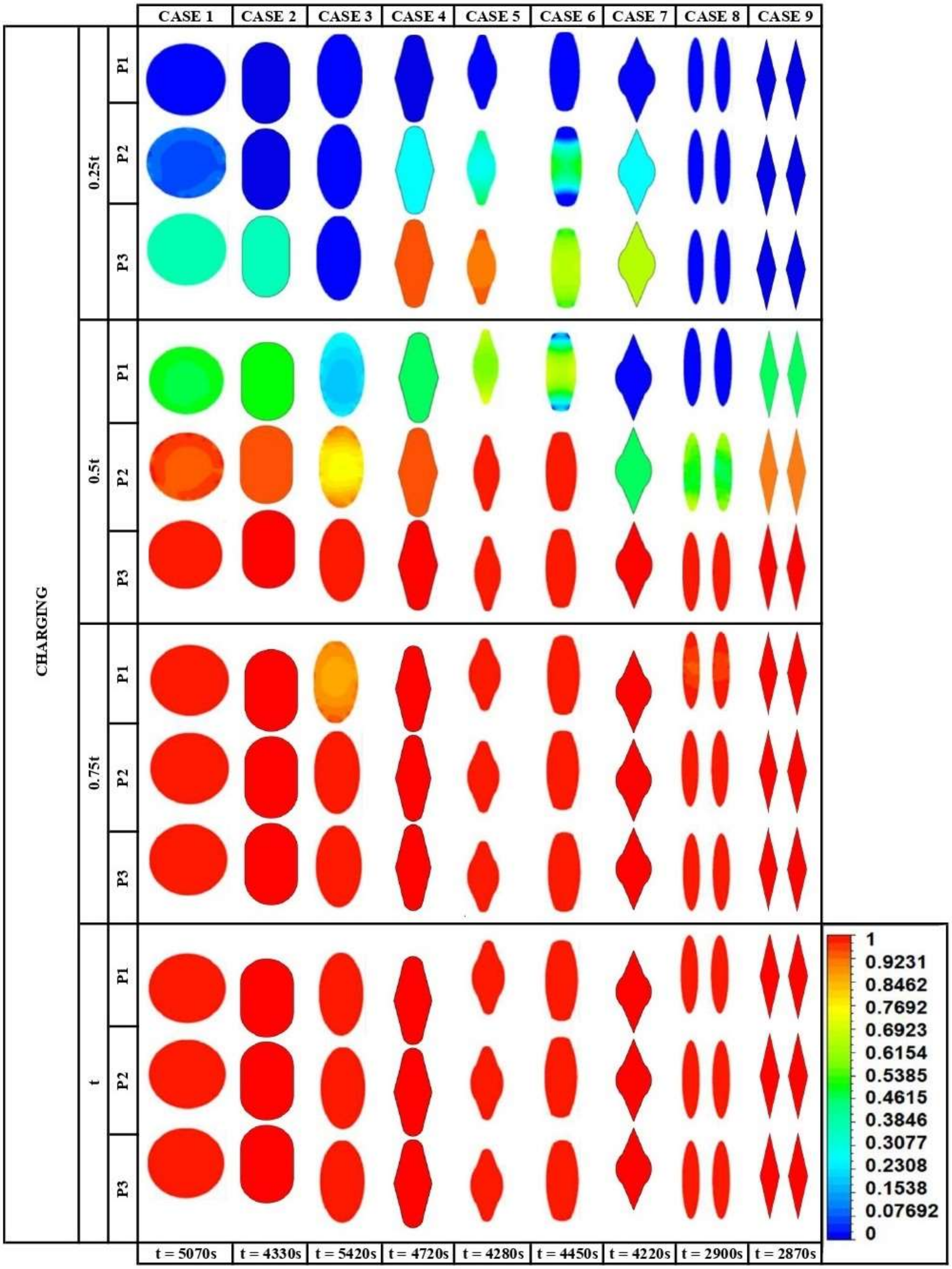

Figure 5-16: Transient Liquid Fraction Contours for Charging Cycle Cases 1-9 (Layout 2)

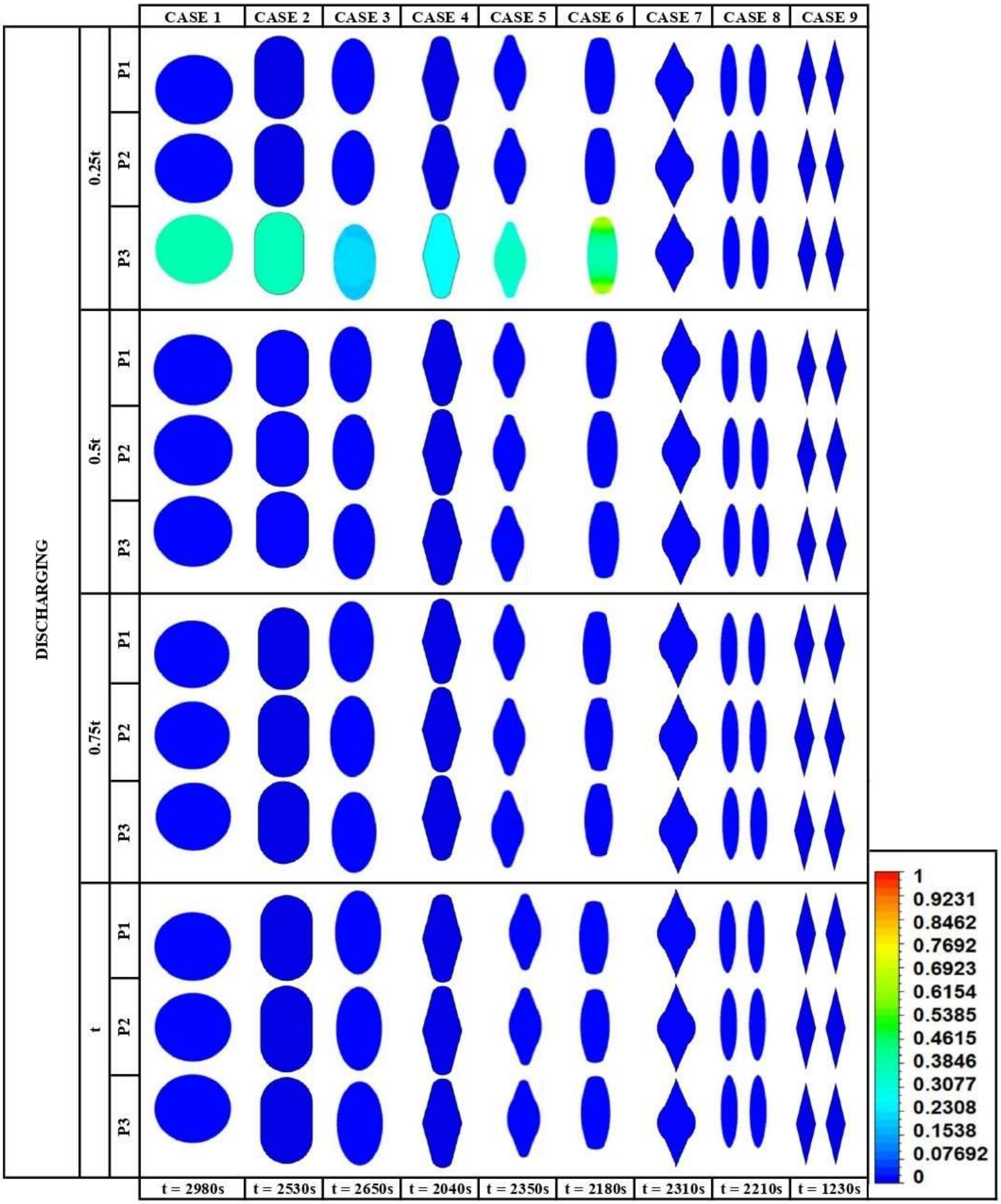

Figure 5-17: Transient Liquid Fraction Contours for Discharging Cycle Cases 1-9 (Layout 2)

Figure 5-14, Figure 5-15, Figure 5-16, and Figure 5-17 depict the quarterly transient liquid fraction distributions inside the different capsule designs during charging and discharging of the packed bed TES. Figure 5-14 and Figure 5-15 represent the first packed bed layout, Figure 5-16 and Figure 5-17 represent the second layout. The contours displayed are for each PCM indicator at the following time markers 0.25t, 0.5t, 0.75t and t (t = charging/discharging completion times for each capsule geometry).

Considering the first layout (Layout 1), at 0.25t (charging), the P1 contours all present similarities during the charging phase as a result of the melting point of KOH not attained at that time. Deviations in liquid fraction formation are realized in P2 and P3 for all cases, the PCMs melt from that the capsule walls inwardly to the center of the capsule however the liquid phase formation is not uniform. At 0.5t (charging), P2 and P3 are fully developed liquids and are undergoing sensible heat gain. The PCMs at P1 are undergoing phase change hence their differential contours. From 0.75t to t (Charging), all the PCMs have fully undergone phase change and are all liquids. The discharge liquid fraction contours are very much identical after 0.25t. This is the result of short discharge completion times and the bulk of the phase change process occurring before the 0.5t mark. Cases 6, 7, 8 and 9 are already solids by the 0.25t mark because they have shorter discharge time in comparison to the other cases.

The contours in the second layout (Layout 2) bears similarities to the those of layout 1 with a few key differences. At 0.5t (charging), the P2 are not all fully developed liquids save for Case 5 and Case 6. At 0.75t (charging), P1, P2 and P3 are fully developed liquids and are undergoing sensible heat gain save for P1 of Case 3. At t (Charging), all the PCMs have fully undergone phase change and are all liquids. The discharge liquid fraction contours are very much identical after 0.25t. This is the result of short discharge completion times and the bulk of the phase change process occurring before the 0.5t mark. Cases 7, 8 and 9 are already solids by the 0.25t mark because they have shorter discharge time in comparison to the other cases.

5.2.4 PCM Transient Temperature Contours

The transient temperature contours from the CFD simulations of the LHTES during charging and discharging for the nine PCM cases and two layouts at the three indicators are given below;

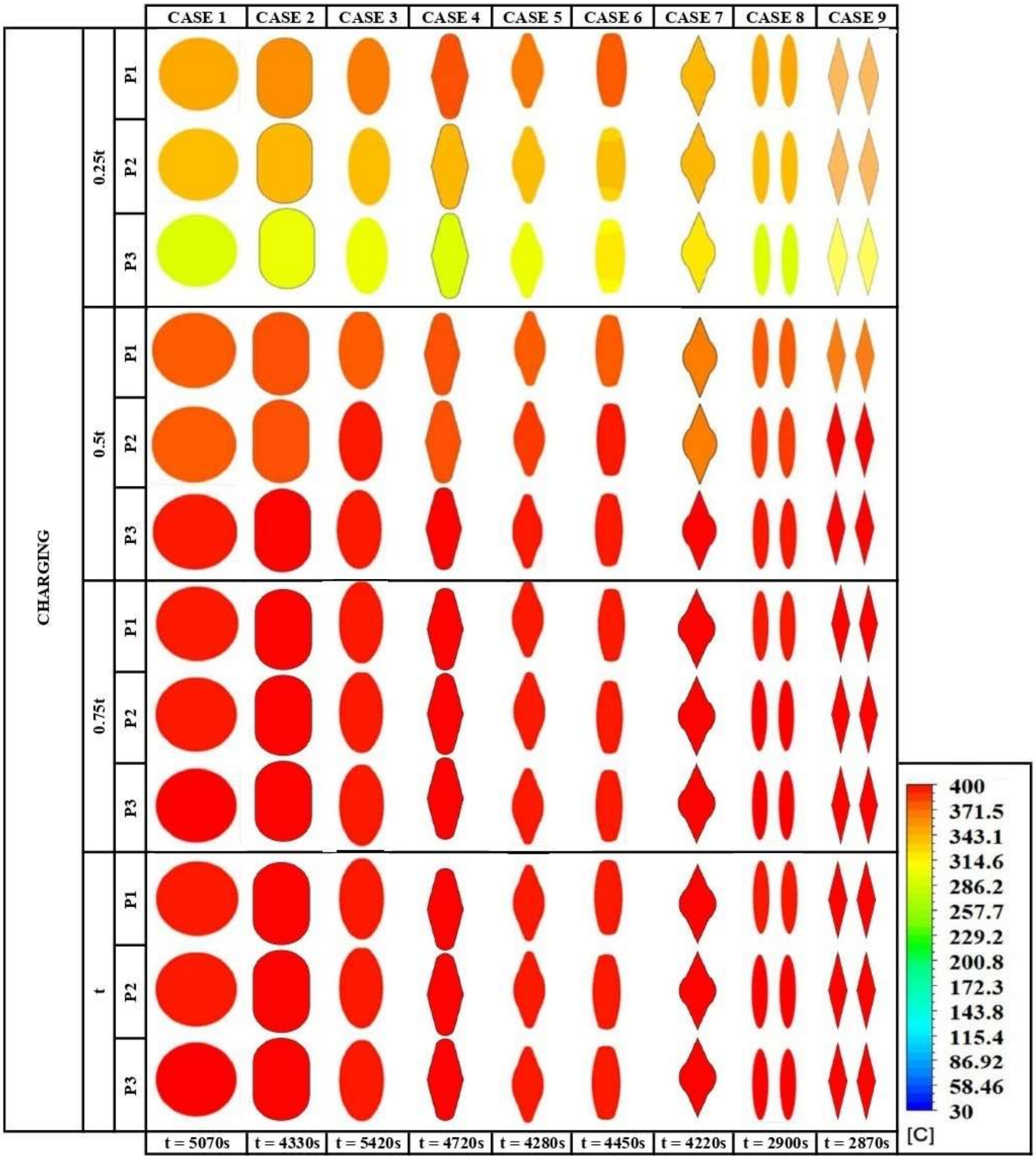

Figure 5-18: Transient Temperature Contours for Charging Cycle Cases 1-9 (Layout 1)

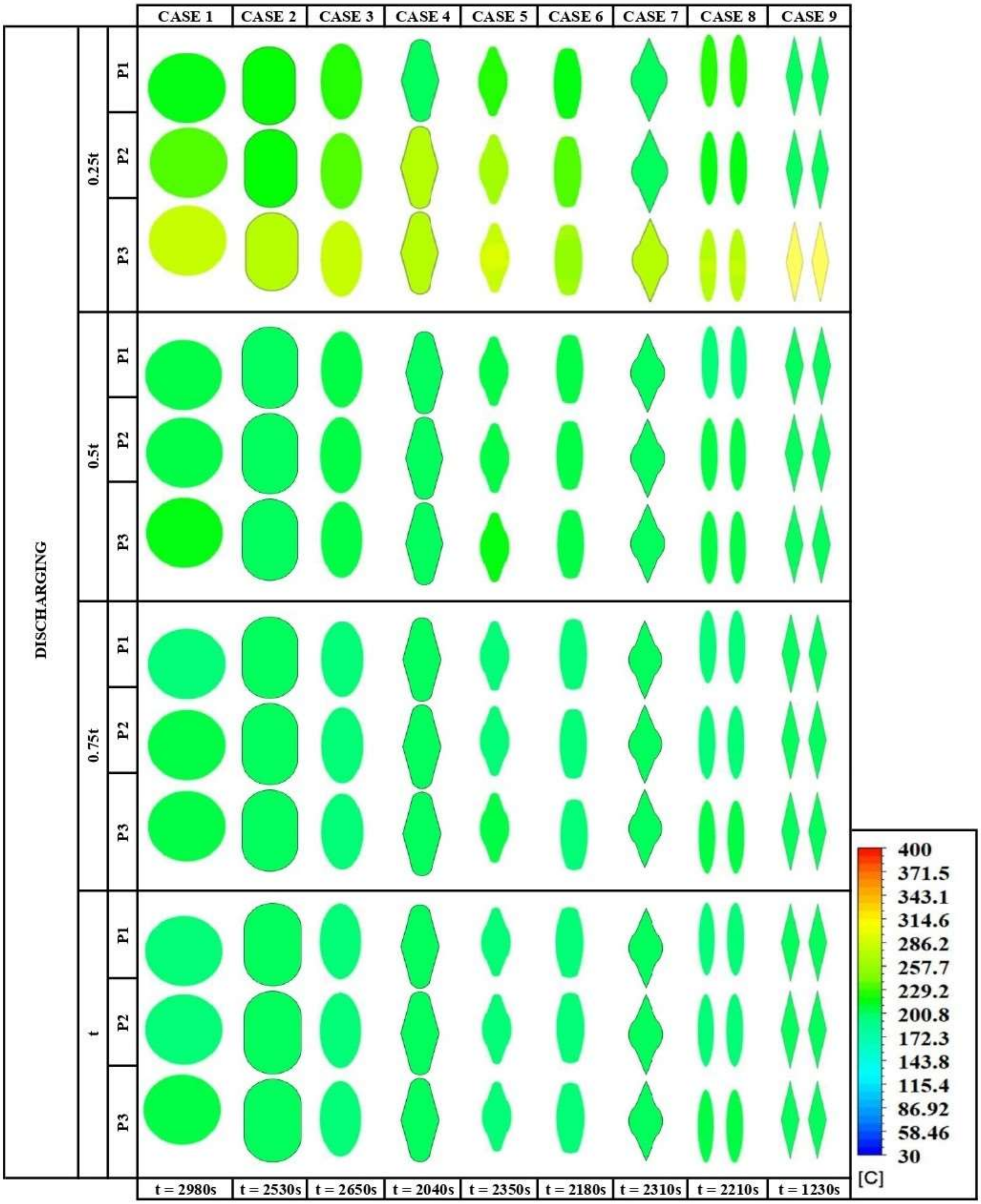

Figure 5-19: Transient Temperature Contours for Discharging Cycle Cases 1-9 (Layout 1)

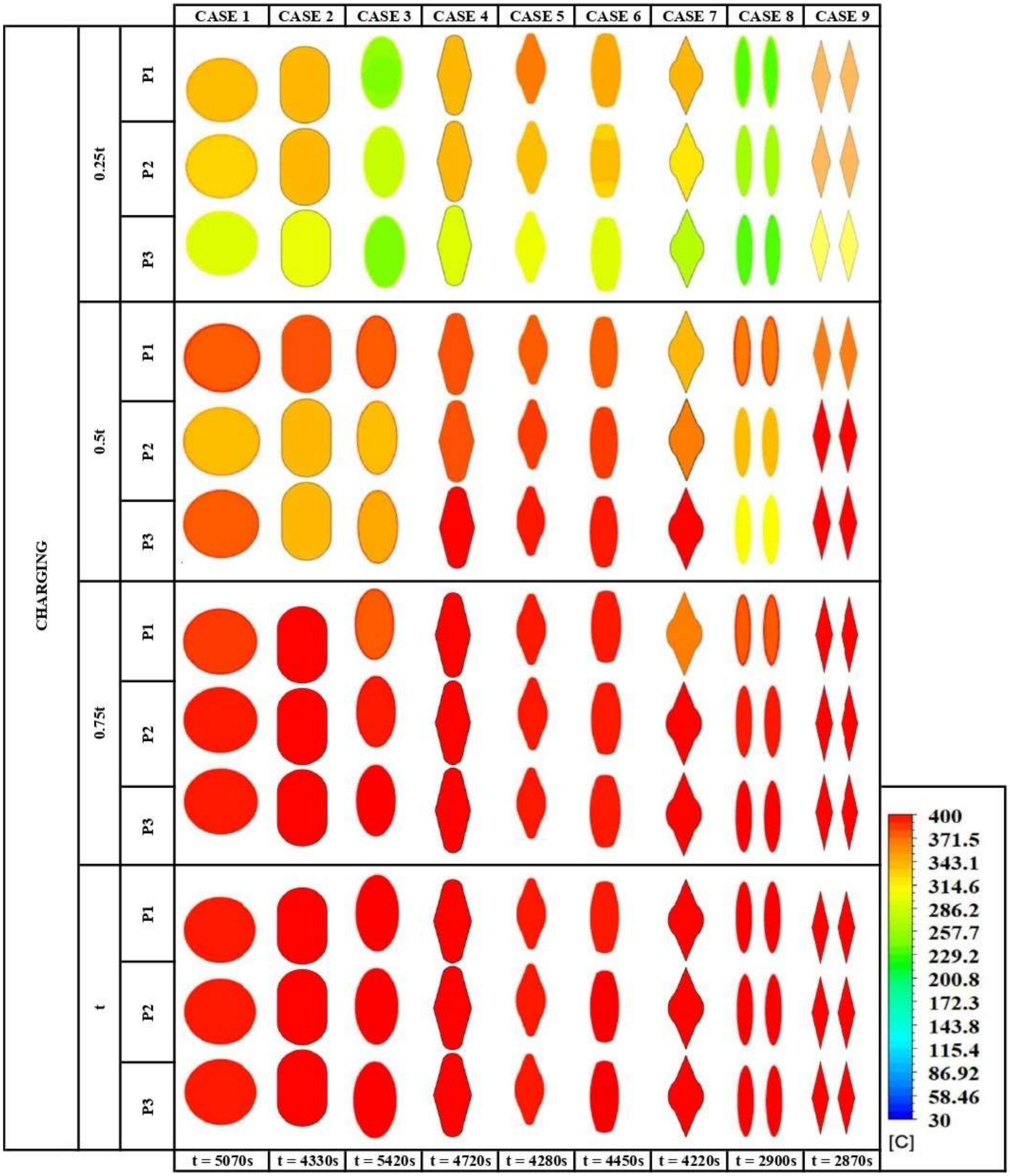

Figure 5-20: Transient Temperature Contours for Charging Cycle Cases 1-9 (Layout 2)

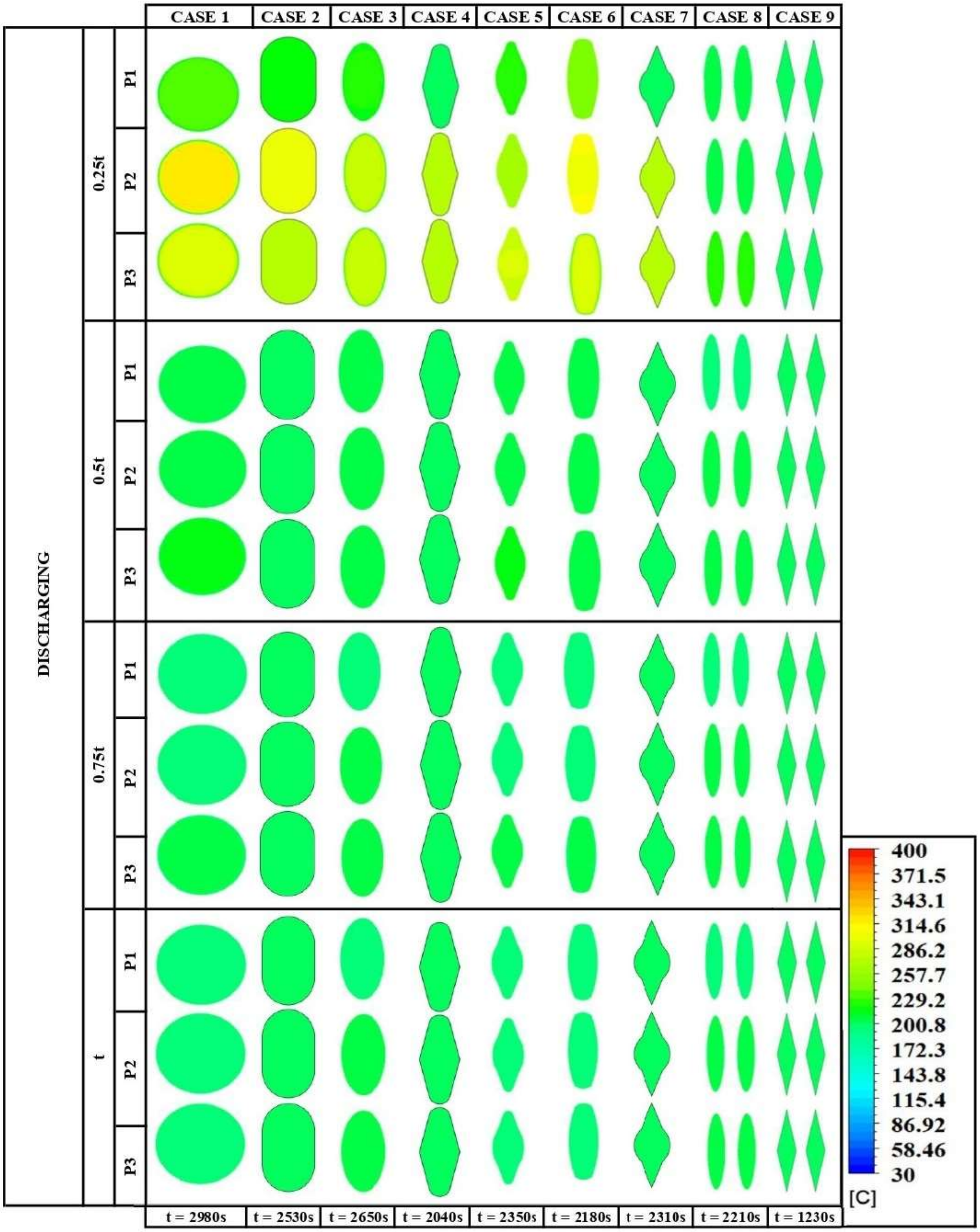

Figure 5-21: Transient Temperature Contours for Discharging Cycle Cases 1-9 (Layout 2)

Figure 5-18, Figure 5-19, Figure 5-20, and Figure 5-21 depict the quarterly transient liquid fraction distributions inside the different capsule designs during charging and discharging of the packed bed TES. Figure 5-18 and Figure 5-19, represent the first packed bed layout, Figure 5-20 and Figure 5-21 represent the second layout. The contours displayed are for each PCM indicator at the following time markers 0.25t, 0.5t, 0.75t and t (t = charging/discharging completion times for each capsule geometry).

Considering the first layout (Layout 1), At 0.25t, the contours all present similarities in temperature patterns during the charging phase. Case 4 and 6 at P1 are at much higher temperatures, with Case 4 being the highest. This can be attributed to its nigh-cylinder design. P2 and P3 contours for each case are similar. There is some differential temperature patterns in Case 6 which is a result of tapering towards the edge of the capsule. At 0.5t (charging), the temperature distributions are fairly uniformly at P1. The temperature pattern at P3 are identical across all the cases in indicating a closer approach to thermal equilibrium with the inlet HTF. From 0.75t to t (Charging), the temperatures only vary by a few degrees hence the identical temperature distributions before converging at the HTF inlet temperature. The discharge temperature contours are very much identical after 0.25t. This is the result of short discharge completion times and the bulk of the phase change process occurring before the 0.5t mark.

Considering the second layout (Layout 2), At 0.25t, the contours are greatly dissimilar in temperature patterns during the charging phase. This is largely because of the orientation of the capsules in the packed bed hence, influencing HTF flow patterns resulting in varied thermal gradients in the capsules. A similar differential temperature pattern exists in Case 6 but is restricted to P2. At 0.5t (charging), the temperature distributions are still varied but to a relatively smaller degree. Some P3 temperatures are already approaching the HTF inlet temperature. From 0.75t to t (Charging), the temperatures only vary by a few degrees hence the identical temperature distributions (save for a few) before converging at the HTF inlet temperature. The discharge temperature contours are very much identical after 0.25t. This is the result of short discharge completion times and the bulk of the phase change process occurring before the 0.5t mark.

5.3 Comparative Data Analysis

5.3.1 PCM Encapsulation Performance Coefficients

The aim of studying the effects of different encapsulations in packed beds during the charging and discharging cycle is to determine the relative performance of each encapsulation as compared to that of the base spherical encapsulation in each of the cycles. For each encapsulation, two packed bed layouts are investigated. For thermal performance comparisons of each layout alongside each new encapsulation, a relative parameter, coefficient of performance, COP$_{rel}$, is employed.

$$COP_{rel,char} = \frac{\textit{Total char}\quad \textit{time of spherica}\ \ \textit{packed bed}}{\textit{Total char}\quad \textit{time of new encapsulation in packed bed}}$$

$$COP_{rel,discharg} = \frac{\textit{Total discharg}\quad \textit{time of spherica}\ \ \textit{packed bed}}{\textit{Total discharg}\quad \textit{time of new encapsulation in packed bed}}$$

$$COP_{rel,total} = \frac{\textit{Total cycle time of spherical packed bed}}{\textit{Total cycle time of new encapsulation in packed bed}}$$

The table below shows the summary of the simulation results in terms of charging and discharging durations for each encapsulation and layout.

Table 5-1: Summary of CFD Simulation Results

S/N	ENCAPSULATION GEOMETRY	LAYOUT 1 CHARGING TIME (s)	LAYOUT 1 DISCHARGING TIME (s)	LAYOUT 2 CHARGING TIME (s)	LAYOUT 2 DISCHARGING TIME (s)
1	SPHERE	5070	2980	6210	3360
2	ELLIPSOID	5420	2650	5400	2710
3	CYLINDER-SPHERE HYBRID	4330	2530	5090	2400
4	DOUBLE ARCED CONE	4280	2350	5670	2420
5	TOP CURVED CONE	4220	2310	5750	2820
6	ELLIPTICAL TORUS	2900	2210	4290	2320
7	OVALOID	4450	2180	6210	2360
8	HALF CAPPED CONE	4720	2040	6120	2690
9	BI-TRIANGULAR TORUS	2870	1230	4040	2080

In each case, each layout has layers of the same height $(\frac{1}{3}H)$ and identical porosities although the porosities vary between layout 1 and 2 as a result of the shape of the new capsule design and arrangement of the capsule in the bed. In case 1, the first layout's layers have porosities of 0.46 and the second layout's layers have porosities of 0.54 respectively. Considering the first comparison between case 2 and case 1, the layers of layout 1 and layout 2 for case 2 have the same height $(\frac{1}{3}H)$ and porosities of 0.40 and 0.51 respectively.

The heat transfer fluid passes through three levels of PCM encapsulation in each layout during charging, and after exchanging thermal energy in each layer, it exits the tank until the charging process of the packed bed is complete. During discharging, the procedure is the same as during charging, with the exception that the intake temperature is lower than the PCM temperature post charging.

Comparison 1 (Case 2/ Case 1)	
Layout 1	Layout 2
$COP_{rel,cha} = \frac{5070}{4330} = 1.171$ $COP_{rel,discharge} = \frac{2980}{2530} = 1.178$ $COP_{rel,total} = \frac{5070 + 2980}{4330\ + 2530} = 1.173$	$COP_{rel,charge} = \frac{6210}{5090} = 1.22$ $COP_{rel,discharge} = \frac{3360}{2400} = 1.4$ $COP_{rel,total} = \frac{6210 + 3360}{5090 + 2400} = 1.278$

Considering the second comparison between case 3 and case 1, the layers of layout 1 and layout 2 for case 3 have the same height ($\frac{1}{3}H$) and porosities of 0.47 and 0.55 respectively.

Comparison 2 (Case 3/ Case 1)	
Layout 1	Layout 2
$COP_{rel,charge} = \frac{5070}{5420} = 0.935$ $COP_{rel,discharge} = \frac{2980}{2650} = 1.124$ $COP_{rel,total} = \frac{5070 + 2980}{5420\ + 2650} = 0.997$	$COP_{rel,charg} = \frac{6210}{5400} = 1.15$ $COP_{rel,discharge} = \frac{3360}{2710} = 1.24$ $COP_{rel,total} = \frac{6210 + 3360}{5400 + 2710} = 1.18$

Considering the third comparison between case 4 and case 1, the layers of layout 1 and layout 2 for case 4 have the same height ($\frac{1}{3}H$) and porosities of 0.55 and 0.62 respectively.

Comparison 3 (Case 4/ Case 1)	
Layout 1	Layout 2
$COP_{rel,char} = \frac{5070}{4720} = 1.074$ $COP_{rel,discharge} = \frac{2980}{2040} = 1.46$ $COP_{rel,total} = \frac{5070 + 2980}{4720 + 2040} = 1.19$	$COP_{rel,charge} = \frac{6210}{6120} = 1.014$ $COP_{rel,discharge} = \frac{3360}{2690} = 1.249$ $COP_{rel,total} = \frac{6210 + 3360}{6120 + 2690} = 1.086$

Considering the fourth comparison between case 5 and case 1, the layers of layout 1 and layout 2 for case 5 have the same height $(\frac{1}{3}H)$ and porosities of 0.55 and 0.61 respectively.

Comparison 4 (Case 5/ Case 1)	
Layout 1	Layout 2
$COP_{rel,charge} = \frac{5070}{4280} = 1.184$ $COP_{rel,discharg} = \frac{2980}{2350} = 1.268$ $COP_{rel,total} = \frac{5070 + 2980}{4280 + 2350} = 1.214$	$COP_{rel,charg} = \frac{6210}{5670} = 1.095$ $COP_{rel,discharge} = \frac{3360}{2420} = 1.388$ $COP_{rel,total} = \frac{6210 + 3360}{5670 + 2420} = 1.183$

Considering the fifth comparison between case 6 and case 1, the layers of layout 1 and layout 2 for case 6 have the same height $(\frac{1}{3}H)$ and porosities of 0.45 and 0.57 respectively.

Comparison 5 (Case 6/ Case 1)	
Layout 1	Layout 2
$COP_{rel,charg} = \frac{5070}{4450} = 1.139$ $COP_{rel,discharge} = \frac{2980}{2180} = 1.367$ $COP_{rel,total} = \frac{5070 + 2980}{4450 + 2180} = 1.214$	$COP_{rel,charge} = \frac{6210}{6210} = 1$ $COP_{rel,discharge} = \frac{3360}{2360} = 1.424$ $COP_{rel,total} = \frac{6210 + 3360}{6210 + 2360} = 1.117$

Considering the sixth comparison between case 7 and case 1, the layers of layout 1 and layout 2 for case 7 have the same height $(\frac{1}{3}H)$ and porosities of 0.61 and 0.63 respectively.

Comparison 6 (Case 7/ Case 1)	
Layout 1	Layout 2
$COP_{rel,charg} = \frac{5070}{4220} = 1.201$ $COP_{rel,discharge} = \frac{2980}{2310} = 1.29$ $COP_{rel,total} = \frac{5070 + 2980}{4220 + 2310} = 1.233$	$COP_{rel,charg} = \frac{6210}{5750} = 1.08$ $COP_{rel,discharg} = \frac{3360}{2820} = 1.191$ $COP_{rel,total} = \frac{6210 + 3360}{5750 + 2820} = 1.117$

Considering the seventh comparison between case 8 and case 1, the layers of layout 1 and layout 2 for case 8 have the same height $(\frac{1}{3}H)$ and porosities of 0.42 and 0.55 respectively. By virtue of its design, the hollow present in the elliptical torus permits inner and outer thermal energy exchange which is evidenced by the higher $\text{COP}_{\text{rel.total}}$ values for each layout in comparison 7.

Comparison 7 (Case 8/ Case 1)	
Layout 1	Layout 2
$COP_{rel,char} = \frac{5070}{2900} = 1.748$ $COP_{rel,discharge} = \frac{2980}{2210} = 1.348$ $COP_{rel,total} = \frac{5070+2980}{2900\ +2210} = 1.575$	$COP_{rel,charg} = \frac{6210}{4290} = 1.447$ $COP_{rel,discharge} = \frac{3360}{2320} = 1.448$ $COP_{rel,total} = \frac{6210+3360}{4290+2320} = 1.448$

Considering the eight comparison between case 9 and case 1, the layers of layout 1 and layout 2 for case 3 have the same height $(\frac{1}{3}H)$ and porosities of 0.57 and 0.65 respectively. By virtue of its design, the bi-triangular torus has the highest surface area of all the encapsulation. The hollow present in this design permits thermal energy exchange on two fronts which is evidenced by the higher $\text{COP}_{\text{rel.total}}$ values for each layout in comparison 8.

Comparison 8 (Case 9/ Case 1)	
Layout 1	Layout 2
$COP_{rel,charge} = \frac{5070}{2870} = 1.766$ $COP_{rel,discharge} = \frac{2980}{1230} = 2.423$ $COP_{rel,total} = \frac{5070+2980}{2870+1230} = 1.963$	$COP_{rel,charge} = \frac{6210}{4040} = 1.537$ $COP_{rel,discharge} = \frac{3360}{2080} = 1.615$ $COP_{rel,total} = \frac{6210+3360}{4040+2080} = 1.564$

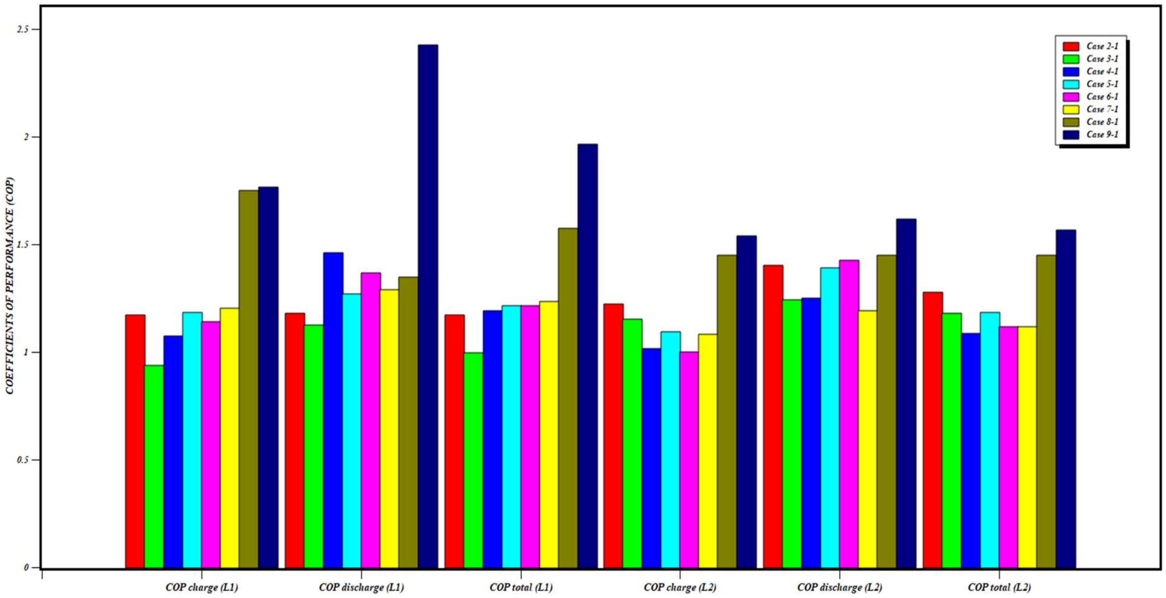

Figure 5-22: Composite bar chart for COP distributions

The composite bar chart shows the COP distributions for each case pair as well as the related layouts during the charging and discharging cycles. As demonstrated in the above chart, the COP values of layout 1 are indicative of the fact that layout 1 outperforms layout 2 in terms of performance. The porosity of the bed in layout 1 contributes significantly to the better performance of the layout when compared to the performance of layout 2. The parallel positioning of the capsules in layout 1 allows for a higher packing density at the expense of a longer bed length, which is advantageous in some cases. Layout 2 shortens the length of the bed in the majority of cases at the expense of increasing the diameter.

The charging and discharging cycle periods of layout 2 are much longer than those of layout 1. This is a significant disadvantage compared to layout 1. In the base (case 1), the charging and discharging cycle times in layout 1 are 5070s and 2980s and 6210s and 3360s in layout 2 respectively.

In comparison 1, the COP values of layout 2 are higher than those of layout 1. This is true for comparison 2. In proportion to the rise in percentage area of the capsules, the COP values of layout 1 gradually increase above those of layout 2. This rise may be seen in the COPs of the charging cycle as well as the COP of the total cycle. The discharge COP values for layout 1 in comparisons 4, 5, and 7 are lower than those for layout 2. In comparisons 3, 6 and 8, the discharge COP values in layout 1 are significantly greater than those of the layout 2.

5.3.2 Percentage Change Ratios (Cycle Times vs Bed Dimensions)

From the results above, it can be observed that with each new capsule design, there is an increase in total surface area per capsule at while maintaining a constant volume with the base case (sphere capsules). This increase in area with each new capsule design results in a relative decrease in charging and discharging time hence increased performance of the cascaded thermal energy storage system. These performance increases come with a change in the dimension of the packed bed. The packed bed diameters decrease and the bed lengths increase respectively with each new case/ capsule design. The bed dimension changes are a result of the collective increase of the capsule dimensions in the direction of the heat transfer fluid. In order to determine which capsule design is most suitable to be employed in practice considering the packed bed dimension changes the following percentage change ratios have been evaluated for each layout and capsule design with respect to the base case;

- $\Delta PR_{CT-B} = \frac{\Delta Charging\ Cycle\ Time}{\Delta Bed\ Lengt}$
- $\Delta PR_{DT-BL} = \frac{\Delta Discharging\ Cycle\ Time}{\Delta Bed\ Length}$
- $\Delta PR_{CT-BD} = \frac{\Delta ChargingCycl\quad Time}{\Delta Bed\ Diameter}$
- $\Delta PR_{DT-} = \frac{\Delta Disharging\ Cycle\ Time}{\Delta Bed\ Length}$

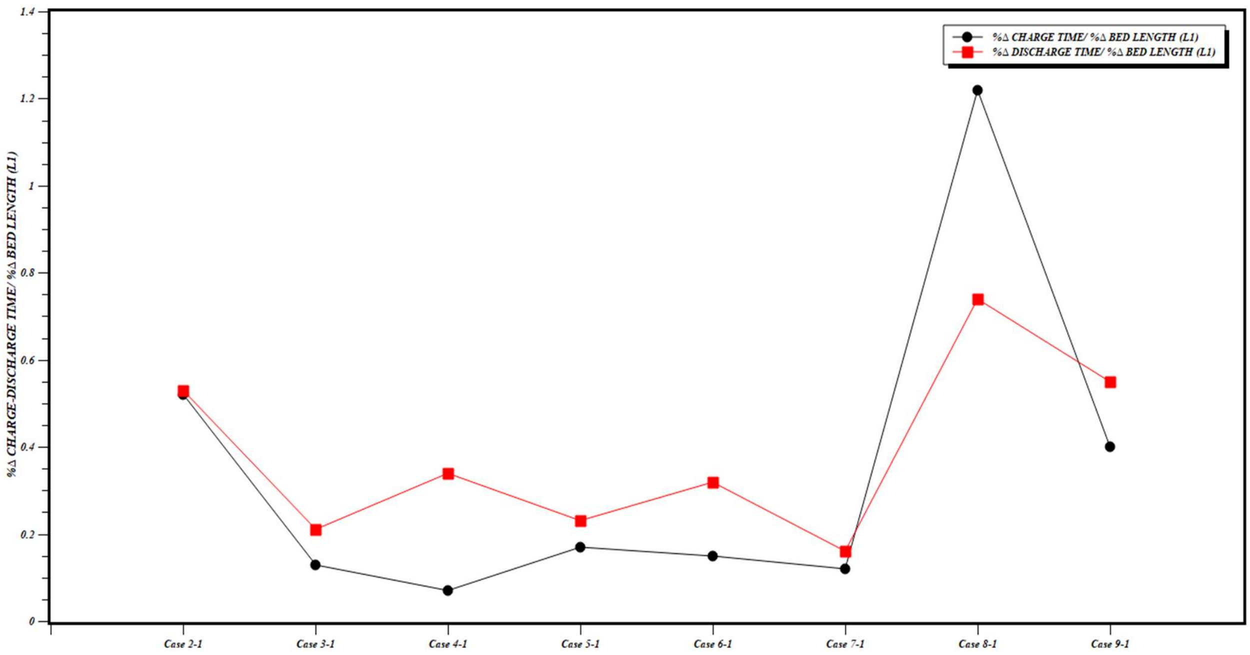

Figure 5-23: Percentage Change Ratios between Charging, Discharging cycle times and Bed Length for Layout 1

Figure 5-23 illustrates the percentage change ratios of layout 1 between the charging, discharge cycle times and bed lengths of each of the respective cases. Case 8-1 (Elliptical Torus) presents the best percentage ratio in both charging and discharging cycles. The elliptical torus having the highest change percentage ratio indicates that in comparison to all the proposed capsule designs, it performs optimally and without significantly engorging the bed length size of the thermal energy storage system.

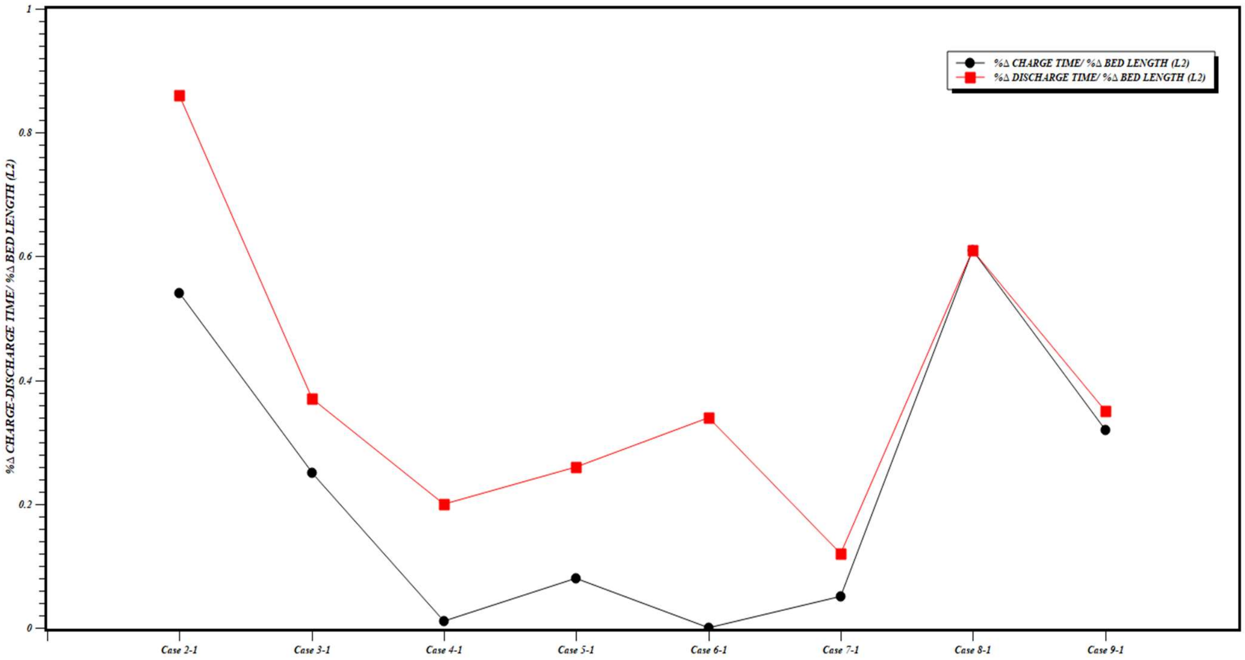

Figure 5-24: Percentage Change Ratios between Charge, Discharge times and Bed Length for Layout 2

Figure 5-24 illustrates the percentage change ratios of layout 2 between the charging, discharge cycle times and bed lengths of each of the respective cases. Case 8-1 (Elliptical Torus) presents the best percentage ratio in the charging cycle. Case 2-1 (Cylinder-Sphere Hybrid) presents the best percentage ratio in the discharging cycle. Case 8-1 and Case 2-1 are the most suitable capsule designs presenting optimal performances while keeping the bed length increase minimized.

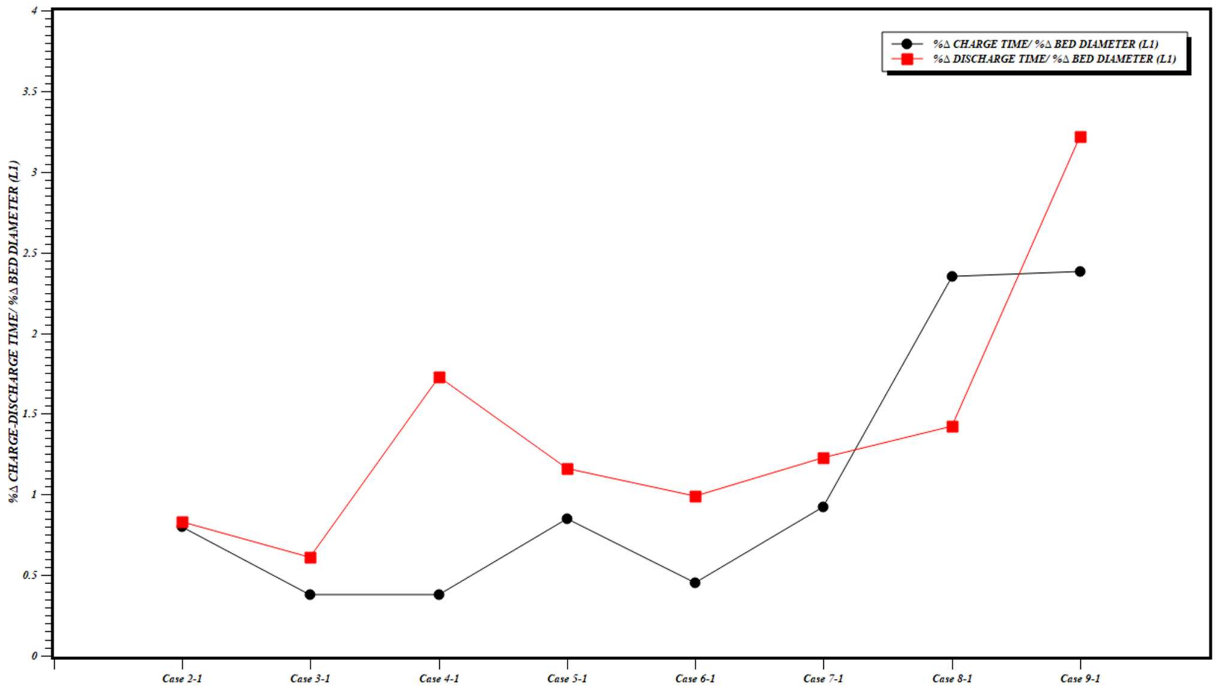

Figure 5-25: Percentage Change Ratios between Charge, Discharge times and Bed Diameter for Layout 1

Figure 5-25 illustrates the percentage change ratios of layout 1 between the charging, discharge cycle times and bed diameters of each of the respective cases. Case 9-1 (Bi-Triangular Torus) presents the best percentage change ratio in both charging and discharging cycles. The bi-triangular torus having the highest change percentage ratio indicates that in comparison to all the proposed capsule designs, it performs optimally with the decreased bed diameter of the thermal energy storage system. Case 8-1 has the next optimal percentage change ratio in charging cycle while Case 4-1 has the next optimal percentage change ratio in the discharge cycle.

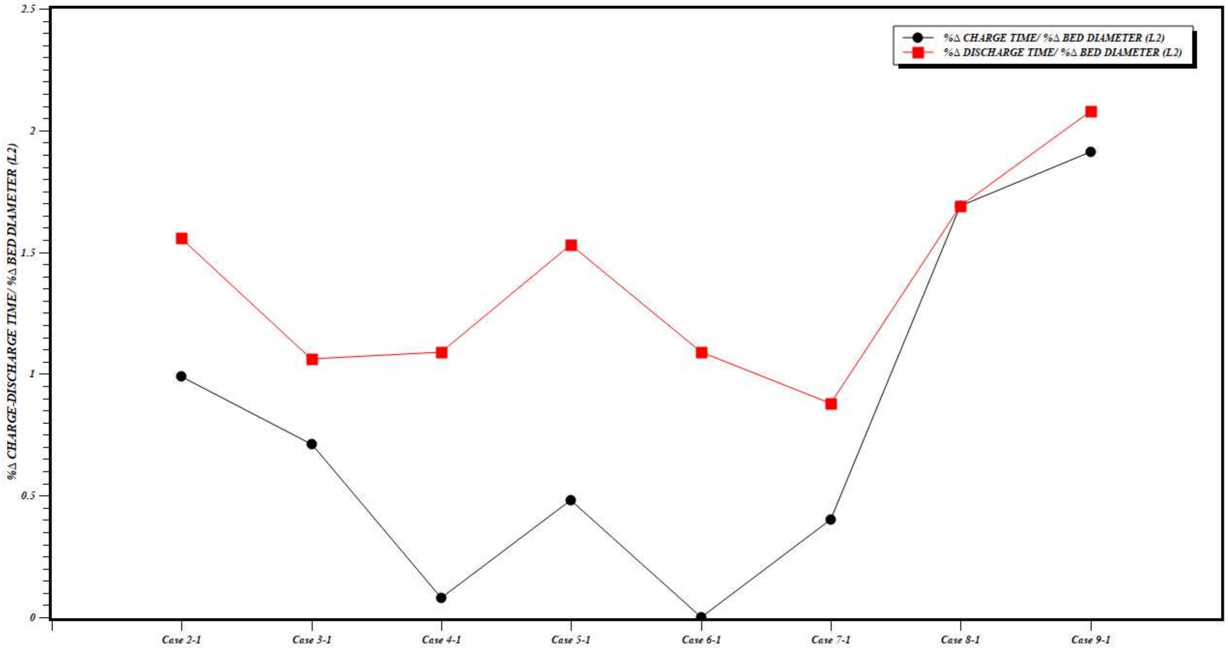

Figure 5-26: Percentage Change Ratios between Charge, Discharge times and Bed Diameter for Layout 2

Figure 5-26 illustrates the percentage change ratios of layout 2 between the charging, discharge cycle times and bed diameters of each of the respective cases. Case 9-1 (Bi-Triangular Torus) presents the best percentage change ratio in both charging and discharging cycles. The bi-triangular torus having the highest change percentage ratio indicates that in comparison to all the proposed capsule designs, it performs optimally with the decreased bed diameter of the thermal energy storage system. Case 8-1 has the next optimal percentage change ratio in both the charging and discharging cycle.

CHAPTER SIX

6. Summary, Conclusion and Recommendations

6.1 Summary

A growing concern in recent years has been the increasing amount of greenhouse gases in the environment caused by the burning of high-priced fossil fuels and other energy sources with a high carbon footprint. As a result, the harvesting and utilization of renewable energy resources has received a great deal of attention. Solar energy is the most abundant of all of the renewable energy sources available today. In order to assist in fulfilling energy demands, there is a critical need for the development of efficient solar power systems. Multiple research are being undertaken to study methods of improving the performance of thermal energy storage systems as well as to propose new design concepts that are more cost effective and efficient than existing designs. The investigation of dominant elements that influence the performance of thermal energy storage systems, as well as the development of innovative methods of enhancing their efficiency, are now underway.

Chapter 2 of this dissertation summarizes pertinent information regarding some fundamental concepts, the operation of concentrated solar power systems, thermodynamic cycles that can incorporate CSP systems, thermal energy storage systems and performance enhancement techniques, and phase change materials, their classifications, and applications. Chapter 3 introduced numerical approaches for efficiently modeling latent heat thermal energy storage systems. This chapter addresses the various numerical modeling techniques used to analyze heat transfer in phase-change materials and the mathematical models developed to simulate heat transfer during phase transitions in two and three dimensions. A validation study was performed and presented in chapter 4 in which the proposed computational fluid dynamics model was validated against experimental results. An experiment which involved the testing the temperature distributions within a packed bed latent heat storage system with encapsulated phase change materials during the charging cycle. This chapter also introduces the concept of computational fluid dynamics, the new proposed capsule designs and bed layouts as well as the governing equations guiding the simulations. Novel PCM capsule designs as well as the base design was presented this chapter. The novel PCM capsule designs included geometric shapes and properties that had the potential to produce higher thermal efficiencies by increasing the heat transfer area while maintaining the same volume of the base design. The performance findings of each of the unique PCM encapsulations were presented in Chapter 5, along with temperature and liquid fraction distributions throughout the PCM indicators and a comparative data analysis of the simulation results of the performance of novel designs vs the base design.

6.2 Conclusion

Computational fluid dynamic models were developed to investigate the charging and discharging processes of a 3-stage cascaded packed bed thermal energy storage system. The CFD simulations were carried out by ANSYS Fluent 2021 R2. The effect of arranging PCMs inside the tank in ascending and descending order of phase change temperature during the charging and discharging cycles is investigated. The influence of employing new PCM capsule designs with increased surface area and equal volumes is studied and as expected it is found that increasing the area of the capsules decreases the completion time of the charging and discharging of the packed bed. The influence of layout configuration aimed at improving the thermal performance of the packed bed is investigated and it is found that layout 1 provides better thermal performance by way of shorter completion durations in comparison to layout 2.

Furthermore, by employing percentage change ratios of the decrease in charging and discharging duration and the bed length and diameter, the elliptical torus encapsulation provided the best thermal performance with a 35.04% increase in bed length for layout 1 and a 50.69% bed length increase in layout 2. The results demonstrate that by modifying the geometric design of the PCM encapsulations, one can achieve a thermal performance that is more advantageous for the intended purpose.

6.3 Recommendations

Regardless of the study's success, recommendations can be made to help with future research and development of cascaded thermal energy storage devices.

The approach of modeling the cascaded packed bed thermal energy storage using computational fluid dynamics was validated.

With the introduction of new PCM encapsulation designs, the thermal energy storage systems have improved in thermal performance. In order to establish whether the trade-off between energy efficiency and economic efficiency is realistic in thermal energy storage systems, an investigation into the economic aspects of applying these new capsule designs in thermal energy storage systems can be done.

To improve the overall thermal performance of a cascaded thermal energy storage system, additional research into the influence of bed layout with the new capsule designs should be done.

References

[1] A. Raul, M. Jain, S. Gaikwad, and S. K. Saha, “Modelling and experimental study of latent heat thermal energy storage with encapsulated PCMs for solar thermal applications,” *Appl. Therm. Eng.*, vol. 143, pp. 415–428, Oct. 2018, doi: 10.1016/j.applthermaleng.2018.07.123.

[2] H. Mehling and L. F. Cabeza, *Heat and cold storage with PCM: An up to date introduction into basics and applications*. Berlin, Heidelberg: Springer Berlin Heidelberg, 2008. doi: 10.1007/978-3-540-68557-9.

[3] S. Jegadheeswaran and S. D. Pohekar, “Performance enhancement in latent heat thermal storage system: A review,” *Renew. Sustain. Energy Rev.*, vol. 13, no. 9, pp. 2225–2244, Dec. 2009, doi: 10.1016/j.rser.2009.06.024.

[4] I. Sarbu and A. Dorca, “Review on heat transfer analysis in thermal energy storage using latent heat storage systems and phase change materials,” *Int. J. Energy Res.*, vol. 43, no. 1, pp. 29–64, 2019, doi: 10.1002/er.4196.

[5] Q. Mao and Y. Zhang, “Study on the thermal storage performance of a new cascade structure phase change thermal storage tank,” *J. Energy Storage*, vol. 56, p. 106155, Dec. 2022, doi: 10.1016/j.est.2022.106155.

[6] H. Gupta, P. Verma, K. Dhiman, P. Chaudhary, and N. Khandelwal, “Analysis of Cascade Thermal Energy Storage System,” in *Recent Trends in Thermal and Fluid Sciences*, Singapore, 2023, pp. 131–146. doi: 10.1007/978-981-19-3498-8_12.

[7] I. Sarbu, “Thermal Energy Storage,” in *Advances in Building Services Engineering: Studies, Researches and Applications*, I. Sarbu, Ed. Cham: Springer International Publishing, 2021, pp. 559–627. doi: 10.1007/978-3-030-64781-0_7.

[8] “The Atlas of African Affairs | Ieuan L.l. Griffiths | Taylor & Francis.” https://www.taylorfrancis.com/books/mono/10.4324/9780203713785/atlas-african-affairs-ieuan-griffiths (accessed Jan. 17, 2023).

[9] “Global Solar Atlas.” https://globalsolaratlas.info/download/sub-saharan-africa (accessed Apr. 27, 2020).

[10] Z. Liu, *Global energy interconnection*. Amsterdam: Elsevier/AP, 2015.

[11] I. M. Bugaje, “Renewable energy for sustainable development in Africa: a review,” *Renew. Sustain. Energy Rev.*, vol. 10, no. 6, pp. 603–612, Dec. 2006, doi: 10.1016/j.rser.2004.11.002.

[12] S. Kraemer, “Novel CSP Design Combines the Solar Receiver with Thermal Energy Storage,” *SolarPACES*, Sep. 10, 2019. https://www.solarpaces.org/novel-csp-design-combines-the-solar-receiver-with-thermal-energy-storage/ (accessed Dec. 15, 2022).

[13] “The Edge of Space | Science Mission Directorate.” https://science.nasa.gov/edge-space (accessed Dec. 15, 2022).

[14] M. Geyer and W. Stine, *Power From The Sun*. 2001.

[15] Y. Tian and C. Y. Zhao, “A review of solar collectors and thermal energy storage in solar thermal applications,” *Appl. Energy*, vol. 104, pp. 538–553, Apr. 2013, doi: 10.1016/j.apenergy.2012.11.051.

[16] “Glossary of Technical Renewable Energy Terminology :: Support :: 3TIER.” https://www.3tier.com/en/support/glossary/ (accessed Apr. 27, 2020).

[17] “Solar Radiation Basics,” *Energy.gov*. https://www.energy.gov/eere/solar/solar-radiation-basics (accessed Dec. 15, 2022).

[18] V. V. Tyagi, S. C. Kaushik, and S. K. Tyagi, “Advancement in solar photovoltaic/thermal (PV/T) hybrid collector technology,” *Renew. Sustain. Energy Rev.*, vol. 16, no. 3, pp. 1383–1398, Apr. 2012, doi: 10.1016/j.rser.2011.12.013.

[19] J. Santamarta, “Concentrated Solar Power Overview,” *HELIOSCSP*. https://helioscsp.com/concentrated-solar-power-overview/ (accessed Dec. 15, 2022).

[20] S. Kalogirou, *Solar energy engineering: processes and systems*, Second edition. Amsterdam ; Boston: Elsevier, AP, Academic Press is an imprint of Elsevier, 2014.

[21] S. Qazi, “Chapter 7 - Solar Thermal Electricity and Solar Insolation,” in *Standalone Photovoltaic (PV) Systems for Disaster Relief and Remote Areas*, S. Qazi, Ed. Elsevier, 2017, pp. 203–237. doi: 10.1016/B978-0-12-803022-6.00007-1.

[22] G. Morin, J. Dersch, W. Platzer, M. Eck, and A. Häberle, “Comparison of Linear Fresnel and Parabolic Trough Collector power plants,” *Sol. Energy*, vol. 86, no. 1, pp. 1–12, Jan. 2012, doi: 10.1016/j.solener.2011.06.020.

[23] F. J. Cabrera, A. Fernández-García, R. M. P. Silva, and M. Pérez-García, “Use of parabolic trough solar collectors for solar refrigeration and air-conditioning applications,” *Renew. Sustain. Energy Rev.*, vol. 20, pp. 103–118, Apr. 2013, doi: 10.1016/j.rser.2012.11.081.

[24] M. J. Blanco and S. Miller, “1 - Introduction to concentrating solar thermal (CST) technologies,” in *Advances in Concentrating Solar Thermal Research and Technology*, M. J. Blanco and L. R. Santigosa, Eds. Woodhead Publishing, 2017, pp. 3–25. doi: 10.1016/B978-0-08-100516-3.00001-0.

[25] L. G. Pheng, R. Affandi, M. R. Ab Ghani, C. K. Gan, Z. Jano, and T. Sutikno, “A Review of Parabolic Dish-Stirling Engine System Based on Concentrating Solar Power,” *TELKOMNIKA Telecommun. Comput. Electron. Control*, vol. 12, no. 4, p. 1142, Dec. 2014, doi: 10.12928/telkomnika.v12i4.1132.

[26] S. Karellas and T. C. Roumpedakis, “Chapter 7 - Solar thermal power plants,” in *Solar Hydrogen Production*, F. Calise, M. D. D’Accadia, M. Santarelli, A. Lanzini, and D. Ferrero, Eds. Academic Press, 2019, pp. 179–235. doi: 10.1016/B978-0-12-814853-2.00007-2.

[27] O. Behar, A. Khellaf, and K. Mohammedi, “A review of studies on central receiver solar thermal power plants,” *Renew. Sustain. Energy Rev.*, vol. 23, pp. 12–39, Jul. 2013, doi: 10.1016/j.rser.2013.02.017.

[28] W. G. Roux, T. Bello-Ochende, and J. P. Meyer, “Thermodynamic optimisation of the integrated design of a small-scale solar thermal Brayton cycle: Solar thermal Brayton cycle optimisation,” *Int. J. Energy Res.*, vol. 36, no. 11, pp. 1088–1104, Sep. 2012, doi: 10.1002/er.1859.

[29] W. G. Le Roux, T. Bello-Ochende, and J. P. Meyer, “The efficiency of an open-cavity tubular solar receiver for a small-scale solar thermal Brayton cycle,” *Energy Convers. Manag.*, vol. 84, pp. 457–470, Aug. 2014, doi: 10.1016/j.enconman.2014.04.048.

[30] M. R. Patel, *Wind and solar power systems: design, analysis, and operation*, 2nd ed. Boca Raton, FL: Taylor & Francis, 2006.

[31] L. Kayofa, “Feasibility study and business plan for manufacturing a 3 kW-electrical solar Stirling engine and dish for stand-alone power supply units,” 2015.

[32] D. Mills, “Advances in solar thermal electricity technology,” *Sol. Energy*, vol. 76, no. 1, pp. 19–31, Jan. 2004, doi: 10.1016/S0038-092X(03)00102-6.

[33] “mcensustainableenergy / Solar Parabolic Dish CSP.” http://mcensustainableenergy.pbworks.com/w/page/32178486/Solar%20Parabolic%20Dish%20CSP (accessed Aug. 29, 2022).

[34] M. T. Dunham and B. D. Iverson, “High-efficiency thermodynamic power cycles for concentrated solar power systems,” *Renew. Sustain. Energy Rev.*, vol. 30, pp. 758–770, Feb. 2014, doi: 10.1016/j.rser.2013.11.010.

[35] C. Tzivanidis, E. Bellos, and K. A. Antonopoulos, “Energetic and financial investigation of a stand-alone solar-thermal Organic Rankine Cycle power plant,” *Energy Convers. Manag.*, vol. 126, pp. 421–433, Oct. 2016, doi: 10.1016/j.enconman.2016.08.033.

[36] S. Ogriseck, “Integration of Kalina cycle in a combined heat and power plant, a case study,” *Appl. Therm. Eng.*, vol. 29, no. 14, pp. 2843–2848, Oct. 2009, doi: 10.1016/j.applthermaleng.2009.02.006.

[37] M. T. Dunham and B. D. Iverson, “High-efficiency thermodynamic power cycles for concentrated solar power systems,” *Renew. Sustain. Energy Rev.*, vol. 30, pp. 758–770, Feb. 2014, doi: 10.1016/j.rser.2013.11.010.

[38] A. El Fadar, “Novel process for performance enhancement of a solar continuous adsorption cooling system,” *Energy*, vol. 114, pp. 10–23, Nov. 2016, doi: 10.1016/j.energy.2016.07.149.

[39] G. A. Lane and N. Shamsundar, “Solar Heat Storage: Latent Heat Materials, Vol. I: Background and Scientific Principles,” *J. Sol. Energy Eng.*, vol. 105, no. 4, p. 467, Nov. 1983, doi: 10.1115/1.3266412.

[40] M. Mofijur *et al.*, “Phase Change Materials (PCM) for Solar Energy Usages and Storage: An Overview,” *Energies*, vol. 12, no. 16, Art. no. 16, Jan. 2019, doi: 10.3390/en12163167.

[41] A. Sharma, V. V. Tyagi, C. R. Chen, and D. Buddhi, “Review on thermal energy storage with phase change materials and applications,” *Renew. Sustain. Energy Rev.*, vol. 13, no. 2, pp. 318–345, Feb. 2009, doi: 10.1016/j.rser.2007.10.005.

[42] G. Hailu, “8 - Energy systems in buildings,” in *Energy Services Fundamentals and Financing*, D. Borge-Diez and E. Rosales-Asensio, Eds. Academic Press, 2021, pp. 181–209. doi: 10.1016/B978-0-12-820592-1.00008-7.

[43] I. Sarbu and A. Dorca, “Review on heat transfer analysis in thermal energy storage using latent heat storage systems and phase change materials,” *Int. J. Energy Res.*, vol. 43, no. 1, pp. 29–64, Jan. 2019, doi: 10.1002/er.4196.

[44] “Revision Change Compare | Encyclopedia MDPI.” https://encyclopedia.pub/item/compare_revision/04534b967b158a856a212f121ba668e5/-1 (accessed Aug. 31, 2022).

[45] I. Sarbu and C. Sebarchievici, “A Comprehensive Review of Thermal Energy Storage,” *Sustainability*, vol. 10, no. 1, p. 191, Jan. 2018, doi: 10.3390/su10010191.

[46] M. M. Farid, A. M. Khudhair, S. A. K. Razack, and S. Al-Hallaj, “A review on phase change energy storage: materials and applications,” *Energy Convers. Manag.*, vol. 45, no. 9, pp. 1597–1615, Jun. 2004, doi: 10.1016/j.enconman.2003.09.015.

[47] S. Rajendrasiva, “EXPERIMENTAL INVESTIGATION ON PHASE CHANGE MATERIALS,” no. 6, p. 6, 2015.

[48] Y. B. Tao and Y.-L. He, “A review of phase change material and performance enhancement method for latent heat storage system,” *Renew. Sustain. Energy Rev.*, vol. 93, pp. 245–259, Oct. 2018, doi: 10.1016/j.rser.2018.05.028.

[49] Y. B. Tao and Y.-L. He, “A review of phase change material and performance enhancement method for latent heat storage system,” *Renew. Sustain. Energy Rev.*, vol. 93, pp. 245–259, Oct. 2018, doi: 10.1016/j.rser.2018.05.028.

[50] O. Achkari and A. El Fadar, “Latest developments on TES and CSP technologies – Energy and environmental issues, applications and research trends,” *Appl. Therm. Eng.*, vol. 167, p. 114806, Feb. 2020, doi: 10.1016/j.applthermaleng.2019.114806.

[51] J. N. W. Chiu and V. Martin, “Multistage latent heat cold thermal energy storage design analysis,” *Appl. Energy*, vol. 112, pp. 1438–1445, Dec. 2013, doi: 10.1016/j.apenergy.2013.01.054.

[52] M. M. Farid and A. Kanzawa, “Thermal Performance of a Heat Storage Module Using PCM’s With Different Melting Temperatures: Mathematical Modeling,” *J. Sol. Energy Eng.*, vol. 111, no. 2, pp. 152–157, May 1989, doi: 10.1115/1.3268301.

[53] H. J. Xu and C. Y. Zhao, “Thermal performance of cascaded thermal storage with phase-change materials (PCMs). Part I: Steady cases,” *Int. J. Heat Mass Transf.*, vol. 106, pp. 932–944, Mar. 2017, doi: 10.1016/j.ijheatmasstransfer.2016.10.054.

[54] D. Laing, W.-D. Steinmann, R. Tamme, and C. Richter, “Solid media thermal storage for parabolic trough power plants,” *Sol. Energy*, vol. 80, no. 10, pp. 1283–1289, Oct. 2006, doi: 10.1016/j.solener.2006.06.003.

[55] H. J. Xu and C. Y. Zhao, “Thermodynamic analysis and optimization of cascaded latent heat storage system for energy efficient utilization,” *Energy*, vol. 90, pp. 1662–1673, Oct. 2015, doi: 10.1016/j.energy.2015.06.131.

[56] T. K. Aldoss and M. M. Rahman, “Comparison between the single-PCM and multi-PCM thermal energy storage design,” *Energy Convers. Manag.*, vol. 83, pp. 79–87, Jul. 2014, doi: 10.1016/j.enconman.2014.03.047.

[57] Y. Zhang, G. Zhou, K. Lin, Q. Zhang, and H. Di, “Application of latent heat thermal energy storage in buildings: State-of-the-art and outlook,” *Build. Environ.*, vol. 42, no. 6, pp. 2197–2209, Jun. 2007, doi: 10.1016/j.buildenv.2006.07.023.

[58] H. Jouhara, A. Żabnieńska-Góra, N. Khordehgah, D. Ahmad, and T. Lipinski, “Latent thermal energy storage technologies and applications: A review,” *Int. J. Thermofluids*, vol. 5–6, p. 100039, Aug. 2020, doi: 10.1016/j.ijft.2020.100039.

[59] K. Kant, A. Shukla, A. Sharma, A. Kumar, and A. Jain, “Thermal energy storage based solar drying systems: A review,” *Innov. Food Sci. Emerg. Technol.*, vol. 34, pp. 86–99, Apr. 2016, doi: 10.1016/j.ifset.2016.01.007.

[60] “Conduction of Heat through a Sphere | Thermal Engineering,” *Engineering Notes India*, Dec. 07, 2017. https://www.engineeringenotes.com/thermal-engineering/heat-conduction/conduction-of-heat-through-a-sphere-thermal-engineering/30154 (accessed Aug. 04, 2021).

[61] “Yunus A Cengel Heat and mass transfer - HEAT AND MASS TRANSFER FUNDAMENTALS & APPLICATIONS - Studocu.” https://www.studocu.com/row/document/university-of-

engineering-and-technology-taxila/thermodynamics/yunus-a-cengel-heat-and-mass-transfer/17559376 (accessed Jan. 17, 2023).

[62] S. Koga and M. Krstic, “Control of the Stefan System and Applications: A Tutorial,” *Annu. Rev. Control Robot. Auton. Syst.*, vol. 5, no. 1, pp. 547–577, May 2022, doi: 10.1146/annurev-control-042920-014825.

[63] J. Stefan, “Ueber die Theorie der Eisbildung, insbesondere über die Eisbildung im Polarmeere,” *Ann. Phys.*, vol. 278, no. 2, pp. 269–286, 1891, doi: 10.1002/andp.18912780206.

[64] V. R. Voller and C. Prakash, “A fixed grid numerical modelling methodology for convection-diffusion mushy region phase-change problems,” *Int. J. Heat Mass Transf.*, vol. 30, no. 8, pp. 1709–1719, Aug. 1987, doi: 10.1016/0017-9310(87)90317-6.

[65] C. Amaral, R. Vicente, P. a. a. P. Marques, and A. Barros-Timmons, “Phase change materials and carbon nanostructures for thermal energy storage: A literature review,” *Renew. Sustain. Energy Rev.*, vol. 79, no. C, pp. 1212–1228, 2017.

[66] T. G. Myers and S. L. Mitchell, “Application of the combined integral method to Stefan problems,” *Appl. Math. Model.*, vol. 35, no. 9, pp. 4281–4294, Sep. 2011, doi: 10.1016/j.apm.2011.02.049.

[67] A. D. Solomon, “Melt time and heat flux for a simple PCM body,” *Sol. Energy*, vol. 22, no. 3, pp. 251–257, Jan. 1979, doi: 10.1016/0038-092X(79)90140-3.

[68] M. Lacroix, “Numerical simulation of a shell-and-tube latent heat thermal energy storage unit,” *Sol. Energy*, vol. 50, no. 4, pp. 357–367, Apr. 1993, doi: 10.1016/0038-092X(93)90029-N.

[69] Z.-X. Gong and A. Mujumdar, “Finite-element analysis of cyclic heat transfer in a shell-and-tube latent heat energy storage exchanger,” 1997, doi: 10.1016/S1359-4311(96)00054-3.

[70] R. Velraj, R. V. Seeniraj, B. Hafner, C. Faber, and K. Schwarzer, “Experimental analysis and numerical modelling of inward solidification on a finned vertical tube for a latent heat storage unit,” *Sol. Energy*, vol. 60, no. 5, pp. 281–290, Jun. 1997, doi: 10.1016/S0038-092X(96)00167-3.

[71] M. Faden, A. König-Haagen, S. Höhlein, and D. Brüggemann, “An implicit algorithm for melting and settling of phase change material inside macrocapsules,” *Int. J. Heat Mass Transf.*, vol. 117, pp. 757–767, Feb. 2018, doi: 10.1016/j.ijheatmasstransfer.2017.10.033.

[72] B. Zalba, J. M. Marín, L. F. Cabeza, and H. Mehling, “Review on thermal energy storage with phase change: materials, heat transfer analysis and applications,” *Appl. Therm. Eng.*, vol. 23, no. 3, pp. 251–283, Feb. 2003, doi: 10.1016/S1359-4311(02)00192-8.

[73] A. J. Dalhuijsen and A. Segal, “Comparison of finite element techniques for solidification problems,” *Int. J. Numer. Methods Eng.*, vol. 23, no. 10, pp. 1807–1829, 1986, doi: 10.1002/nme.1620231003.

[74] Y. Dutil, D. R. Rousse, N. B. Salah, S. Lassue, and L. Zalewski, “A review on phase-change materials: Mathematical modeling and simulations,” *Renew. Sustain. Energy Rev.*, vol. 15, no. 1, pp. 112–130, Jan. 2011, doi: 10.1016/j.rser.2010.06.011.

[75] F. Ghani, R. Waser, T. O’Donovan, P. Schuetz, M. Zaglio, and J. Worlitschek, “Non-linear system identification of a latent heat thermal energy storage system,” *Appl. Therm. Eng.*, vol. 134, Feb. 2018, doi: 10.1016/j.applthermaleng.2018.02.035.

[76] S. Liu, Y. Li, and Y. Zhang, “Review on Heat Transfer Mechanisms and Characteristics in Encapsulated PCMs,” *Heat Transf. Eng.*, vol. 36, no. 10, pp. 880–901, 2015, doi: 10.1080/01457632.2015.965093.

[77] B. T. F. Chung and L. T. Yeh, “Solidification and melting of materials subject to convection and radiation,” *J. Spacecr. Rockets*, vol. 12, no. 6, pp. 329–333, Jun. 1975, doi: 10.2514/3.27839.

[78] A. S. Wood, “A note on the use of the isotherm migration method,” *J. Comput. Appl. Math.*, vol. 36, no. 3, pp. 371–384, Sep. 1991, doi: 10.1016/0377-0427(91)90017-E.

[79] D. Buddhi, N. K. Bansal, R. L. Sawhney, and M. S. Sodha, “Solar thermal storage systems using phase change materials,” *Int. J. Energy Res.*, vol. 12, no. 3, 1988, doi: 10.1002/er.4440120318.

[80] J. Taler and P. Duda, Eds., “Melting and Solidification (Freezing),” in *Solving Direct and Inverse Heat Conduction Problems*, Berlin, Heidelberg: Springer, 2006, pp. 799–829. doi: 10.1007/978-3-540-33471-2_26.

[81] A. Lazaridis, “A numerical solution of the multidimensional solidification (or melting) problem,” *Int. J. Heat Mass Transf.*, vol. 13, no. 9, pp. 1459–1477, Sep. 1970, doi: 10.1016/0017-9310(70)90180-8.

[82] A. de Gracia and L. F. Cabeza, “Numerical simulation of a PCM packed bed system: A review,” *Renew. Sustain. Energy Rev.*, vol. 69, pp. 1055–1063, Mar. 2017, doi: 10.1016/j.rser.2016.09.092.

[83] K. Nagano, S. Takeda, T. Mochida, and K. Shimakura, “Thermal characteristics of a direct heat exchange system between granules with phase change material and air,” *Appl. Therm. Eng.*, vol. 14–15, no. 24, pp. 2131–2144, 2004, doi: 10.1016/j.applthermaleng.2004.02.004.

[84] K. A. R. Ismail and R. Stuginsky Jr, “A parametric study on possible fixed bed models for pcm and sensible heat storage,” *Appl. Therm. Eng.*, vol. 19, no. 7, pp. 757–788, Jul. 1999, doi: 10.1016/S1359-4311(98)00081-7.

[85] T. E. W. Schumann, “Heat transfer: A liquid flowing through a porous prism,” *J. Frankl. Inst.*, vol. 208, no. 3, pp. 405–416, Sep. 1929, doi: 10.1016/S0016-0032(29)91186-8.

[86] X. Cheng, X. Zhai, and R. Wang, “Thermal performance analysis of a packed bed cold storage unit using composite PCM capsules for high temperature solar cooling application,” *Appl. Therm. Eng.*, vol. C, no. 100, pp. 247–255, 2016, doi: 10.1016/j.applthermaleng.2016.02.036.

[87] D. Y. Y. Goswami, “Numerical and experimental studies on heat transfer characteristics of thermal energy storage system packed with molten salt PCM capsules”, Accessed: Jan. 17, 2023. [Online]. Available: https://www.academia.edu/24373464/Numerical_and_experimental_studies_on_heat_transfer_characteristics_of_thermal_energy_storage_system_packed_with_molten_salt_PCM_capsules

[88] V. R. Voller, “Fast Implicit Finite-Difference Method for the Analysis of Phase Change Problems,” *Numer. Heat Transf. Part B Fundam.*, vol. 17, no. 2, pp. 155–169, Jan. 1990, doi: 10.1080/10407799008961737.

[89] S. Lohrasbi, M. Sheikholeslami, and D. D. Ganji, “Multi-objective RSM optimization of fin assisted latent heat thermal energy storage system based on solidification process of phase change Material in presence of copper nanoparticles,” *Appl. Therm. Eng.*, vol. 118, pp. 430–447, May 2017, doi: 10.1016/j.applthermaleng.2017.03.005.

[90] Y. Dutil, D. R. Rousse, N. B. Salah, S. Lassue, and L. Zalewski, “A review on phase-change materials: Mathematical modeling and simulations,” *Renew. Sustain. Energy Rev.*, vol. 15, no. 1, pp. 112–130, 2011.

[91] V. Udoewa and V. Kumar, “Computational Fluid Dynamics,” *Appl. Comput. Fluid Dyn.*, 2012.

[92] T. J. Baker, “Fluent User’s Guide,” p. 4944, 2021.

[93] G. C. Naidu, K. D. Reddy, and P. V. Ramaiah, “CFD Simulation for Charging and Discharging Process of Thermal Energy Storage System using Phase Change Material,” *Int. J. Eng. Res.*, p. 8, 2016.

[94] A. B. Zavoico, “Solar Power Tower Design Basis Document, Revision 0; TOPICAL,” Sandia National Labs., SAND--2001-2100, 2001. Accessed: Aug. 12, 2021. [Online]. Available: http://inis.iaea.org/Search/search.aspx?orig_q=RN:33052855

[95] Y. T. Lee, S. W. Hong, and J. D. Chung, “Effects of capsule conduction and capsule outside convection on the thermal storage performance of encapsulated thermal storage tanks,” *Sol. Energy*, vol. 110, pp. 56–63, Dec. 2014, doi: 10.1016/j.solener.2014.08.034.